NASA/TP-2008-215317

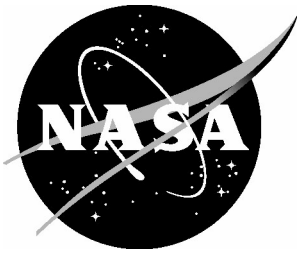

Correlations for Boundary-Layer Transition on Mars Science Laboratory Entry Vehicle Due to Heat-Shield Cavities

Brian R. Hollis and Derek S. Liechty
Langley Research Center, Hampton, Virginia

June 2008

The NASA STI Program Office . . . in Profile

Since its founding, NASA has been dedicated to the advancement of aeronautics and space science. The NASA Scientific and Technical Information (STI) Program Office plays a key part in helping NASA maintain this important role.

The NASA STI Program Office is operated by Langley Research Center, the lead center for NASA's scientific and technical information. The NASA STI Program Office provides access to the NASA STI Database, the largest collection of aeronautical and space science STI in the world. The Program Office is also NASA's institutional mechanism for disseminating the results of its research and development activities. These results are published by NASA in the NASA STI Report Series, which includes the following report types:

- TECHNICAL PUBLICATION. Reports of completed research or a major significant phase of research that present the results of NASA programs and include extensive data or theoretical analysis. Includes compilations of significant scientific and technical data and information deemed to be of continuing reference value. NASA counterpart of peer-reviewed formal professional papers, but having less stringent limitations on manuscript length and extent of graphic presentations.

- TECHNICAL MEMORANDUM. Scientific and technical findings that are preliminary or of specialized interest, e.g., quick release reports, working papers, and bibliographies that contain minimal annotation. Does not contain extensive analysis.

- CONTRACTOR REPORT. Scientific and technical findings by NASA-sponsored contractors and grantees.

- CONFERENCE PUBLICATION. Collected papers from scientific and technical conferences, symposia, seminars, or other meetings sponsored or co-sponsored by NASA.

- SPECIAL PUBLICATION. Scientific, technical, or historical information from NASA programs, projects, and missions, often concerned with subjects having substantial public interest.

- TECHNICAL TRANSLATION. English-language translations of foreign scientific and technical material pertinent to NASA's mission.

Specialized services that complement the STI Program Office's diverse offerings include creating custom thesauri, building customized databases, organizing and publishing research results ... even providing videos.

For more information about the NASA STI Program Office, see the following:

- Access the NASA STI Program Home Page at ***http://www.sti.nasa.gov***

- E-mail your question via the Internet to help@sti.nasa.gov

- Fax your question to the NASA STI Help Desk at (301) 621-0134

- Phone the NASA STI Help Desk at (301) 621-0390

- Write to:
  NASA STI Help Desk
  NASA Center for AeroSpace Information
  7115 Standard Drive
  Hanover, MD 21076-1320

NASA/TP-2008-215317

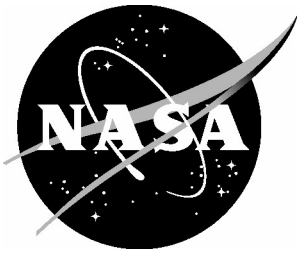

Correlations for Boundary-Layer Transition on Mars Science Laboratory Entry Vehicle Due to Heat-Shield Cavities

Brian R. Hollis and Derek S. Liechty
Langley Research Center, Hampton, Virginia

National Aeronautics and
Space Administration

Langley Research Center
Hampton, Virginia 23681-2199

June 2008

Available from:

NASA Center for AeroSpace Information (CASI)
7115 Standard Drive
Hanover, MD 21076-1320
(301) 621-0390

National Technical Information Service (NTIS)
5285 Port Royal Road
Springfield, VA 22161-2171
(703) 605-6000

Table of Contents

List of Tables

List of Figures

Abstract

The influence of cavities (for attachment bolts) on the heat-shield of the proposed Mars Science Laboratory entry vehicle has been investigated experimentally and computationally in order to develop a criterion for assessing whether the boundary layer becomes turbulent downstream of the cavity. Wind tunnel tests were conducted on the 70-deg sphere-cone vehicle geometry with various cavity sizes and locations in order to assess their influence on convective heating and boundary layer transition. Heat-transfer coefficients and boundary-layer states (laminar, transitional, or turbulent) were determined using global phosphor thermography. The wind tunnel tests were performed with 5.00-inch (0.127 m) diameter models at Mach 6 over a free-stream unit Reynolds number range of $1.2x10^6$/ft to $7.3x10^6$/ft ($3.8x10^6$/m to $24x10^6$/m) with angles-of-attack of 0-deg, 11-deg, 16-deg, and 20-deg. Laminar and turbulent Navier-Stokes computations were performed at the test conditions in order to compare with the experimental aeroheating data and to determine boundary layer parameters for use in correlating the experimental transition data. Comparisons of laminar heating data and computations agreed to within an estimated experimental uncertainty of ±13%, but turbulent computations were up to 20% than the experimental data. It was hypothesized that the greater differences for turbulent cases were due to the fact that the cavities were not included in the simple computational geometry employed. The cavity transition data were analyzed to determine correlations for transition to turbulence at a cavity in terms of its geometric parameters and computed boundary-layer conditions. This correlation was used to show that the vehicle could experience onset of turbulent flow due to the presence of cavities well before the peak heating point on the trajectory. In part because of the results of this study, the attachment points were moved to the aftbody of the vehicle where their influence on the heating environment would be minimal.

Nomenclature

Symbols

a_w	speed of sound at wall (m/s)
H_{aw}	adiabatic enthalpy (J/kg)
H_w	wall enthalpy (J/kg)
H_0	total enthalpy (J/kg)
h	heat transfer coefficient (kg/m^2/sec),
h_{FR}	Fay-Riddell heat transfer coefficient (kg/m^2/sec)
k	cavity depth (in)
M_0	correlation curve fit coefficient
M_1	correlation curve fit coefficient
M_∞	free-steam Mach number
M_e	boundary layer edge Mach number
q	heat transfer rate (W/m^2)

r radial position (m)
$R_{Pearson}$ Pearson's correlation coefficient
R base (maximum) radius (m)
R_n nose radius (m)
R_c corner radius (m)
Re_∞ free-stream unit Reynolds number (1/m or 1/ft)
Re_{cell} wall cell Reynolds number $= \left(\rho_w a_w \Delta s\right)/\mu_w$
Re_θ momentum thickness Reynolds number $= \left(\rho_e a_e \theta\right)/\mu_e$
$Re_{w,e}$ critical Reynolds number $= \left(\rho_e a_e w\right)/\mu_e$
T_e boundary layer edge temperature (K)
T_w wall temperature (K)
T_∞ free-stream temperature (K)
U_∞ free-stream velocity (m/sec)
x distance along centerline (m)
w cavity diameter (in)
α angle-of-attack (deg)
δ boundary layer thickness (m)
ϕ model rotation (deg)
Δs wall cell height (m)
θ boundary-layer momentum thickness (m)
μ_w wall cell viscosity (kg/m/s)
ρ_∞ free-stream density (kg/m^3)
ρ_w wall cell density (kg/m^3)

Subscripts

aw adiabatic wall
fs full scale
FR Fay-Riddell
ms model scale
w wall
∞ free stream

Abbreviations

LAURA Langley Aerothermodynamic Upwind Relaxation Algorithm
La laminar
Lo localized disturbance
MSL Mars Science Laboratory
Tr transitional
Tu turbulent
UV ultraviolet

Introduction

The entry vehicle for the Mars Science Laboratory (MSL) mission (Refs. 1, 2), which was originally known as the Mars Smart Lander, will perform a precision landing of a scientific payload on Mars and is currently scheduled for launch in 2009. One of the important design issues for such an entry vehicle is determining whether the boundary layer on the forebody heat shield will be laminar or turbulent. This problem was more complicated for

MSL than any previous Mars missions because preliminary designs included six circular cavities equally spaced around the circumference of the forebody heat shield where bolts would be used to attach the vehicle to a cruise stage during transit from Earth.

The goal of this study was to formulate a criterion for boundary-layer transition due to the cavities on the MSL forebody that would account for cavity size and location, angle-of-attack, and Reynolds number. To accomplish this goal, wind tunnel tests (designated as 20-Inch Mach 6 Air Tests 6823 and 6827) were conducted to generate a transition database for these parametrics. Navier-Stokes computations were performed at the wind tunnel conditions to determine boundary-layer edge properties that were then used to correlate the experimental transition data. The transition data and the correlations are presented in this paper and comparisons of both laminar and turbulent aeroheating predictions with sample experimental data are also presented. Preliminary results of this work have also been presented in Refs. 3, 4, and 5. A more detailed investigation of the MSL aeroheating environment during Mars entry was presented in Ref. 7.

Mars Science Laboratory Entry Vehicle Geometry

When this study was conducted, the proposed Mars Science Laboratory entry vehicle geometry was a 70-deg sphere-cone with a biconic aftbody (Figure 1). Preliminary forebody designs included six cavities spaced at 60-deg increments where the entry vehicle would be bolted to the carrier vehicle in transit to Mars (Figure 2). The size and locations of these cavities had not yet been fixed, and so the effects of cavity diameter, radial location, and angular location on the aeroheating environment and boundary-layer transition were investigated. The final MSL geometry is still a 70-deg sphere-cone; however, the aftbody shape has changed considerably and the attachment points have been moved to the aftbody, in part because of the results of this study.

When the Mars Science Laboratory mission planning began, a small control surface that projected from the forebody was under consideration in order to increase aerodynamic trimming capability. Various sizes, shapes, and inclinations for the control surface (Figure 3) were investigated during the experimental phase of this study (Ref. 5). Although no control surface was included in the final MSL design, cavity transition data from the control surface model tests are part of the database (the control surface is downstream of the cavities and does not influence transition) and are also reported in Ref. 5 for future reference.

Computational Methods

Numerical Algorithm

Computations were performed using the LAURA code (Refs. 7, 8). LAURA (Langley Aerothermodynamic Upwind Relaxation Algorithm) is a three-dimensional, finite-volume solver which includes perfect-gas, equilibrium and non-equilibrium chemistry models. The code can be used to solve the inviscid, thin-layer Navier-Stokes, or full Navier-Stokes equations. In the current study the thin-layer model was employed. Time integration to steady-state in LAURA is accomplished through point-relaxation or line-relaxation schemes. Roe-averaging (Ref. 9) with Harten's entropy fix (Ref. 10) and Yee's Symmetric Total Variation Diminishing limiter (Ref. 11) is used for inviscid fluxes, and a second-order scheme is employed for viscous fluxes. For turbulent computations, the algebraic Baldwin-Lomax (Ref. 12) model with modifications (Ref. 13) for compressible flow and the Dhawan-Narashima (Ref. 15) transition model were employed. In this study, the perfect-gas air model was used for all wind tunnel computations.

Free-Stream and Surface Boundary Conditions

Computations were performed at wind tunnel conditions for angles-of-attack of 0-deg, 11-deg, 16-deg, and 20-

deg at each of the Reynolds number operating points of the NASA LaRC 20-Inch Mach 6 Air Tunnel. These conditions are listed in Table 1. Note that the Reynolds numbers are listed in English units in addition to metric as English units are commonly used to refer to the operating points of the tunnel. For these wind tunnel cases, a uniform, ambient 300 K wall temperature boundary condition was imposed. The use of a constant wall temperature is valid because the experimental data and computations are reported in terms of a non-dimensional heat-transfer ratio h/h_{FR}, which takes into account surface temperature variations, and because the surface temperature rise during a wind tunnel run is not large enough to affect the flow field.

Computational Grid

A multiple-block grid with a singularity-free nose was employed for the computations. Several variations of the leeside grid block where the control surface is located were generated and could be substituted to compute the flow around the various control surface geometries. Although the full grid completely encompassed the aftbody and wake, computations were limited to the forebody blocks as this was the region of interest in the present study and because the aftbody flow has no influence on the forebody. The forebody grid blocks contained approximately 230,000 points with a body-normal direction resolution of 65 points. Grid adaptation was performed (as per the method detailed in Ref. 9) to align the grid with the bow shock and to produce nominal wall cell Reynolds numbers on the order of 10 or less.

The effects of normal grid-point resolution on the computed heating distributions was examined by repeating the computations for the α = 16-deg, $Re_\infty = 7.3 \times 10^6$/ft case with grids containing half (32) and twice (128) as many cells as in the nominal grid (64). The heating distributions from these computations are shown in Figure 4. Computed heating levels were found to drop nearly uniformly over the entire surface by about 5% from the 32-cell grid to the 64-cell grid, but from the 64-cell grid to the 128-cell grid heating levels dropped by about 1% except around the stagnation regions where the decrease was approximately 2%. Therefore, it was concluded that the original 64-cell grid provided acceptable resolution for this study.

Although the wind tunnel test models were fabricated with actual cavities to replicate those in the flight vehicle heat shield, the MSL computational grid did not include these cavities. Thus, the effects of the cavities on the flow field were not directly modeled by the computations. In the turbulent computations, the effects of the cavities on the state of the boundary layer were approximately simulated by specifying that transition began at the cavity location. In order to attempt to bound the effects of the cavity on boundary-layer transition, either an instantaneous transition to fully-developed turbulent flow downstream of the cavity was specified (as might be caused by a large cavity), or the Dhawan-Narashima transition model was employed with the transition length set equal to the running length of the boundary layer from the nose of the vehicle to the cavity location (as might be caused by a small cavity or by natural, smooth-body transition).

Experimental Methods

A description of the methods employed in the experimental study which complimented this computational study is presented in this section. A more detailed presentation and analysis of the experimental heating-rate data obtained in this study can be found in Refs. 3, and 5.

Test Facility Description

Aeroheating tests were conducted in the NASA Langley 20-Inch Mach 6 Air Tunnel (Figure 5). This facility is a blow-down tunnel in which heated, dried, and filtered air is used as the test gas. The tunnel has a two-dimensional, contoured nozzle that opens into a 20.5 by 20.0 inch test section. The tunnel is equipped with a bottom-mounted injection system which can transfer a model from the sheltered model box to the tunnel centerline in less than 0.5

sec. Run times of up to 15 minutes are possible in this facility, although for this aeroheating study run times of only a few seconds were required to obtain data. The nominal reservoir conditions of this facility are stagnation pressures of 206.8 to 3447.4 kPa (30 to 500 psia) with stagnation temperatures of 422.2 to 555.5 K (760˚ to 1000 ˚R) that produce perfect-gas free stream flows with Mach numbers between 5.8 and 6.1 and Reynolds numbers from 1.64×10^6 to 23.3×10^6 1/m (0.5×10^6 to 7.1×10^6 1/ft). A more detailed description of this facility is presented in Refs. 15-16. Representative flow conditions for each of the nominal 20-Inch Mach 6 Air Tunnel operating points have been computed using the GASPROPS code (Ref. 17) and are listed in Table 1.

Thermographic Phosphor Global Heating Technique

Global surface heating distributions were obtained through the digital optical measurement method of two color, relative-intensity, phosphor thermography (Refs. 18-21). In this method, ceramic wind tunnel models are coated with a phosphor compound that fluoresces in two separate regions (green and red) of the visible light spectrum. During a wind tunnel run, the phosphor-coated model is illuminated by ultraviolet (UV) light sources, and the resulting fluorescent intensity of the model is recorded and digitized through a three-color charge coupled device camera (Figure 6). The fluorescent intensity is dependent on both the intensity of incident UV light and the local model surface temperature. The UV intensity dependence is removed by taking the ratio of the green to red intensity images, from which surface temperature distributions can be determined through prior calibrations. Images of the model are acquired in the tunnel before and during a run and global heat transfer distributions are then computed from the changes in temperatures between these images using one-dimensional, constant heat-transfer coefficient conduction theory.

Thermographic phosphor data are commonly reported in terms of the heat-transfer coefficient ratio, h/h_{FR}, where h is the heat transfer coefficient measured in the wind tunnel and h_{FR} is a reference heat transfer coefficient based on Fay-Riddell theory (Ref. 22). The heat-transfer coefficient is defined as:

$$h = q/\left(H_{aw} - H_w\right) \tag{1}$$

To calculate the heat-transfer coefficient, the adiabatic wall enthalpy H_{aw} is set equal to the total enthalpy H_0 in the tunnel. This heat-transfer coefficient definition provides a theoretically constant value over the course of a wind tunnel run since the decrease over time in the heating rate, q, as the wind tunnel model becomes hotter is offset by the decrease of the enthalpy difference term in the denominator. The Fay-Riddell value, h_{FR}, in the ratio is computed using the nose radius of the vehicle at the appropriate model scale with the wall temperature at an ambient value of 300 K. Heat transfer results from the computations will also be presented in terms of the ratio h/h_{FR} for consistency.

As discussed in Ref. 21 , the experimental uncertainty of the phosphor technique is dependent on the temperature rise on the surface of the test model. For the experimental results discussed herein, forebody surface heating data were estimated to have an uncertainty of ±8% due to the measurement technique. The overall uncertainty was estimated to be ±13% by taking into account all factors, such as free stream conditions and flow uniformity, model placement, accuracy of model aerolines, etc.

Wind Tunnel Model Descriptions

Cast ceramic models are used for aeroheating testing with the thermographic phosphor system. To fabricate these models, a rapid prototyping stereolithographic apparatus is first used to build a resin pattern of the configuration. Next, a wax mold of the resin pattern is formed, and then a patented (Ref. 23) fused silica-ceramic investment slip-casting technique is used to make a ceramic shell model of the vehicle. The ceramic shell model is

backfilled with a hydraulically setting magnesia ceramic for strength and support into which a sting is fixed. Finally, the model is coated with a mixture of phosphors suspended in a silica-based colloidal binder.

The model scale for the aeroheating tests was 0.031358, which resulted in 5.00-inch (0.127 m) diameter models (Figure 7). Models of the baseline configuration and configurations with a control surface "tab" were fabricated both with (Figure 8) and without cavities. For the baseline models, cavities of 1.5-in. (3.8 cm), 2.2-in. (5.6 cm), and 3.0-in. (7.6 cm) diameter (full-scale) were spaced (Figure 9) at 60-deg increments around the forebody at radial locations of r/R = 0.41 and 0.70. Two identical baseline models, designated as B-5-PA-2 and B-5-PA-3 were fabricated and tested (because the phosphor coating tends to become worn after extensive testing). Three different cavity layouts were employed for the "tab" control surface models (Figure 10), with six cavities of either 1.5-in. (3.8 cm) or 3.0-in. (7.6 cm) diameter spaced at 60-deg increments around the forebody at a radial location of r/R = 0.41. These models were designated as T-5-1C-1, T-5-3B-1 and T-5-3C-1. Cavity diameters listed above are all nominal values. The measured "as-built" cavity radii, depth, and locations for each of the test models are given in Table 2 - Table 6. These actual values, not the nominal values, were used in the formulation of transition criteria. Cavity depths were not rigorously controlled; in general the ratio of cavity diameter to depth was in the range of 2 to 4.

In addition to the MSL models fabricated for this study, a model of the Genesis solar-wind sample return mission vehicle was also fabricated and tested. This configuration was examined in order to extend the sample range of the cavity correlation and to take advantage of the cavity data obtained in the Genesis aerothermodynamic study (Ref. 24). The cavity dimension data from the original Genesis model and the newly-built model (designated as G-5-PA-1) used in the current study are given in Table 7 - Table 8. The scale for the original Genesis model was 0.100 and the scale for the new model was 0.0833.

Comparisons of Aeroheating Computations with Wind Tunnel Data

Comparisons between wind tunnel heating data and predictions (both laminar and turbulent) are discussed in this section. The laminar computations are presented in order to demonstrate that the numerical method employed satisfactorily reproduced the observed smooth model data. This demonstration was necessary because, as will be discussed in a subsequent section, the results from the laminar flow field computations were employed to formulate boundary layer transition correlations. The turbulent comparisons are presented in order to provide some insight into the applicability of the relatively simple turbulence modeling methods employed herein to the problem of transition due to heat shield cavities. However, this study is not meant to be a comprehensive analysis of numerical simulation of transition and turbulence.

Laminar Aeroheating Comparisons

Laminar computations were performed at the conditions listed in Table 1 for angles-of-attack of 0-deg, 11-deg, 16-deg, and 20-deg. Symmetry plane comparisons of these computed heating distributions with the wind tunnel data for each angle-of-attack are presented in Figure 11 - Figure 14. In these figures, the experimental data were obtained on models without cavities. For all cases, the computed laminar heating distributions were found to agree with the experimental data to within the estimated ±13% uncertainty.

Turbulent Aeroheating Comparisons

Turbulent computations were performed for wind tunnel conditions of $Re_\infty = 4.2\text{x}10^6$/ft to $7.3\text{x}10^6$/ft ($1.4\text{x}10^7$/m to $2.4\text{x}10^7$/m). Computations were performed at α = 16-deg, which was the nominal angle-of-attack at peak heating on the flight trajectory at the time that this study was in progress (values have varied from 11-deg to 20-deg over the course of the program). Symmetry-plane comparisons of these computations with the experimental data for both radial cavity locations are shown for $r/R = 0.41$, $Re_\infty = 4.2\text{x}10^6$/ft, $5.8\text{x}10^6$/ft, and $7.3\text{x}10^6$/ft in Figure 15 - Figure 17

and for the same Reynolds numbers with $r/R = 0.70$ in Figure 18 - Figure 20. In both sets of figures, comparisons are shown only for the leeside of the heat shield because the flow on the windside remained laminar and the wind-side centerline cavity was observed to have little or no effect on the heating except at the cavity itself.

Because boundary-layer transition in these tests was produced artificially by cavities in the test models (as opposed to natural transition on a smooth model surface) transition in the computations was modeled in several different ways in order to attempt to simulate the observed behavior. The computations were performed with the following options:

1. The boundary layer fully turbulent over the entire length of the vehicle.

2. Natural, smooth-body transition beginning at the location of the cavity via the Dhawan-Narashima model (with transition length set equal to the running length of the flow from the nose to the cavity).

3. Zero-length transition to fully-turbulent flow at the cavity location.

As shown in Figure 15 - Figure 20, both the location at which transition was specified to begin and the length of transition that was specified had significant effects (~5% to 10% variation) on the computed turbulent heating levels downstream of transition.

The heating levels computed by specifying turbulent flow beginning at the cavity were higher than those computed when the flow was treated as turbulent from the nose of the vehicle. When turbulence was specified to begin at a cavity location, higher heating downstream of the cavity was predicted for zero-length transition than for natural transition. Also, when natural transition was specified at the outer, $r/R = 0.70$ cavity location, it did not appear than the boundary-layer had sufficient running-length for fully-turbulent flow to develop before the shoulder was reached; this observation is also supported by the experimental data.

The comparisons between experimental and computational results were also dependent on transition location and transition length, as well as on Reynolds number and cavity size. Comparisons for the cavity location of $r/R = 0.41$ are discussed first.

- At a Reynolds number of $Re_\infty = 4.2 \times 10^6$/ft for the cavity location of $r/R = 0.41$ (Figure 15), the smallest cavity had no noticeable effect on the heating and the predictions compared well with the data. The intermediate cavity caused a small (~10%) rise in heating, while the largest cavity produced a significant increase (> 30%) in heating. For the two large cavity cases, the measured heating levels continued to rise gradually over the length of the vehicle and never reached a "plateau" indicative of fully-developed turbulent flow. For the two larger cavity cases, the measured heating levels fell between the laminar and natural transition computations except immediately behind the cavity.

- At a Reynolds number of $Re_\infty = 5.8 \times 10^6$/ft for the cavity location of $r/R = 0.41$ (Figure 16), the data for the smallest cavity appeared to remain laminar and matched the laminar computation. The shapes of the heating distributions for the two larger cavities were similar in character to the natural transition prediction. However, the measured heating rates downstream of the cavities reached maximum values 15% to 20% higher than all the turbulent predictions.

- At a Reynolds number of $Re_\infty = 7.3 \times 10^6$/ft for the cavity location of $r/R = 0.41$ (Figure 17), the beginning of transition was noted downstream of the smallest cavity, but the boundary layer did not

appear to develop into fully-turbulent flow. The shapes of the heating distributions for the two larger cavity were similar to the zero-length transition predictions, but the peak heating levels were again 15% to 20% higher than the computed turbulent values.

Comparisons for the cases with the cavity located at $r/R = 0.70$ are discussed next. These cases were not as well suited for comparison as the $r/R = 0.41$ case. For the these $r/R = 0.70$ cases, the boundary layer did not appear to have sufficient running length between the cavity and the shoulder of the model for fully turbulent flow to develop, except possibly for the largest cavity size at the highest Reynolds number.

- At a Reynolds number of $Re_\infty = 4.2 \times 10^6$/ft for the cavity location of $r/R = 0.70$ (Figure 18), no deviation from laminar behavior was observed for the two smaller cavity sizes. The large cavity heating distribution had a shape similar to the natural-transition computation but with a greater magnitude.

- At a Reynolds number of $Re_\infty = 5.8 \times 10^6$/ft for the cavity location of $r/R = 0.70$ (Figure 19), a small heating augmentation similar to that of the natural transition computation was observed for the two smaller cavities. The large cavity data heating distribution was similar in shape to the zero-length transition computation and the predicted heating rates agreed with the data to within the experimental uncertainty. However, given the small length of apparently turbulent flow observed for this case, this good agreement may have been coincidental, especially in light of the under-prediction of the turbulent heating levels observed for the $r/R = 0.41$ cases

- At a Reynolds number of $Re_\infty = 7.3 \times 10^6$/ft for the cavity location of $r/R = 0.70$ (Figure 20), significant heating increases were observed for all three cavity sizes. The measured heating levels for the two smaller cavities fell between the natural-transition and the zero-length transition computations. The large cavity heating data matched the fully-turbulent computation, but as noted for the previous case, this agreement may only have been coincidental.

In summary, the present method for predicting turbulent heating levels (an algebraic turbulence model with a specified transition location and various transition lengths) roughly bounded the $r/R = 0.70$ experimental heating data (which appeared to be produced by transitional boundary-layer flow) for the range of Reynolds numbers and cavity sizes. However, for the $r/R = 0.41$ cavity location, the computations under-predicted the measured peak heating levels by up to 20%, although the shapes of the heating distributions were approximately reproduced. In general, it would appear that this method is not sufficient to accurately reproduce the non-laminar, cavity-influenced experimental data. However, it should be noted that the actual heat-shield cavities were not included in the computational geometry, and their effects on the inviscid flow field (e.g. flow field separation and/or shocks at the cavity edge) may have been the cause for these differences.

In a similar study (Ref. 24) for the Genesis mission, the cavity was modeled in the computations. In that study it was found that the presence of the cavity had significant effects both on heating around the cavity itself, where a localized maxima in the heating levels was predicted, and downstream of the cavity, where heating levels lower than those without the cavity were predicted. However, it was also concluded in that study that the simple algebraic transition/turbulence models used (the same as in this study) were not sufficient to resolve the effects of the cavity even with the cavity included in the computational geometry.

In terms of design criteria for an actual vehicle, the worst-case for heating, based on these experimental data, would be a cavity at the inner $r/R = 0.41$ location of sufficient diameter to cause transition. The longer running length from this location would produce higher turbulent heating levels than that for a cavity at $r/R = 0.70$. Examples of this case are the data for the two larger cavities at $Re_\infty = 7.3 \times 10^6$/ft (Figure 17). For these cases, the turbulent experimental heating levels downstream of the cavity were approximately 25% higher than the laminar

levels measured at the nose. In comparison to the predicted heating levels, the experimental heating levels were approximately 10% higher than the predicted fully-turbulent levels at the nose and were approximately 20% higher than those predicted downstream of the cavity using the zero-length transition model. With regard to vehicle heat shield design, it should also be noted that heating augmentation factors derived from the current data may not be appropriate for flight through the atmosphere of Mars because these data were obtained in a low-enthalpy, perfect-gas air environment at a low hypersonic Mach number. Also, the spatial resolution of the plots herein is not sufficient to show the localized heating augmentation produced immediately downstream of the cavity, which can reach levels greater than the measured downstream turbulent data.

Boundary Layer Transition Correlations

The primary goal of this study was to generate correlations between heat-shield cavity parameters and boundary-layer transition in order to guide the design and placement of these cavities for the MSL entry vehicle. Many studies have been conducted on the similar problem of boundary-layer transition correlations for roughness elements (i.e. steps or protrusions) and a historical review of such roughness correlations can be found in Ref. 25. More recently, correlations have been developed for the Space Shuttle Orbiter (e.g. Refs. 26-28), the X-33 (Ref. 29), and the X-38 (Ref. 30). However, the subject of correlations for the effects of small cavities on boundary-layer transition (as opposed to transition correlations or heating/pressure data for backward-facing steps or large cavities) has received little study; the only notable references found were those by Todisco (Ref. 31) for a hemisphere and by Cheatwood (Ref. 24) for the Genesis sample return capsule.

Classification of Transition Data

More than 800 data points on the state of the boundary layer were obtained during the wind tunnel testing. This data set covered the full test range of angles-of-attack, free-stream Reynolds numbers, cavity diameters, and cavity radial locations. Approximately 90% of the data were obtained on MSL models and the rest were obtained on Genesis models (including a few data points taken from Ref. 24). For each data point, the state of the boundary layer downstream of the cavity was determined through visual inspection of the surface heating images and classified as either: laminar; localized disturbance and heating effects at the cavity; transitional at or downstream of the cavity; or fully turbulent at the cavity. Examples of experimental data that fit each of these classifications are shown in Figure 21. These classifications are somewhat simplified descriptions of a complex flow field and should be used with care. For example, for a case classified as “localized disturbance”, the heating levels measured near the cavity may be higher than heating levels farther downstream of the cavity for a case classified as “transition downstream”. Additionally, because of the three-dimensional nature of the flow over this geometry at angle-of-attack, transitional/turbulent heating levels downstream of a cavity are highly dependent on the location of that cavity.

The global heating images from each wind tunnel run used to determine the state of the boundary layer are presented in Figure 22 to Figure 59. Data from the baseline (no control surface) configuration models B-5-PA-2 and B-5-PA-3 are shown for α = 0-deg to 20-deg in Figure 22 to Figure 48. Data from the tab control surface models T-5-1C-1, T-5-3B-1, and T-5-3C-1 are shown for α = 11-deg to 20-deg in Figure 49 to Figure 56. Data from the old and new Genesis models are shown in Figure 57 to Figure 59.

In these figures, the images obtained at each Reynolds number at which a model was tested at a given angle-of-attack and rotation are arranged by increasing Reynolds number from top-to-bottom in two columns. Each figure also includes a diagram that shows the orientation (ϕ) and the placement (r/R) of the cavities for the given case. The state of the boundary layer downstream of each cavity is denoted on the individual images following the classification system previously discussed as “La” (laminar), “Lo” (localized disturbance following the cavity), “Tr” (transitional downstream of the cavity), or “Tu” (turbulent at the cavity). In regards to these images, several

qualifiers must be given. First, the images are reproduced to lower resolution than available in the original digital data, and so smaller disturbances may not be recognizable. Second, each model has a large number of fiducial marks (dots of ink) which are used to relate pixel locations to geometric position and these should not be confused with the actual cavities. And finally, damage to the phosphor coating on the model from natural wear over numerous runs and from particulate impacts often caused boundary layer transition at locations other than the cavities. Also, with respect to the interpretation of the data itself, it should be noted the state of the boundary layer at each cavity was not always completely clear from the image data. However this database should be large enough that the occasional data point that was difficult to classify with complete confidence does not skew the derived correlations.

Parameters for Boundary-Layer Transition Correlations

Boundary-layer transition correlations are typically formulated in terms of the physical parameters of the tripping mechanism (a step, gap, protuberance, etc) and the fluid dynamic parameters of the boundary layer. In this study, the tripping parameters of interest were the diameter (w) and depth (k) (listed in Table 2 through Table 8). The boundary-layer parameters of interest were the edge Mach number (M_e), boundary layer thickness (δ), and edge Reynolds number based on momentum thickness and local flow field quantities (Re_θ).

The parameter θ (momentum thickness) is also commonly employed in transition correlations; however, in the present perfect-gas data set, the ratio θ/δ (sometime referred to as the "shape factor") was very nearly constant at a value of 7.35 as shown in Figure 60 (the small differences noted were probably due mainly to numerical error in determining the edge of the boundary layer on a grid with a finite number of points). Therefore, inclusion of this variable would be redundant in the current analysis, but may well be important when correlating data across a wider range of conditions where the shape factor is not a constant.

Another variable, the ratio of boundary-layer edge temperature to wall temperature, T_e/T_w, has also been employed in past transition correlations. In the phosphor thermography technique employed in this study, data are taken before the wall temperature has time to experience a significant increase. For the purposes of this correlation study, the wall temperature can be approximated as constant at ambient (T_w = 300 K) conditions. For the range of test conditions, temperature ratios generally varied between 1.5 to 1.7, and an average value of T_e/T_w = 1.6 was assumed. Therefore, since the ratio T_e/T_w was effectively a constant, it was not included in the analysis, although as with the shape factor, it would probably have had some influence if data from a wider range of conditions were under consideration.

Information on these boundary-layer variables was extracted from the computed laminar flow field solutions. These laminar computations were performed for the complete wind tunnel test range of angle-of-attack (α = 0-deg, 11-deg, 16-deg, and 20-deg) and Reynolds numbers (Re_∞ = 2.1x10^6/ft to 7.3x10^6/ft). To determine these properties, the boundary layer edge was defined as the distance normal to the surface at which the total enthalpy was equal to 99.5% of the free stream total enthalpy, with linear interpolation performed between solution grid points in order to more precisely determine this location. Sample distributions of Re_θ and δ are shown in Figure 61 - Figure 63 for α = 11-deg, 16-deg and 20-deg cases.

Transition Correlations

The boundary-layer states determined from the images in Figure 22 through Figure 59 are classified and plotted in Figure 64 through Figure 71; results are plotted on both linear and logarithmic scale to aid in the interpretation of the data. In each figure, the data are plotted with a different set of variables: Re_θ vs. w/δ in Figure 64 and Figure 65; Re_θ vs. k/δ in Figure 66 and Figure 67; Re_θ/M_e vs. w/δ in Figure 68 and Figure 69; and Re_θ/M_e vs. k/δ in Figure 70 and Figure 71.

Although a statistical analysis will be presented subsequently as the basis and justification for the formulation of correlations from these data, it is apparent from inspection of these figures that in the plots where the cavity-diameter to boundary-layer height ratio (w/δ) was used as the abscissa (Figure 64, Figure 65, Figure 68, and Figure 69) the data sets that represent each of the different classifications (laminar, local, transitional, and turbulent) group much more closely and with less overlap between them than in those plots (Figure 66, Figure 67, Figure 70, and Figure 71) in which the cavity-depth to boundary-layer height ratio (k/δ) was used as the abscissa. In other words, the data appear to correlate better with cavity diameter than with cavity depth. This behavior may seem counterintuitive at first, and is not consistent with typical results from boundary-layer trip correlations based on surface roughness element heights. However, an analogy between the height of a roughness element and the depth of a cavity is not necessarily appropriate for all cavity flows.

Cavity flows can be classified as either open or closed (e.g. Refs. 32 through 34) depending on the aspect ratio (w/k) of the cavity. A two-dimensional illustration of these types of cavity flows is given in Figure 72. In a closed cavity flow, the cavity aspect ratio is large enough that the upstream and downstream walls of the cavity are effectively isolated from each other's influence and so the boundary layer remains attached to the surface except perhaps in small regions in the immediate vicinity of the cavity's edges. In this closed cavity type of flow, an analogy between the flow approaching the downstream cavity wall and the flow over a protruding roughness element is apparent, and a correlation in terms of cavity depth would likely be appropriate. However, in an open cavity flow, the cavity aspect ratio is small and the relative proximity of the upstream and downstream walls forces the boundary layer to separate and form a free shear layer that skips over the cavity and reattaches on the other side. In this case, there is relatively little curvature of the free shear layer due to the cavity, and thus an analogy between cavity depth and surface roughness height is not valid.

The aspect ratio of cavity width to cavity depth (w/k) has been identified as one of the parameters that determines whether a cavity flow is open or closed. Various authors have reported different values for this parameter depending on the external flow parameters (Mach number, pressure, etc) and the cavity shape (length, width, orientation, etc) of the problem under consideration. In general, data from past studies indicate that the change from open to closed cavity flow occurs somewhere between $(w/k) = 10$ to $(w/k) = 20$. In this study, values of the cavity aspect ratios (where the cavity diameter was identified as the length quantity) were all less than 10 (Table 2 through Table 8) with the exception of a single cavity on the G-5-PA-1 Genesis model. These low values suggest that open cavity flows were produced in the wind tunnel tests. Further evidence to support this hypothesis is the fact that, as noted previously, the data did not appear to correlate well with cavity depth, which would have been the expected behavior for closed cavity flows.

Accepting then the hypothesis that the cavity flow was of the open type instead of the closed type and thus cavity depth is not a relevant parameter, the data appear to indicate that the ratio of cavity diameter to boundary-layer height (w/δ) is the relevant parameter to use in an open-cavity transition correlation. It should be noted though that because of the circular cross-section of the cavities in the current study, the applicability of the cavity diameter may be a simplification of a more generalized set of correlation variables for open cavity flows such as cavity width, length, and orientation.

The choice of cavity depth, rather than cavity height, as a correlating parameter was validated statistically by curve-fitting equations to the data and evaluating the accuracy of those fits. Additionally, the selection of Re_θ rather than Re_θ/M_e as the ordinate variable was also made based on statistical analysis. For this analysis, equations were developed that could be used to represent boundaries below which the data were laminar and above which the data were turbulent. These boundary points were selected from Reynolds numbers "sweeps" of data points for which the cavity geometric parameters, model angle of attack, and model orientation remained constant. Several such sweeps are shown in Figure 73. By following such a sweep of data, the highest Reynolds number data point at which the boundary layer remained laminar and the lowest Reynolds number data point at which the boundary layer became

fully turbulent could be identified. For each set of boundary-layer and cavity parameters, these points for the laminar and turbulent equations were fitted to power-law curves of the form:

$$Y = M_0 \times X^{M_1} \tag{2}$$

The resulting correlation equations are plotted in Figure 74 to Figure 77 and the curve fit coefficients M_0 and M_1, along with the linear correlation parameter R_{Pearson}, are also shown. This correlation parameter (known as Pearson's R) is a measure of the accuracy of the curve fit. It has hypothetical maximum value of 1, which would indicate that the curve fit exactly matches all the data.

The best correlations for both the laminar and turbulent data were found when the data were expressed in terms of Re_θ vs. w/δ (R_{Pearson} values of 0.38 and 0.73, respectively), followed by Re_θ/M_e vs. w/δ (R_{Pearson} values of 0.17 and 0.57), then Re_θ vs. k/δ (R_{Pearson} values of 0.18 and 0.34). The worst correlations were those expressed in terms of Re_θ/M_e vs. k/δ (R_{Pearson} values of 0.02 and 0.28). These results confirmed the earlier assertion based on visual inspection of the data that the cavity depth is not a relevant parameter for an open-cavity correlation. These results also showed that Re_θ, rather than Re_θ/M_e, was the better correlation parameter for these data. The lack of observed dependence on boundary-layer edge Mach number was probably due to the fact that the flow field disturbance was caused by a feature at the wall (i.e. the cavity) as opposed to a feature near the edge of the boundary layer such as a protruding trip.

The best cavity effects correlations obtained from these data are given for the upper laminar limit on Re_θ by:

$$\left(\text{Re}_\theta\right)_{lam} = 2382.7 \times \left(w/\delta\right)^{-2.348} \tag{3}$$

and for the lower turbulent limit on Re_θ by:

$$\left(\text{Re}_\theta\right)_{turb} = 652.7 \times \left(w/\delta\right)^{-0.9214} \tag{4}$$

These curve fits should be considered applicable for a range of approximately $w/\delta = 2$ to 20 and $Re_\theta = 10$ to 300. It should be noted that these coefficients differ slightly from those reported earlier in Ref. 4 due to the inclusion of additional data from the MSL "tab" control surface models and the Genesis models, as well as careful re-evaluation of all the MSL model data points. While both correlations are of interest with respect to the physics involved in producing transition and turbulence, it is recommended that for practical heat-shield design purposes the laminar limit curve fit be employed because significant local heating augmentation may still occur even for conditions that fall between the laminar and turbulent limits.

The correlation data points and the Re_θ vs. (w/δ) correlations are shown again with uncertainty margins of ±20% in Figure 78 and these correlations are shown along with the entire data set in Figure 79 - Figure 80. The margins are added because the correlations are not perfect; for design purposes points that fall within those margins should be considered carefully. Most of the turbulent boundary-point data points fall within these margins, whereas the deviation of the laminar boundary-point data and the laminar correlation at higher (w/δ) is likely due to the sparseness of data in that region. Also, the overlap of these curve fits for low values of (w/δ) with high values of Re_θ is due to that fact that at high enough values of Re_θ natural "smooth-body" transition occurred regardless of the cavity size. This natural transition limit is typically taken to be in the range of $Re_\theta = 200$ to 400 (e.g. Ref. 35).

In addition to the above correlations, a critical Reynolds number can also be defined. This parameter was

introduced by Schiller (Ref. 36) and has been employed in several studies (Refs. 26, 37-38) to correlate transition data. It is defined as:

$$\left(\mathrm{Re}_{w,e}\right)_{crit} = \frac{\rho_e U_e w}{\mu_e} = \mathrm{Re}_\theta \left(\frac{w}{\theta}\right) \tag{5}$$

To determine the critical Reynolds number for the current data set, a new power-law curve fit for the turbulent boundary limit was generated by fixing the exponent at -1:

$$\left(\mathrm{Re}_\theta\right)_{turb} = 777.36 \times \left(w/\delta\right)^{-1} \tag{6}$$

As shown in Figure 81, this alternate form and the original Equation 0 both fit the data to approximately the same accuracy. Then, making use of the fact that for these wind tunnel data, the shape factor (θ/δ) was nearly constant at ~ 7.35, substitution into Equation 0 resulted in a critical Reynolds number of:

$$\left(\mathrm{Re}_{w,e}\right)_{crit} = 777.36 \times \left(\frac{\delta}{w}\right)\left(\frac{w}{\theta}\right) = 777.36\left(\frac{\delta}{\theta}\right) = 777.36 \times 7.35 = 5699 \tag{7}$$

This constant critical Reynolds number for transition can then be mapped over an entire surface in order to determine where a cavity of a specified size would cause transition to turbulence at the cavity. An example is shown for a Mars flight case in Figure 82.

Application to Flight Conditions

Values of (w/δ) and Re_θ were computed for an attachment point cavity on the leeside of the heat shield along a typical trajectory. As shown in Figure 83, the correlations generated in this study indicate that the cavity would produce transition well before the peak heating point on the trajectory. Because this cavity-induced transition could produce heating levels in excess of natural turbulent heating levels (as was discussed in the Turbulent Aeroheating Section), and because the early transition due to the cavities would also result in a greater integrated heat load, the MSL design was revised. In the final design, the structural attachment points were moved from the forebody to the aftbody (the geometry of which has also changed) to eliminate the severe heating effects that they would produce.

Summary and Conclusions

An experimental and computational study of the effects of heat-shield cavities on boundary-layer transition and the aeroheating environment has been performed. This study was initiated because the original Mars Science Laboratory vehicle heat shield design included cavities through which bolts would pass to attach it to the carrier vehicle during transit to Mars.

Comparisons of measured heating levels and predictions were first conducted to assess the accuracy of the computational methods. For laminar cases, agreement to within the experimental uncertainty of ±13% was observed, but for turbulent cases measured heating data were generally 15% to 20% higher than turbulent predictions. This difference was thought to be due to the exclusion of the cavities from the computational geometry, as well as due to the use of a simple algebraic turbulence model. However, the possibility of a general bias in the computational method as compared to the data cannot be excluded.

The data on transition due to the presence of cavities were then analyzed to determine the post-cavity state of the boundary layer. Correlation equations for the laminar and fully turbulent boundaries in the data set were formulated in terms of the momentum Reynolds number based on boundary layer edge conditions Re_θ and the ratio of cavity diameter to boundary layer height (w/δ). Additionally, a critical Reynolds number $Re_{w,e}$ for transition due to cavities was also determined based on these data. These correlations were applied to typical MSL entry conditions and it was found that the presence of heat shield cavities would likely result in transition occurring well before the peak heating point in the trajectory and would produce heating levels in excess of those predicted for smooth-body transition to turbulence. In part because of these results, the heat-shield cavities were eliminated from the MSL design by relocating the attachment points to the aftbody of the vehicle.

Acknowledgements

The authors wish to thank the following individuals for their contributions to this work: Neil Cheatwood, John Ellis, Karl Edquist, Grace Gleason, Mark Griffith, Rhonda Manis, Ron Merski, Steve Nevins, Mike Powers and Gary Wainwright.

References

1. Lockwood, M. K., Powell, R. W., Graves, C. A., and Carman, G. L., "Entry System Design Considerations for Mars Landers," American Astronautical Society Paper AAS 01-023, 2001.

2. Lockwood, M. K., Powell, R. W., Sutton, K., Prabhu, R. K., Graves, C. A., Chirold, D. E., and Carman, G. L., "Entry Configurations and Performance Comparisons for the Mars Smart Lander," *Journal of Spacecraft & Rockets*, Vol. 43, No. 2, March-April 2006, pp. 258-269.

3. Liechty, D. S. and Hollis, B. R., "Heat Shield Parametric Experimental Aeroheating for a Mars Smart Lander," AIAA Paper 2002-2746, June, 2002.

4. Hollis, B. R. and Liechty, D. S., "Transition Due to Heat-Shield Cavities on a Mars Entry Vehicle," *Journal of Spacecraft & Rockets*, Vol. 43, No. 2, March-April 2006, pp. 354-366.

5. Liechty, D. S., Hollis, B. R., and Edquist, K. T., "Mars Science Laboratory Experimental Aerothermodynamics with Effects of Cavities and Control Surfaces," *Journal of Spacecraft & Rockets*, Vol. 43, No. 2, March-April 2006, pp. 340-353.

6. Edquist, K. T., Liechty, D. S., Hollis, B. R., Alter, S. J., and Loomis, M. L., "Aeroheating Environments for a Mars Smart Lander, *Journal of Spacecraft & Rockets*, Vol. 43, No. 2, March-April 2006, pp. 330-339.

7. Gnoffo, P. A., "An Upwind-Biased, Point-Implicit Algorithm for Viscous, Compressible Perfect-Gas Flows," NASA TP 2953, Feb. 1990.

8. Cheatwood, F. M., and Gnoffo, P. A., "User's Manual for the Langley Aerothermodynamic Upwind Relaxation Algorithm (LAURA)," NASA TM 4674, April, 1996.

9. Roe, P. L., "Approximate Riemann Solvers, Parameter Vectors and Difference Schemes," *Journal of Computational Physics*, Vol. 43, No. 2, 1981, pp. 357-372.

10. Harten, A., "High Resolution Schemes for Hyperbolic Conservation Laws," *Journal of Computational Physics*, Vol. 49, No. 3, 1983, pp. 357-393.

11. Yee, H. C., "On Symmetric and Upwind TVD Schemes," NASA TM 88325, 1990.

12. Baldwin, B. S. and Lomax, H., "Thin Layer Approximation and Algebraic Model for Separated Turbulent Flow," AIAA Paper 78-257, Jan. 1978.

13. Cheatwood, F. M., and Thompson, R. A., "The Addition of Algebraic Turbulence Modeling to Program LAURA," NASA TM-107758, April 1993.

14. Dhawan. S., and Narashima, R., "Some Properties of Boundary Layer Flow from Laminar to Turbulent Motion," *Journal of Fluid Mechanics*, Vol. 1, Part 4, pp. 418-436, Jan. 1958.

15. Micol, J. R. "Hypersonic Aerodynamic/ Aerothermodynamic Testing Capabilities at Langley Research Center: Aerothermodynamic Facilities Complex," AIAA Paper 95-2107, June 1995.

16. Micol, J. R. "Langley Aerothermodynamic Facilities Complex: Enhancements and Testing Capabilities," AIAA Paper 98-0147, Jan. 1998.

17. Hollis, B. R., "Real-Gas Flow Properties for NASA Langley Research Center Aerothermodynamic Facilities Complex Wind Tunnels," NASA CR-4755, September, 1996.

18. Buck, G. M., "Automated Thermal Mapping Techniques Using Chromatic Image Analysis," NASA TM 101554, April 1989.

19. Buck, G. M., "Surface Temperature/Heat Transfer Measurement Using a Quantitative Phosphor Thermography System," AIAA Paper 91-0064, Jan. 1991.

20. Merski, N. R., "A Relative-Intensity, Two-Color Phosphor Thermography System," NASA TM 104123, Sept. 1991.

21. Merski, N. R., "Global Aeroheating Wind-Tunnel Measurements Using Improved Two-Color Phosphor Thermography Methods, *Journal of Spacecraft and Rockets*, Vol. 36, No. 2, pp. 160-170, March-April 1999.

22. Fay, J. A., and Riddell, F. R., "Theory of Stagnation Point Heat Transfer in Dissociated Air," *Journal of Aeronautical Sciences*, Vol. 25, No. 2., pp. 73-85, Feb. 1958.

23. Buck, G. M., and Vasquez, P., "An Investment Ceramic Slip-Casting Technique for Net-Form, Precision, Detailed Casting of Ceramic Models," U. S. Patent 5,266,252, Nov. 1993.

24. Cheatwood, F. M., Merski, N. R., Riley, C. J., and Mitchletree, R. A., "Aerothermodynamic Environment Definition for the Genesis Sample Return Capsule," AIAA Paper 2001-2889, June, 2001.

25. Reda, D. C., "A Review and Synthesis of Roughness-Dominated Transition Correlations for Re-entry Applications," *Journal of Spacecraft and Rockets*, Vol. 39, No. 2., pp. 161-167, May-June 1998.

26. Berry, S. A., Bouslog, S. A., Brauckmann, G. J., and Caram, J. M., "Shuttle Orbiter Experimental Boundary-Layer Results with Isolated Roughness," *Journal of Spacecraft and Rockets*, Vol. 35, No. 3., pp. 241-248, May-June 1998.

27. Bouslog, S. A., Bertin, J. J., Berry, S. A., Caram, J. M., "Isolated Roughness Induced Boundary-Layer Transition: Shuttle Orbiter Ground Tests and Flight Experience," AIAA Paper 97-0274, January 1997.

28. Bertin, J. J. and Hayden, T. E., "Comparison of Correlations of Shuttle Boundary-Layer Transition Due to Distributed Roughness," AIAA Paper 81-0417, January 1981.

29. Berry, S. A., Horvath, T. J., Hollis, B. R., Thompson, R. A., and Hamilton, H. H. II, "X-33 Hypersonic Boundary Layer Transition," *Journal of Spacecraft and Rockets*, Vol. 38, No. 5., pp. 646-657, September-October 2001.

30. Horvath, T. J., Berry, S. A., Merski, N. R., and Fitzgerald, S. M., X-38 Experimental Aerothermodynamics," AIAA Paper 2000-2685, June, 2000.

31. Todisco, A, Reeves, B., Siegelman, D., and Mascola, R., "Boundary Layer Transition on Blunt Axisymmetric Nosetips Induced by Single and Multiple Craters," AIAA Paper 81-1087, June 1981.

32. Charwat, A. F., Roos, J. N., Dewey, C. F., and Hitz, J. A., "An Investigation of Separated Flows - Part I: The Pressure Field," *Journal of the Aerospace Sciences*, Vol. 28, No. 6, June 1961, pp. 457-470.

33. Nestler, D. E., "An Experimental Study of Cavity Flow on Sharp and Blunt Cones at Mach 8," AIAA Paper 81-0335, Jan. 1981

34. Zhang, J., Morishita, E., Okunuki, T., and Itoh, H., "Experimental and Computational Investigation of Supersonic Cavity Flows," AIAA Paper 2001-1755, April 2001.

35. Stetson, K. F., "Boundary-Layer Transition on Blunt Configurations," NASA-JSC-26528, Feb. 1994.

36. Schiller, L., "Flow in Pipes", Handbook of Experimental Physics, Vol. 4, Pt. 4, Academic Press, Leipzig, Germany, 1932, pp. 189-192.

37. Poll, D. I. A., "The Effect of Isolated Roughness Elements on Transition in Attachment-Line Flows," Laminar-Turbulent Transition, edited by D. Arnal and R. Michel, Springer-Verlag, New York, 1990, pp. 657-667.

38. Bouslog, S. A., Bertin, J. J., Berry, S. A., and Caram, J. M., "Isolated Roughness Induced Boundary-Layer Transition: Shuttle Orbiter Ground Tests and Experience," AIAA Paper 97-0274, Jan. 1997.

Tables

Table 1. Nominal Flow Conditions for 20-Inch Mach 6 Air Tunnel MSL Test

Condition	M_∞	T_∞ (K)	ρ_∞ (kg/m^3)	U_∞ (m/s)	Re_∞ (1/m)	h_{FR} (kg/m^2-s)	q_{FR} (W/cm^2)
$Re_\infty = 2.1\text{x}10^6$/ft	5.95	62.0	$3.35\text{x}10^{-2}$	938.6	$7.07\text{x}10^6$	0.283	5.70
$Re_\infty = 2.6\text{x}10^6$/ft	5.97	62.2	$4.05\text{x}10^{-2}$	943.0	$8.55\text{x}10^6$	0.313	6.45
$Re_\infty = 3.0\text{x}10^6$/ft	5.98	62.2	$4.62\text{x}10^{-2}$	944.4	$9.79\text{x}10^6$	0.335	6.95
$Re_\infty = 3.4\text{x}10^6$/ft	5.99	61.6	$5.29\text{x}10^{-2}$	940.1	$1.13\text{x}10^7$	0.356	7.25
$Re_\infty = 4.2\text{x}10^6$/ft	6.00	61.3	$6.41\text{x}10^{-2}$	940.4	$1.37\text{x}10^7$	0.392	7.95
$Re_\infty = 4.6\text{x}10^6$/ft	6.01	63.5	$7.25\text{x}10^{-2}$	958.5	$1.52\text{x}10^7$	0.427	9.48
$Re_\infty = 5.1\text{x}10^6$/ft	6.02	63.4	$7.92\text{x}10^{-2}$	958.7	$1.67\text{x}10^7$	0.446	9.92
$Re_\infty = 5.8\text{x}10^6$/ft	6.03	62.8	$8.99\text{x}10^{-2}$	955.6	$1.91\text{x}10^7$	0.474	10.4
$Re_\infty = 7.3\text{x}10^6$/ft	6.06	62.3	$1.13\text{x}10^{-1}$	954.6	$2.41\text{x}10^7$	0.529	11.5

Table 2. Cavity Parameters for Baseline Model B-5-PA-2

Cavity	r/R	w_{fs} (in)	k_{fs} (in)	w/k	w_{ms} (in)	k_{ms} (in)
1	0.70	2.74	0.844	3.246	0.0859	0.0265
2	0.70	1.75	0.608	2.878	0.0549	0.0191
3	0.70	1.58	0.513	3.080	0.0495	0.0161
4	0.41	2.58	0.895	2.833	0.0809	0.0281
5	0.41	1.83	0.382	4.791	0.0574	0.0120
6	0.41	1.37	0.366	3.743	0.0430	0.0115
Model Scale = 0.031358						

Table 3. Cavity Parameters for Baseline Model B-5-PA-3

Cavity	r/R	w_{fs} (in)	k_{fs} (in)	w/k	w_{ms} (in)	k_{ms} (in)
1	0.70	3.41	0.710	4.803	0.1069	0.0223
2	0.70	2.69	0.774	3.475	0.0844	0.0243
3	0.70	1.74	0.777	2.239	0.0546	0.0244
4	0.41	3.51	0.656	5.351	0.1101	0.0206
5	0.41	2.34	0.408	5.735	0.0734	0.0128
6	0.41	1.62	0.583	2.779	0.0508	0.0183
Model Scale = 0.031358						

Table 4. Cavity Parameters for "Tab" Control Surface Model T-5-1C-1

Cavity	r/R	w_{fs} (in)	k_{fs} (in)	w/k	w_{ms} (in)	k_{ms} (in)
1	0.41	1.50	NA	NA	0.0469	NA
2	0.41	1.58	NA	NA	0.0496	NA
3	0.41	1.59	NA	NA	0.0499	NA
4	0.41	1.52	NA	NA	0.0478	NA
5	0.41	1.50	NA	NA	0.0469	NA
6	0.41	1.63	NA	NA	0.0512	NA
Model Scale = 0.031358						

Table 5. Cavity Parameters for "Tab" Control Surface Model T-5-3B-1

Cavity	r/R	w_{fs} (in)	k_{fs} (in)	w/k	w_{ms} (in)	k_{ms} (in)
1	0.41	2.80	0.836	3.355	0.0879	0.0262
2	0.41	2.68	0.867	3.092	0.0841	0.0272
3	0.41	2.74	0.867	3.162	0.0860	0.0272
4	0.41	2.88	0.896	3.214	0.0903	0.0281
5	0.41	2.90	0.976	2.967	0.0908	0.0306
6	0.41	2.75	0.848	3.241	0.0862	0.0266
Model Scale = 0.031358						

Table 6. Cavity Parameters for "Tab" Control Surface Model T-5-3C-1

Cavity	r/R	w_{fs} (in)	k_{fs} (in)	w/k	w_{ms} (in)	k_{ms} (in)
1	0.41	2.65	0.662	4.001	0.0831	0.0208
2	0.41	2.94	0.994	2.959	0.0922	0.0312
3	0.41	3.03	0.854	3.550	0.0950	0.0268
4	0.41	3.00	0.806	3.728	0.0942	0.0253
5	0.41	2.99	0.825	3.630	0.0939	0.0259
6	0.41	2.97	0.812	3.656	0.0931	0.0255
Model Scale = 0.031358						

Table 7. Cavity Parameters for Old Genesis Model

Cavity	r/R	w_{fs} (in)	k_{fs} (in)	w/k	w_{ms} (in)	k_{ms} (in)
1	0.70	1.00	0.300	3.333	0.1000	0.0300
2	0.40	2.00	0.300	6.667	0.2000	0.0300
3	0.40	1.00	0.300	3.333	0.1000	0.0300
4	0.70	0.50	0.300	1.667	0.0500	0.0300
5	0.70	2.00	0.300	6.667	0.2000	0.0300
6	0.70	1.00	0.600	1.667	0.1000	0.0600
Model Scale = 0.1000						
Note: these are parameters specified, not as built						

Table 8. Cavity Parameters for New Genesis Model G-5-PA-1

Cavity	r/R	w_{fs} (in)	k_{fs} (in)	w/k	w_{ms} (in)	k_{ms} (in)
1	0.70	0.87	0.132	6.564	0.0722	0.0110
2	0.40	1.88	0.218	8.621	0.1569	0.0182
3	0.40	0.95	0.220	4.306	0.0788	0.0183
4	0.70	0.52	0.126	4.143	0.0435	0.0105
5	0.70	1.91	0.125	15.30	0.1591	0.0104
6	0.70	0.70	0.185	3.812	0.0587	0.0154
Model Scale = 0.0833						

Figures

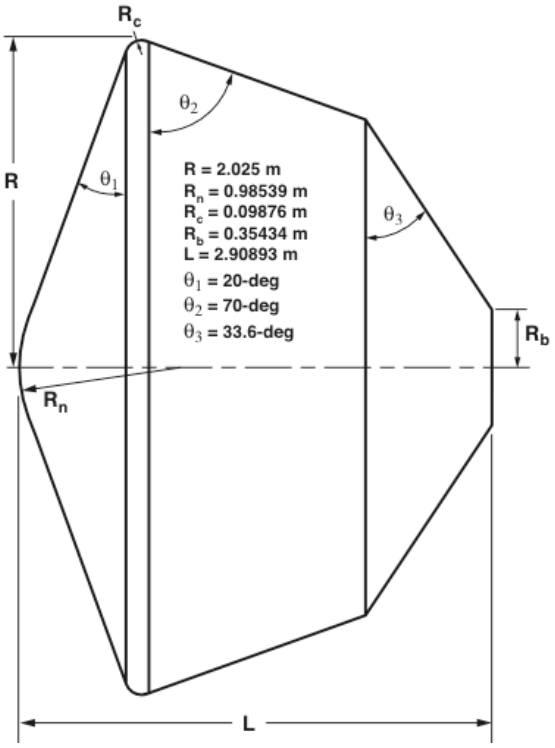

(dimensions are relevant to configuration in 2004)

Figure 1. Geometry and Dimensions of Full-Scale Mars Science Laboratory

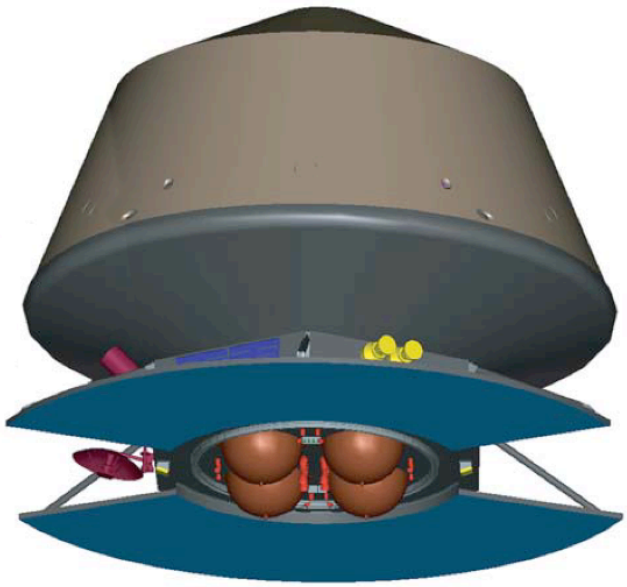

Figure 2. Entry Vehicle Attached to Cruise Stage

Figure 3. MSL Control Surface Parametric Models

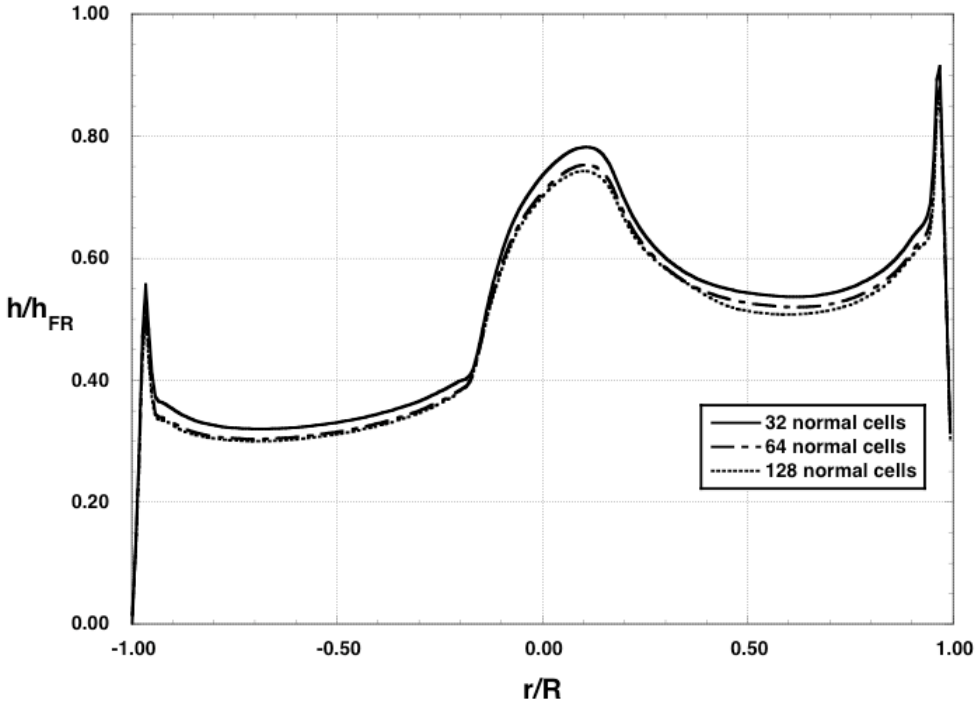

Figure 4. Effects of Normal Grid Resolution on Centerline Heating Levels, α=16, Re_∞=7.3x10^6/ft

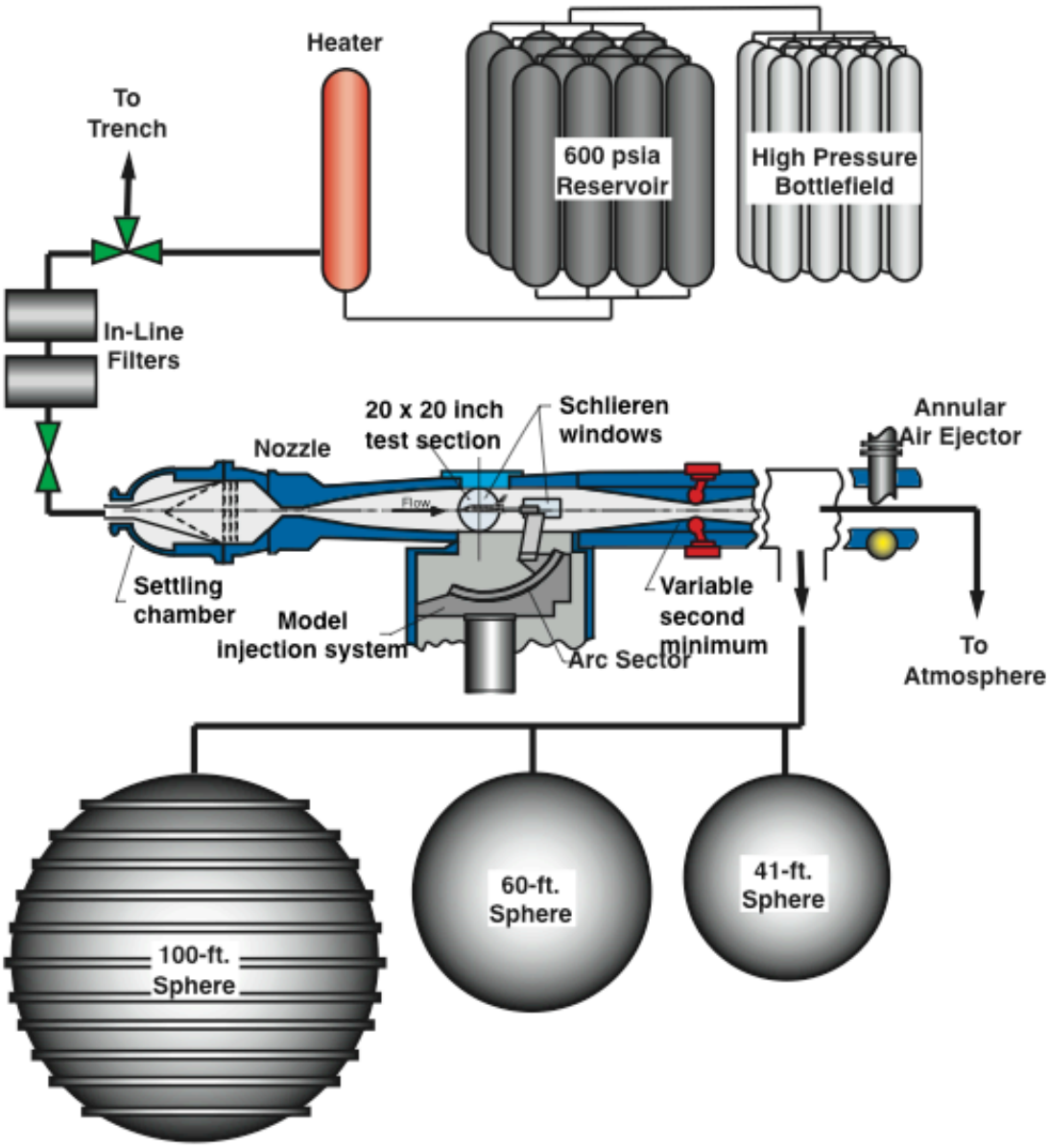

Figure 5. NASA LaRC 20-Inch Mach 6 Air Tunnel

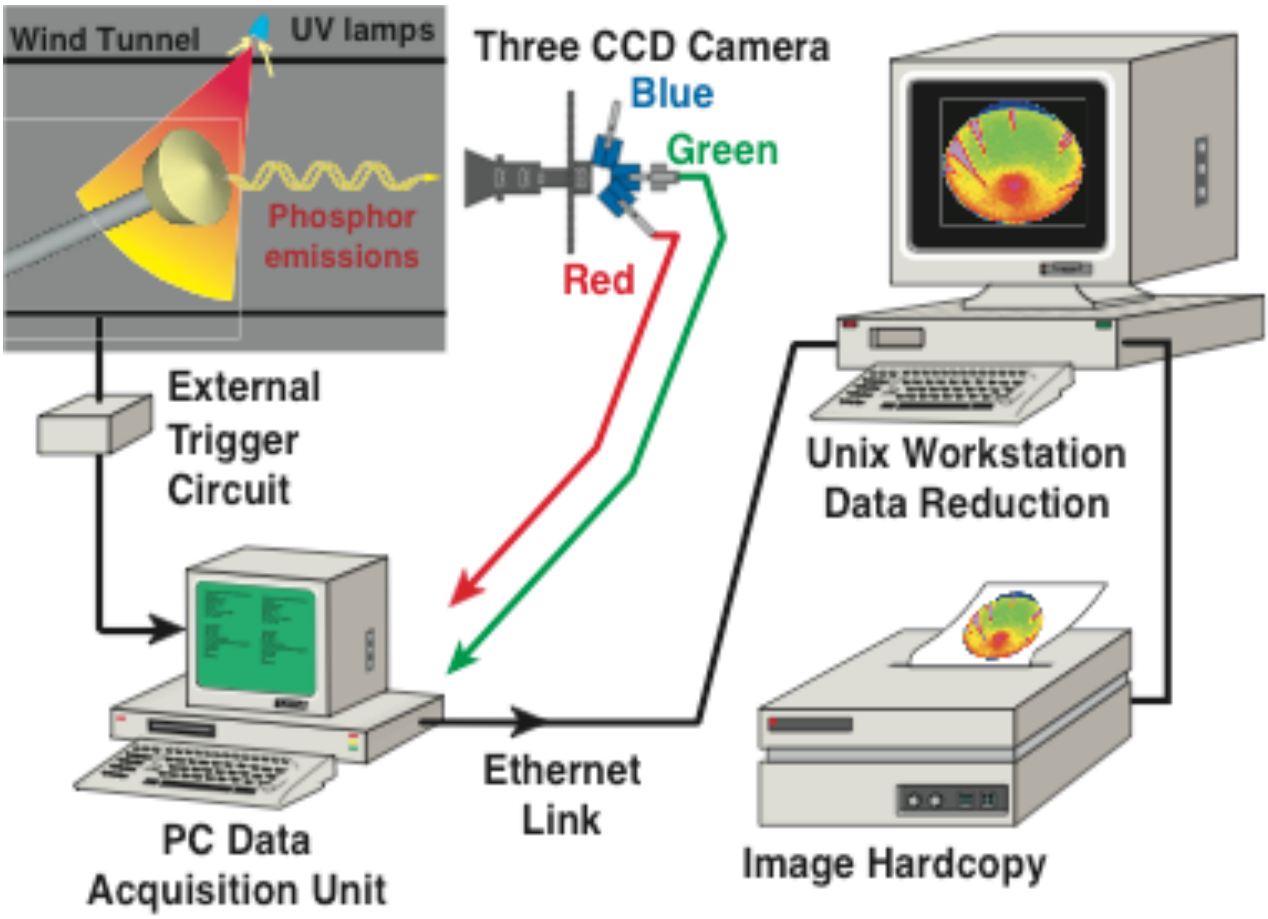

Figure 6. Schematic of Langley Two-Color Thermographic Phosphor System

Figure 7. Ceramic MSL Models

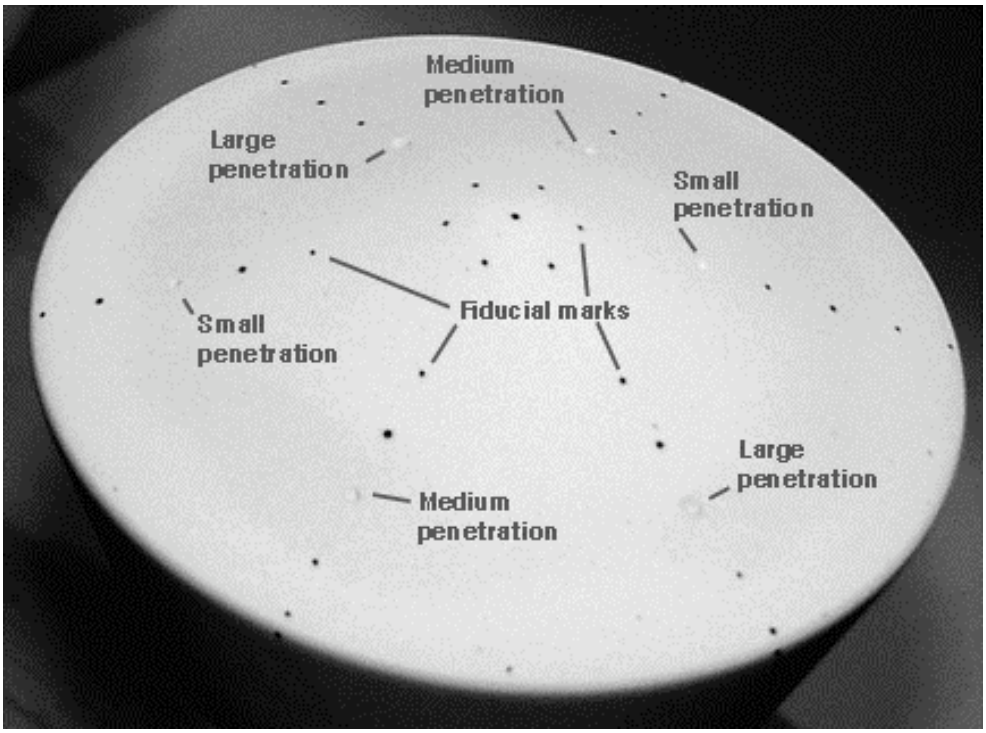

Figure 8. Photograph of Cavities on MSL Model

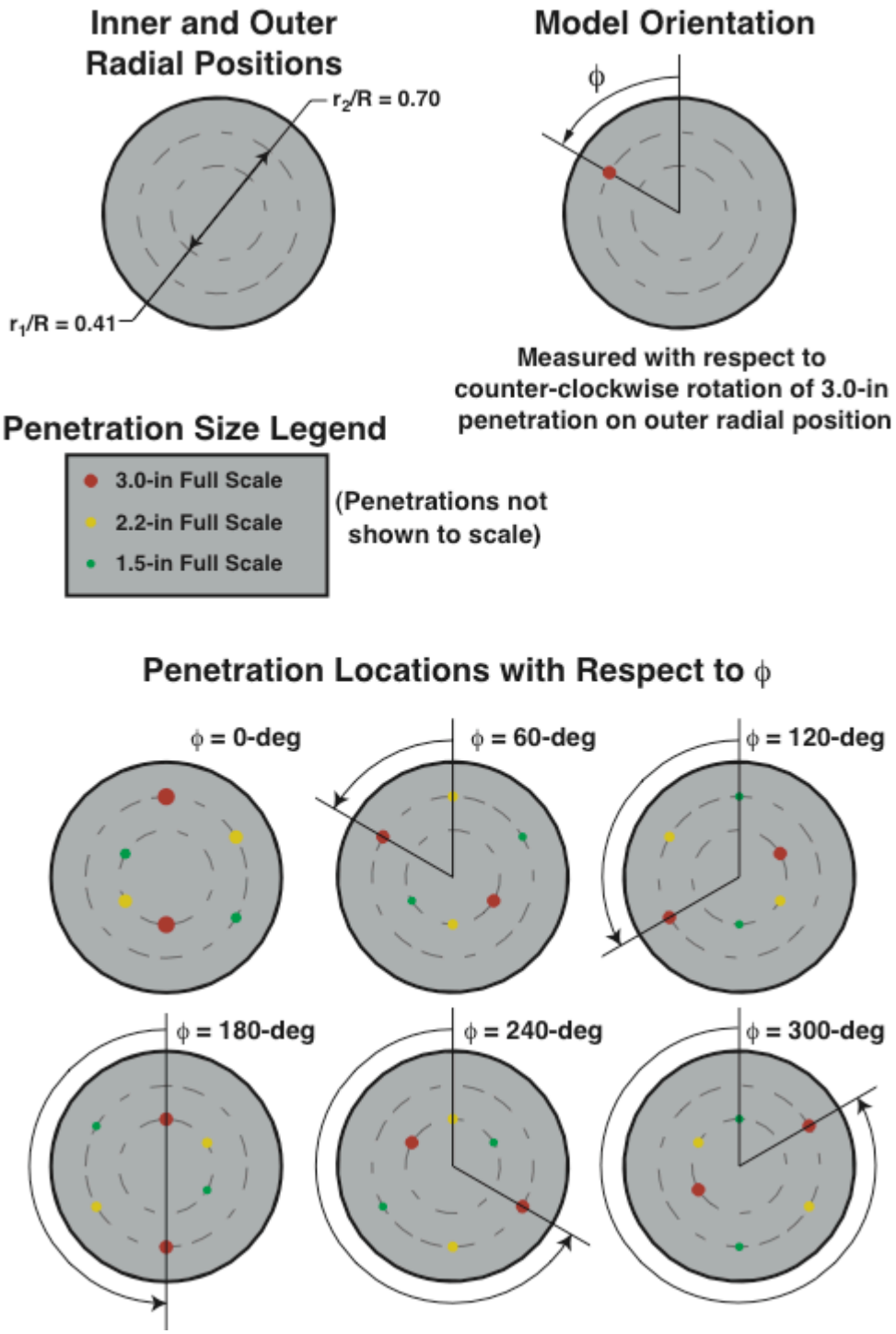

Figure 9. Cavity Layout on Baseline Models

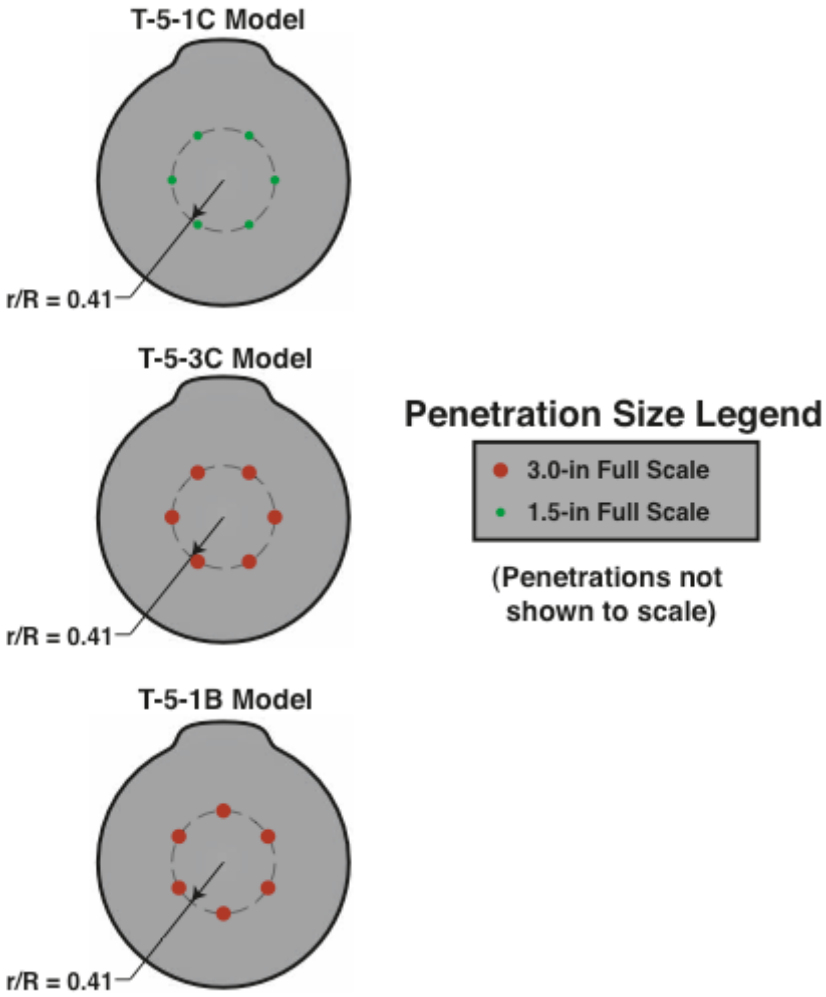

Figure 10. Cavity Layout on "Tab" Control Surface Models

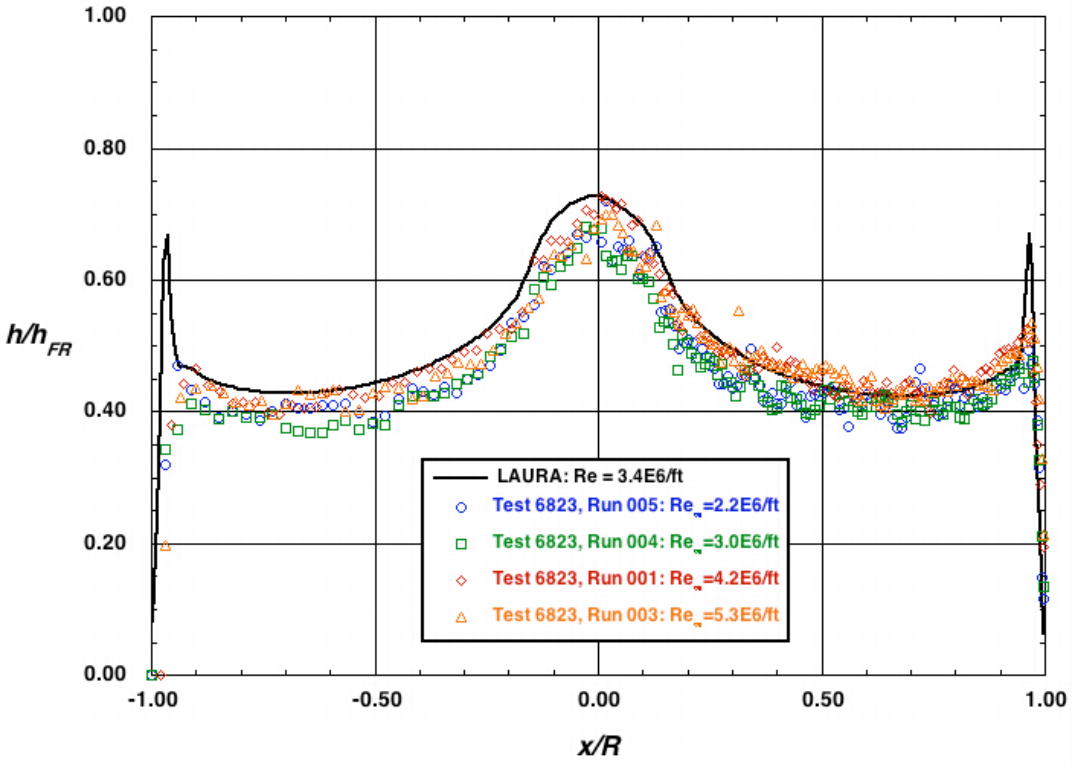

Figure 11. Comparison of Baseline Model Data with Laminar Predictions at α = 0-deg

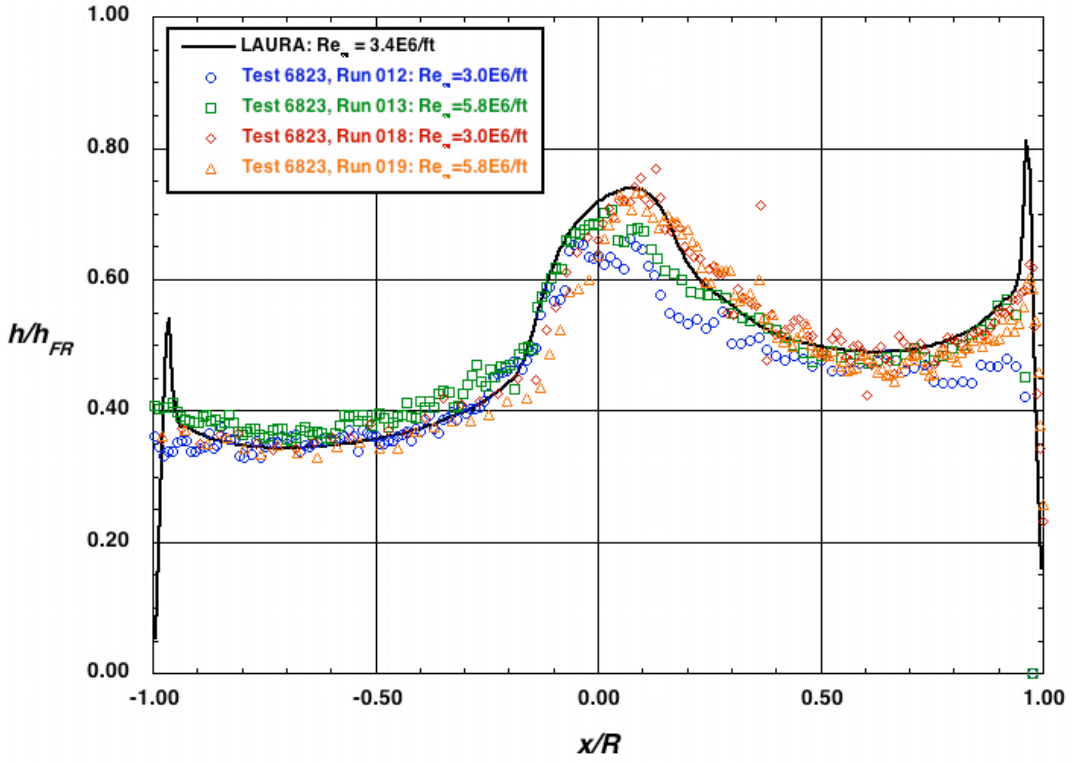

Figure 12. Comparison of Baseline Model Data with Laminar Predictions at α = 11-deg

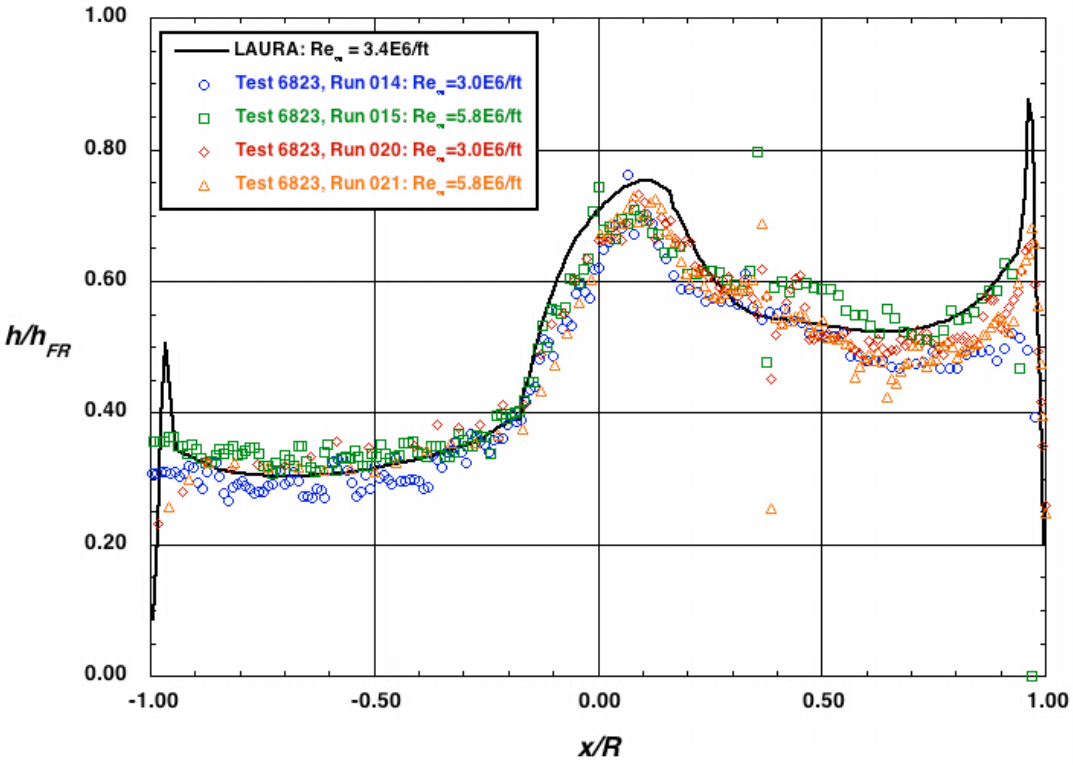

Figure 13. Comparison of Baseline Model Data with Laminar Predictions at α = 16-deg

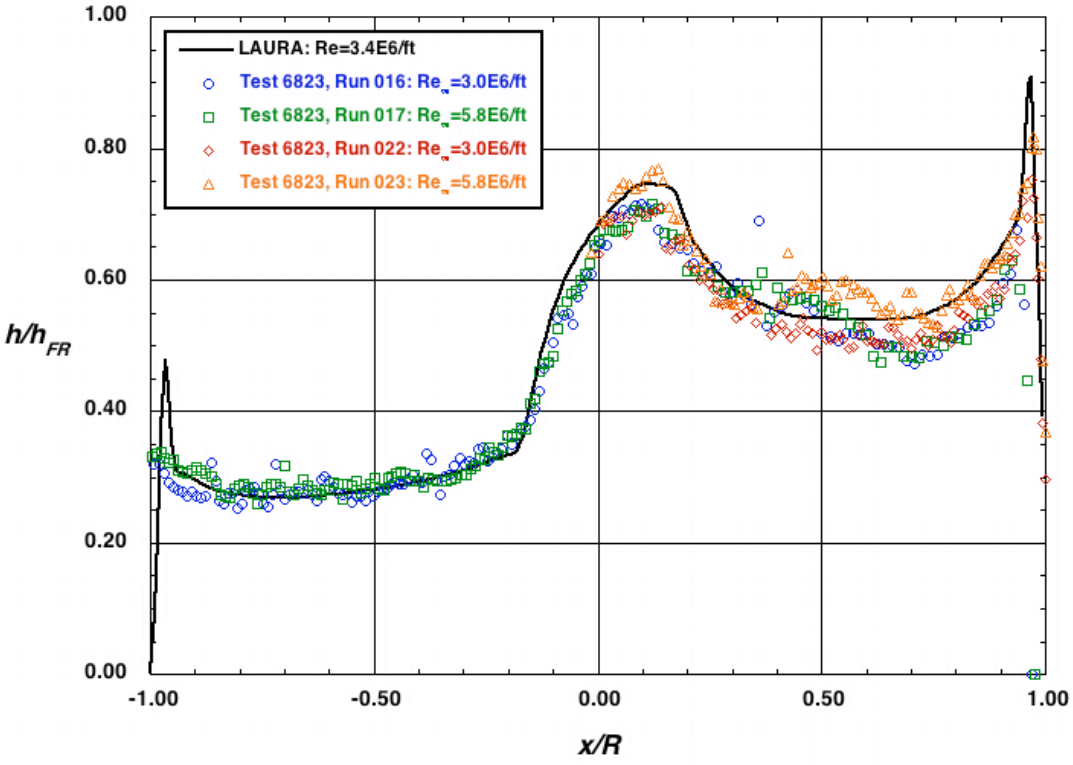

Figure 14. Comparison of Baseline Model Data with Laminar Predictions at α = 20-deg

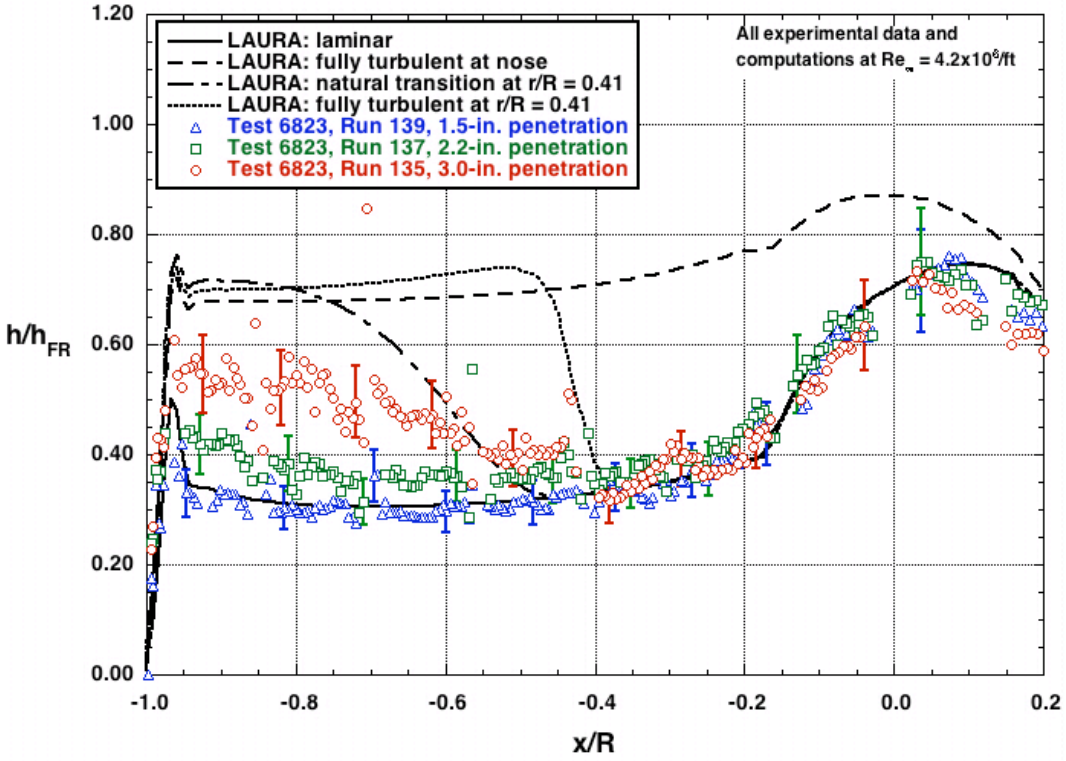

Figure 15. Comparison of Data and Turbulent Predictions for α = 16-deg, Re_∞ = 4.2E6/ft, r/R = 0.41

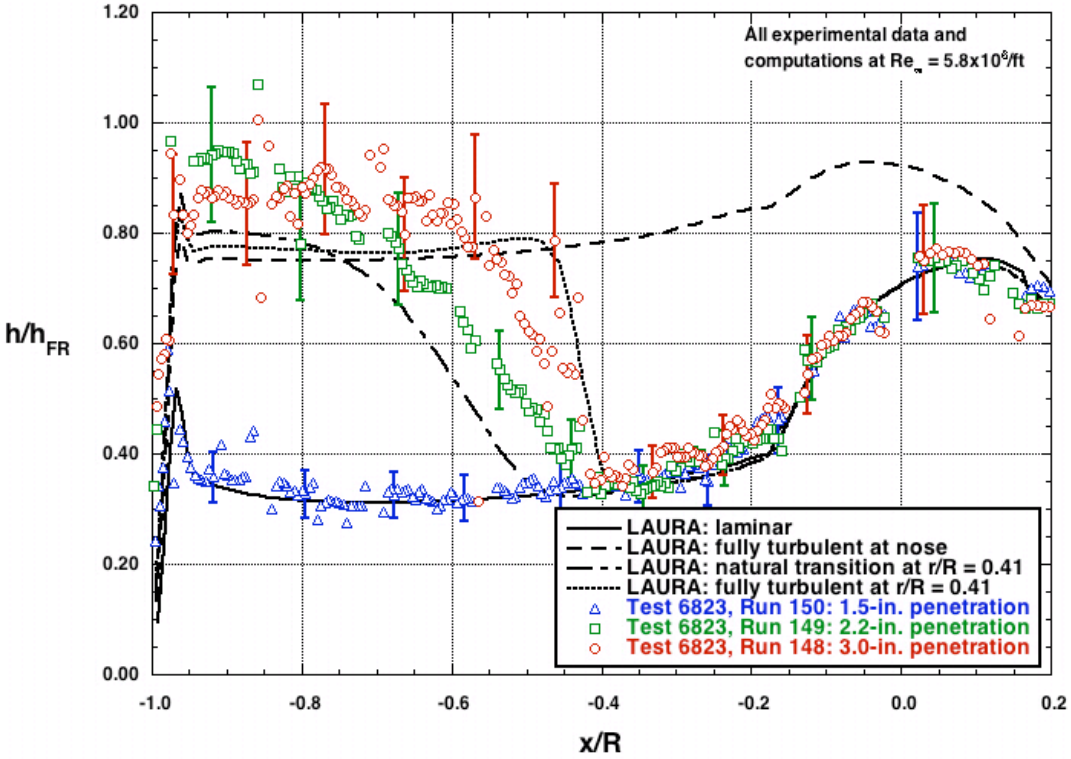

Figure 16. Comparison of Data and Turbulent Predictions for α = 16-deg, Re_∞ = 5.8E6/ft, r/R = 0.41

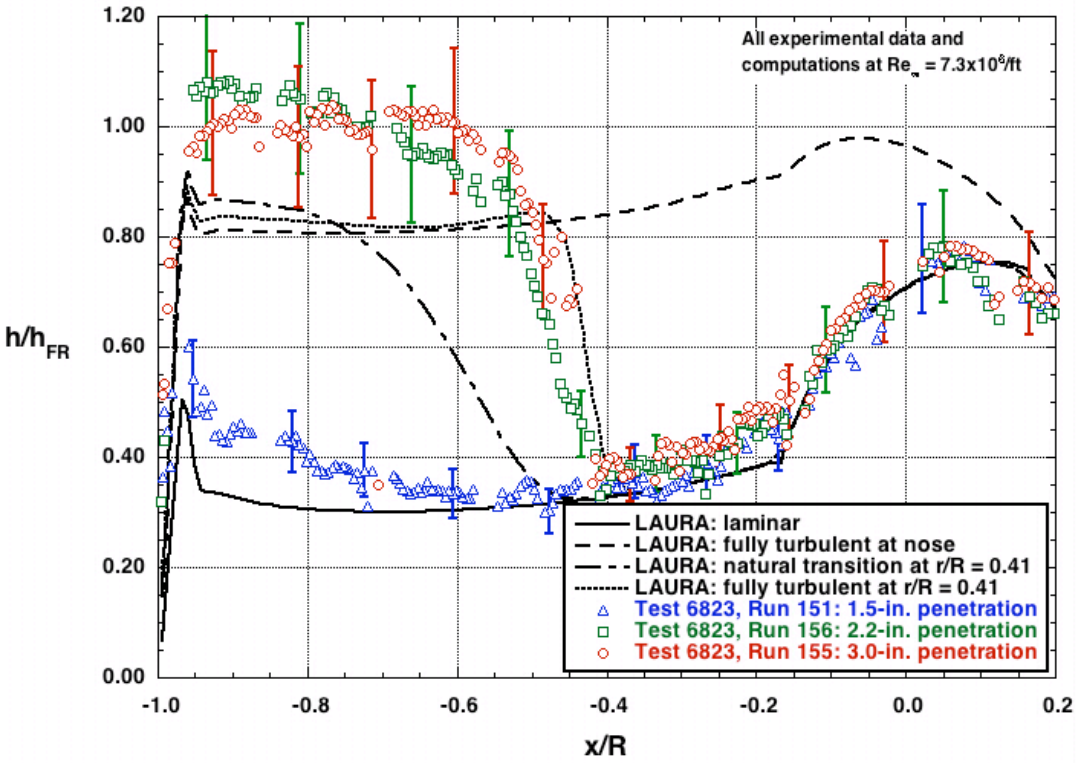

Figure 17. Comparison of Data and Turbulent Predictions for α = 16-deg, Re_∞ = 7.3E6/ft, r/R = 0.41

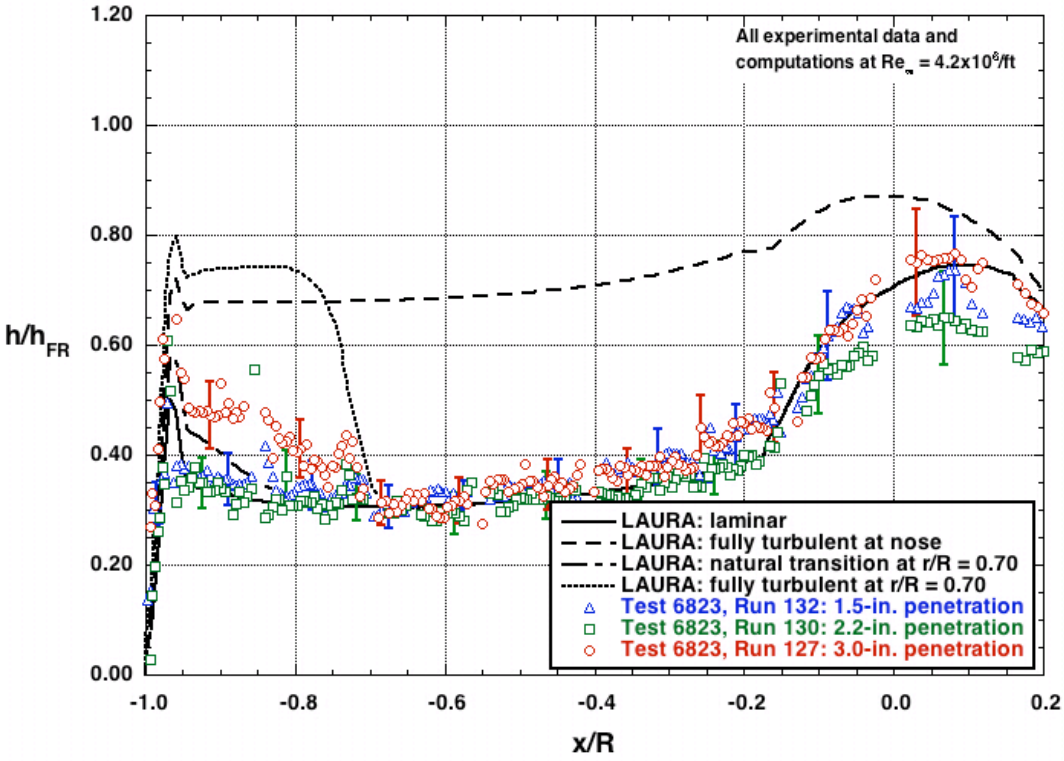

Figure 18. Comparison of Data and Turbulent Predictions for α = 16-deg, Re_∞ = 4.2E6/ft, r/R = 0.70

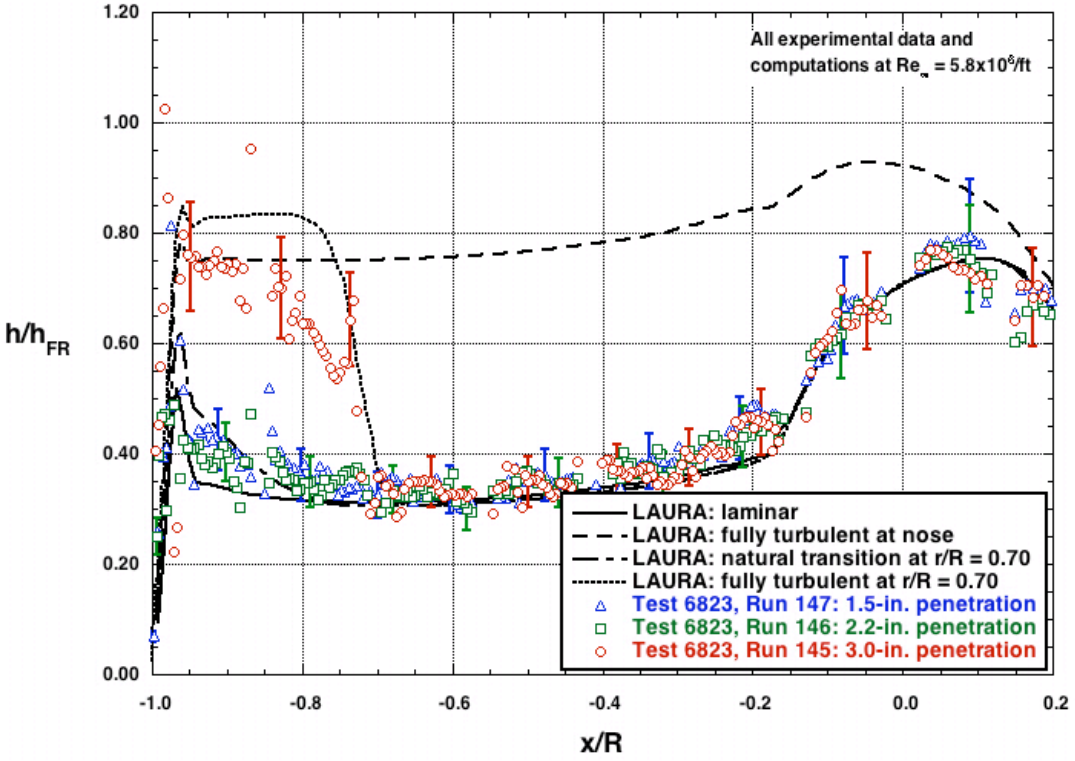

Figure 19. Comparison of Data and Turbulent Predictions for α = 16-deg, Re_∞ = 5.8E6/ft, r/R = 0.70

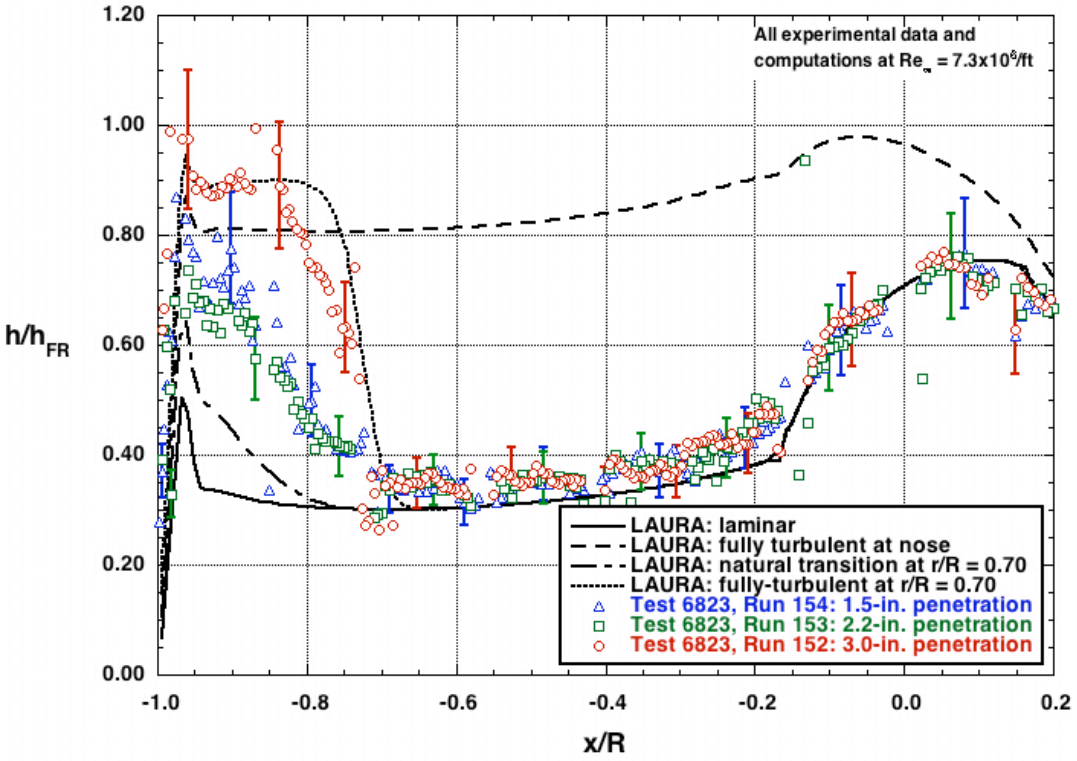

Figure 20. Comparison of Data and Turbulent Predictions for α = 16-deg, Re_∞ = 7.3E6/ft, r/R = 0.70

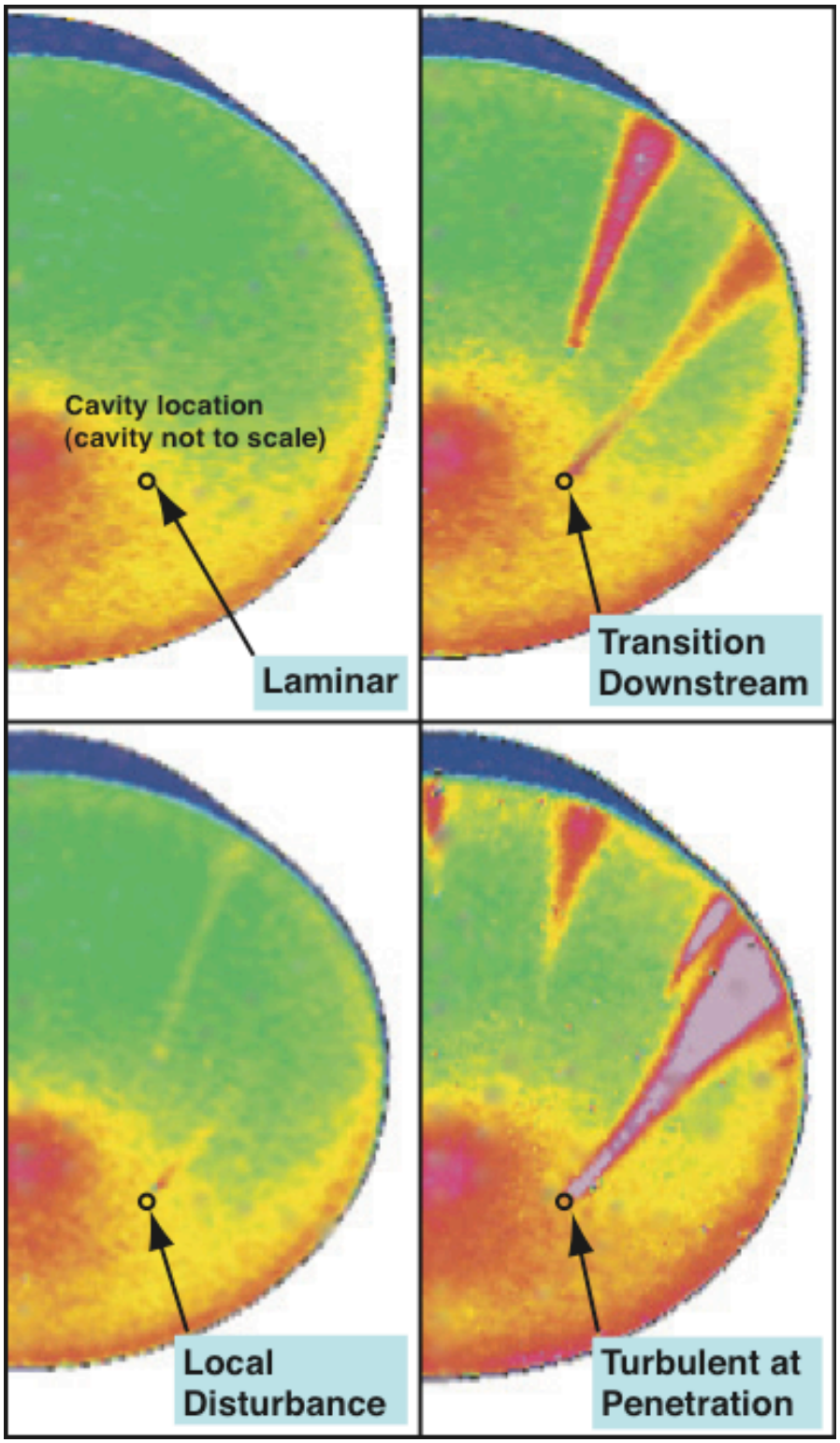

Figure 21. Classification of Cavity Effects on Boundary-Layer State

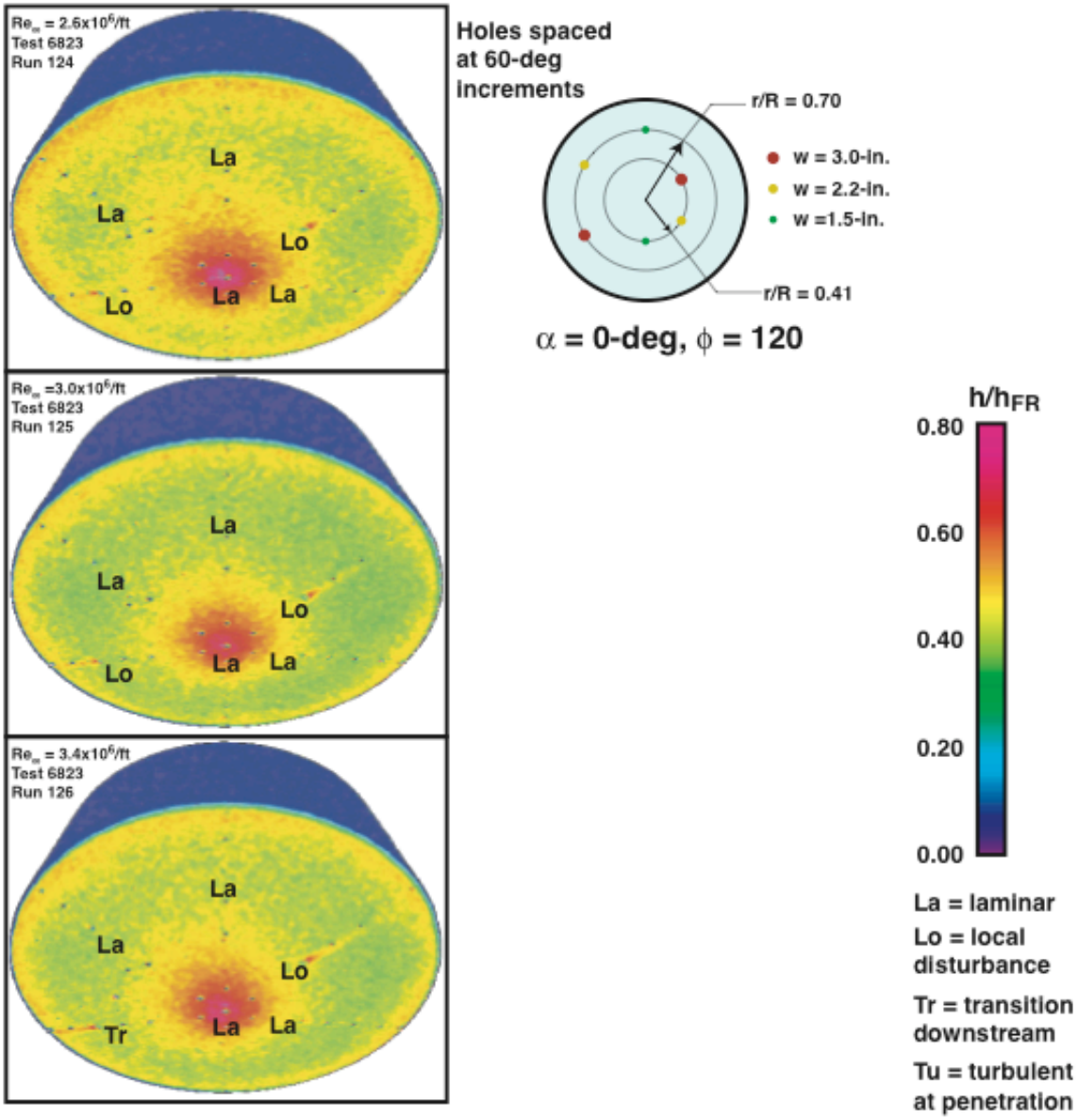

Figure 22. Cavity Effects on Heating, Baseline B-5-PA-2 Model, α = 0-deg, ϕ = 120-deg

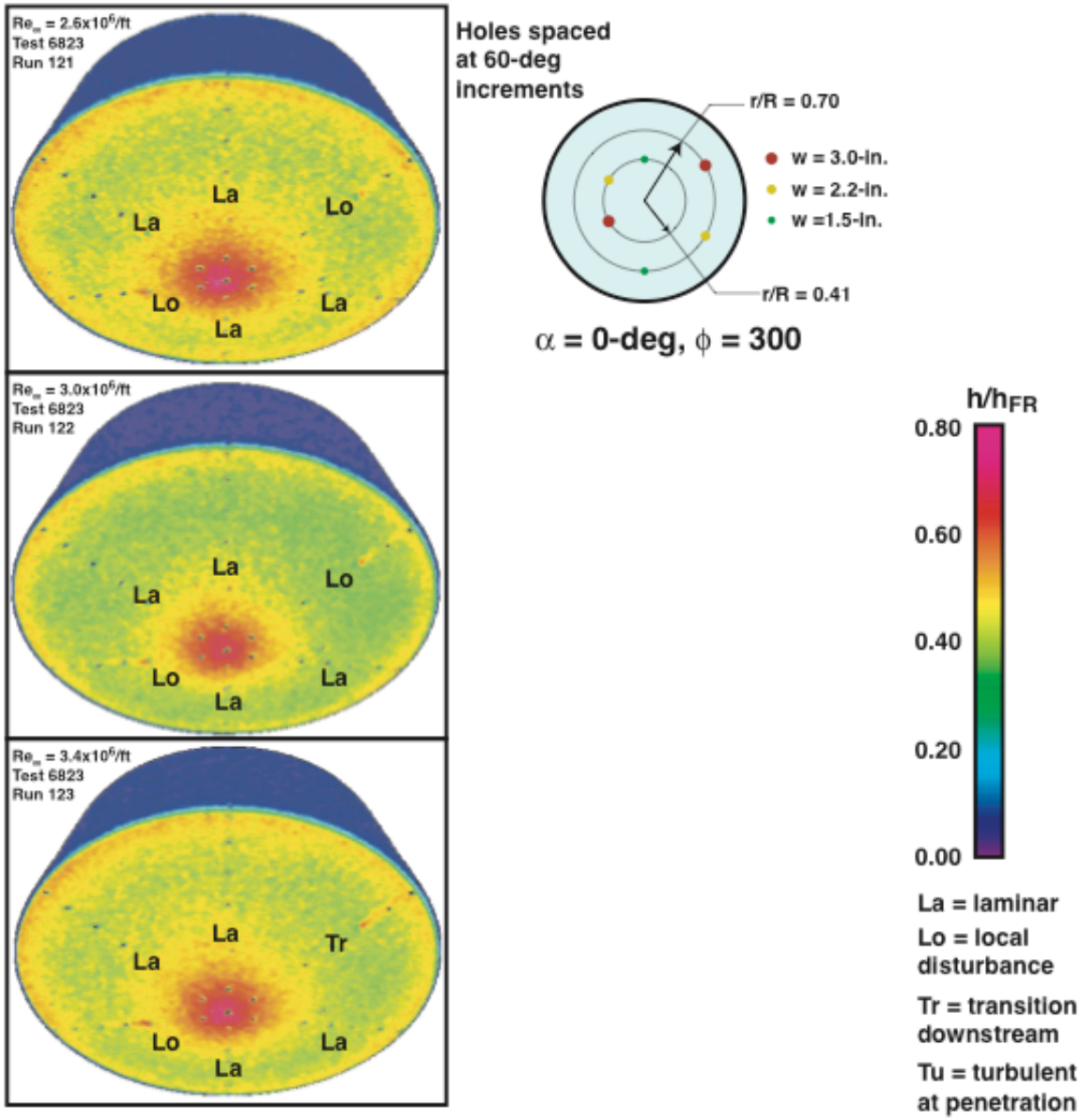

Figure 23. Cavity Effects on Heating, Baseline B-5-PA-2 Model, α = 0-deg, ϕ = 300-deg

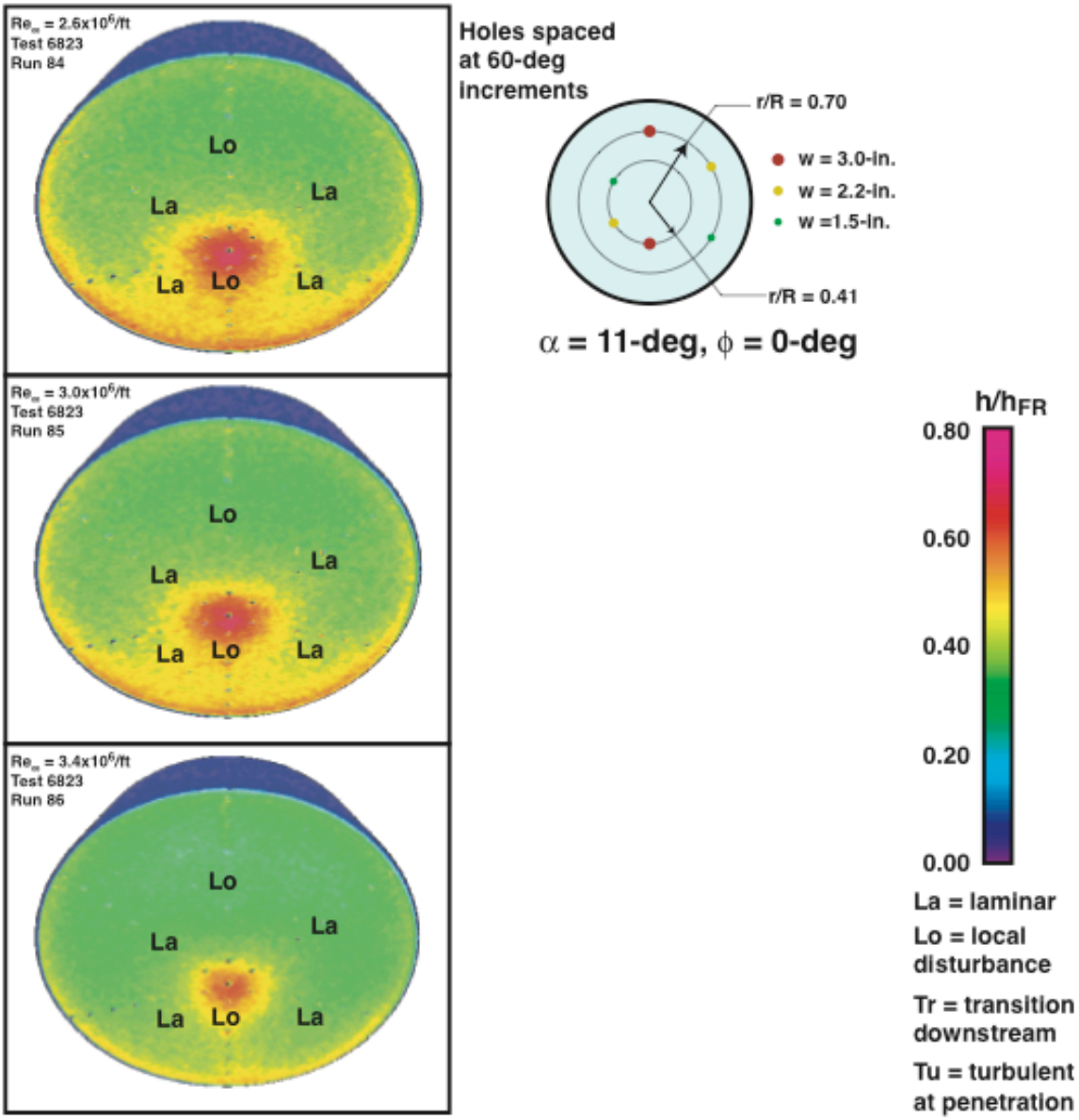

Figure 24. Cavity Effects on Heating, Baseline B-5-PA-2 Model, α =11-deg, ϕ = 0-deg

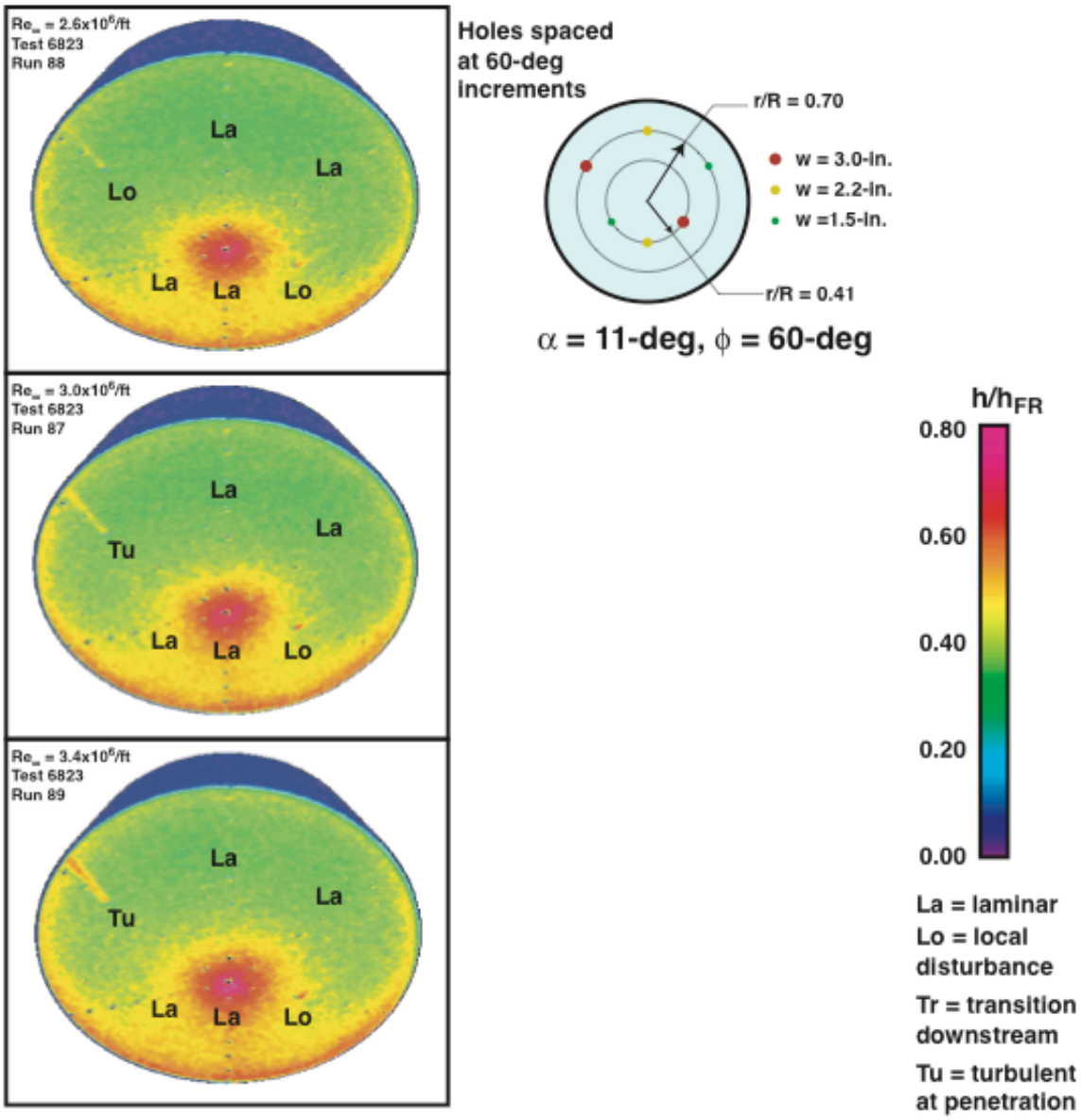

Figure 25. Cavity Effects on Heating, Baseline B-5-PA-2 Model, α = 11-deg, ϕ = 60-deg

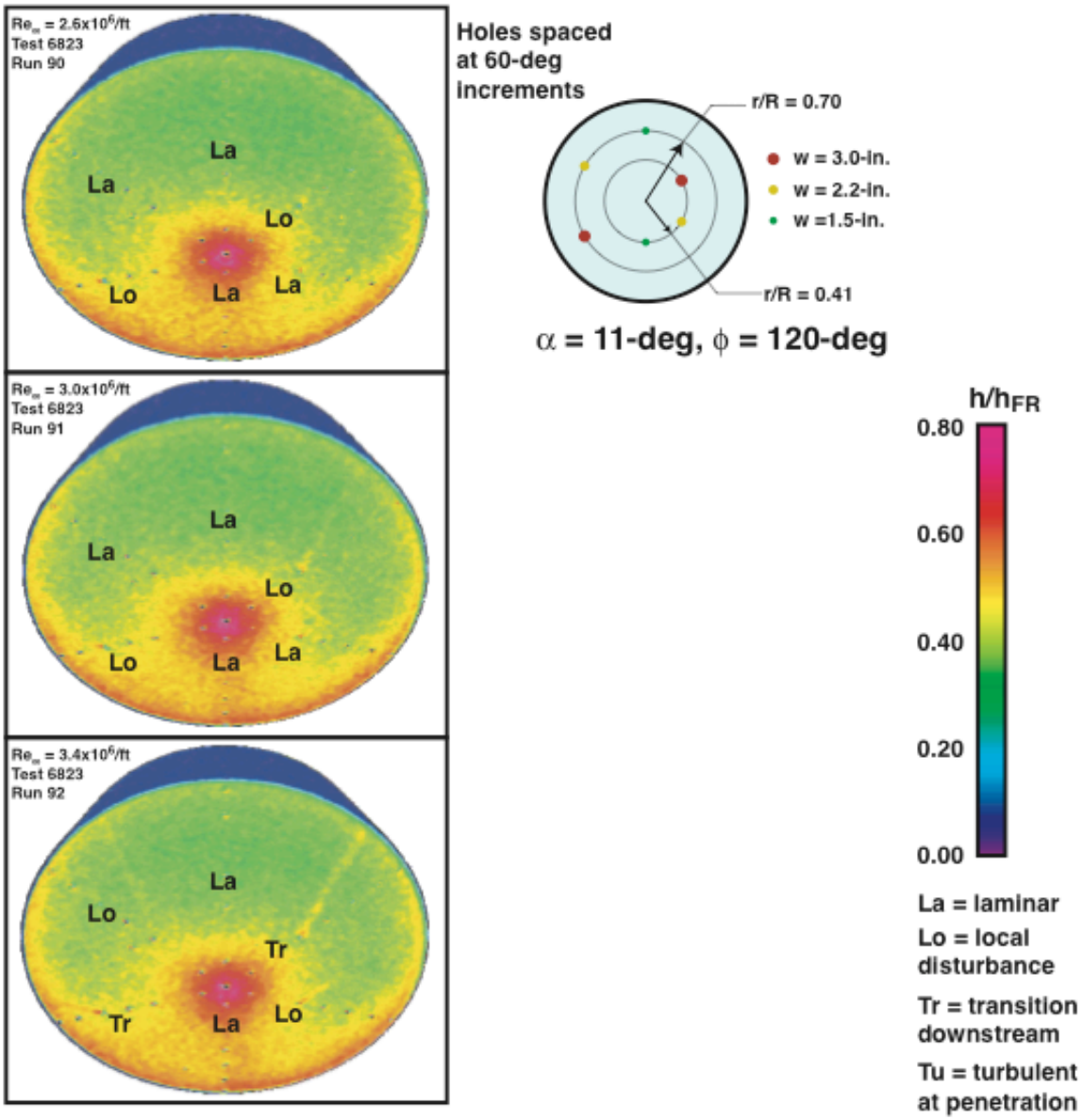

Figure 26. Cavity Effects on Heating, Baseline B-5-PA-2 Model, α = 11-deg, ϕ = 120-deg

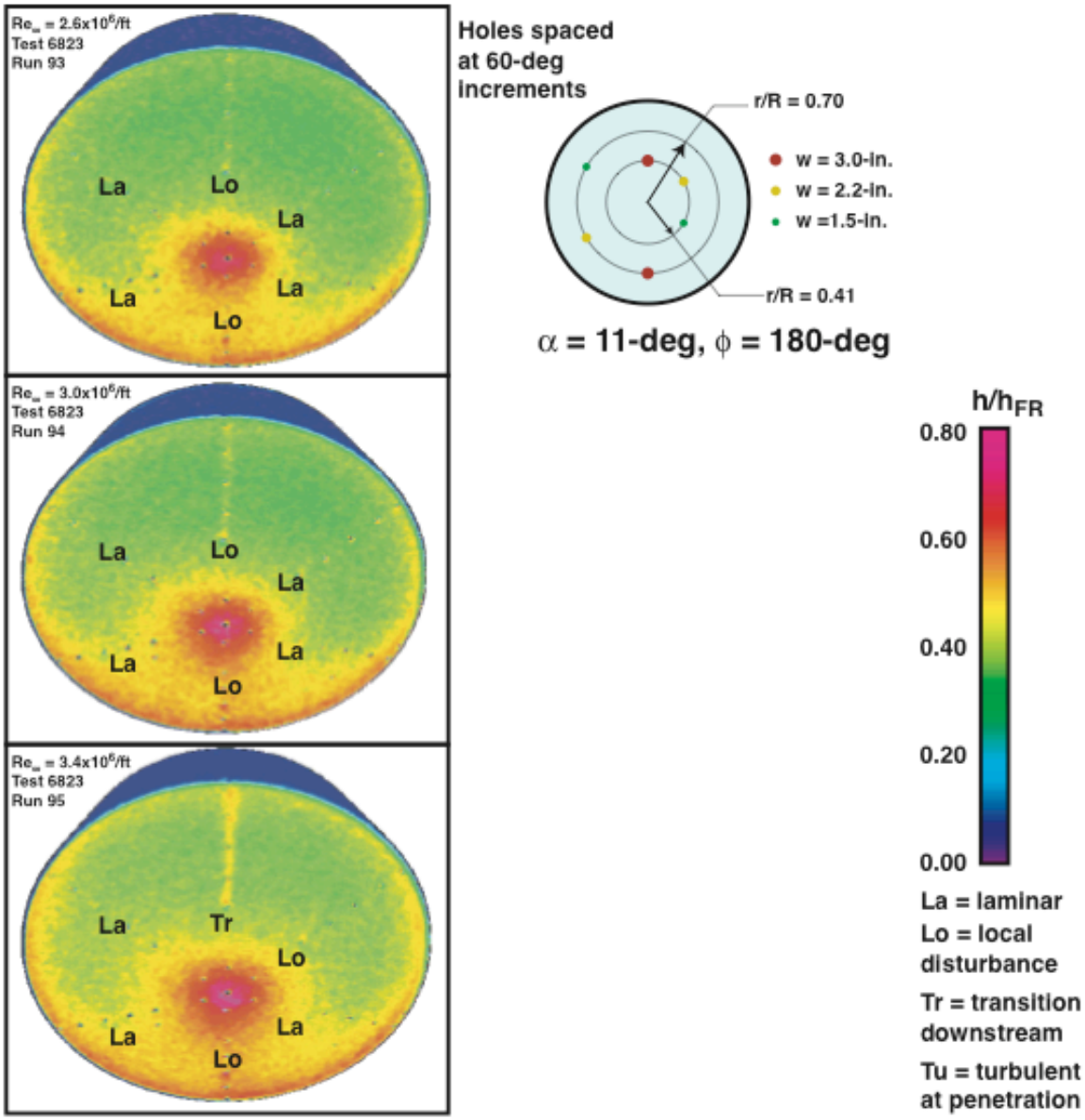

Figure 27. Cavity Effects on Heating, Baseline B-5-PA-2 Model, α = 11-deg, ϕ = 180-deg

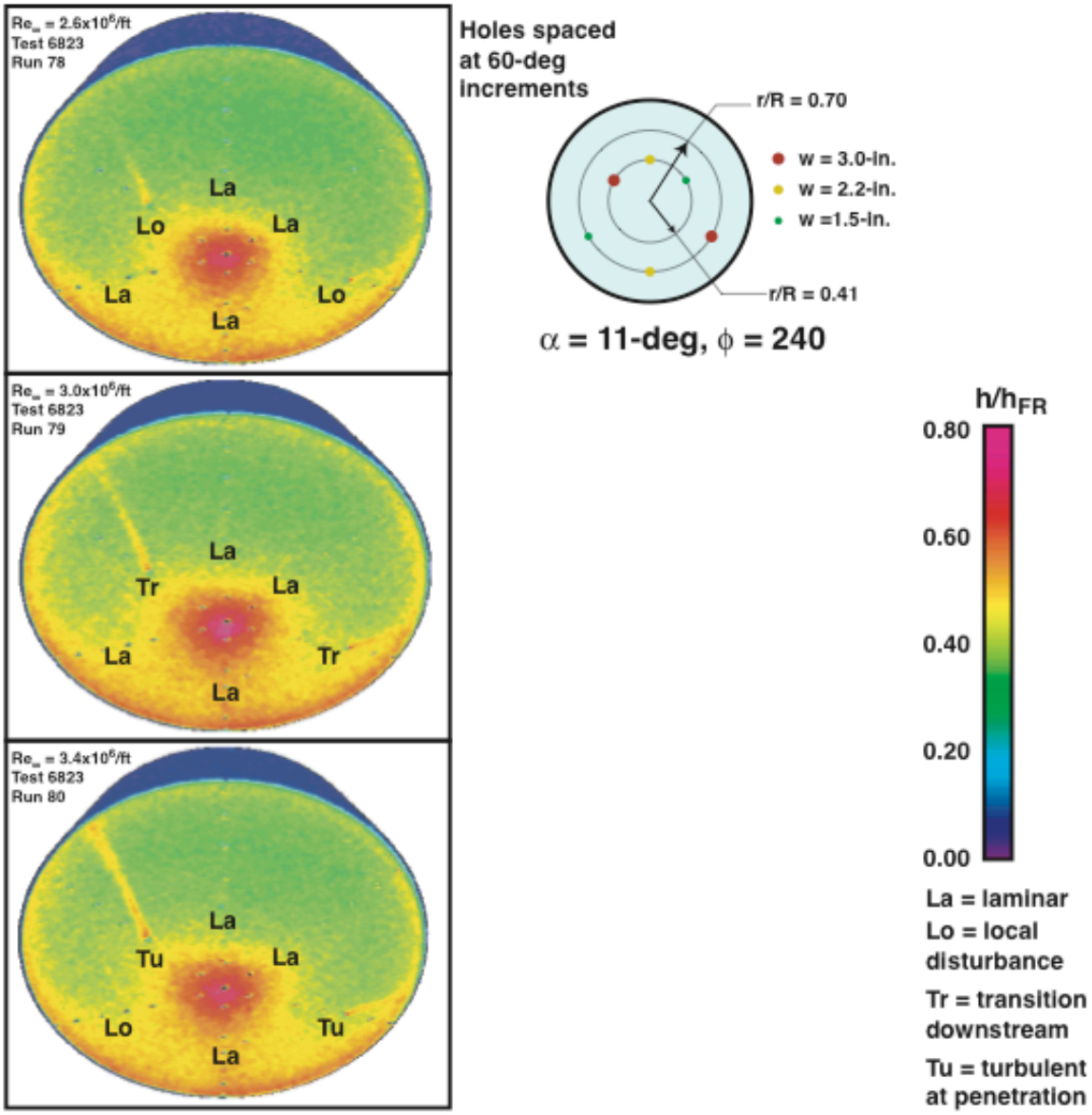

Figure 28. Cavity Effects on Heating, Baseline B-5-PA-2 Model, α = 11-deg, ϕ = 240-deg

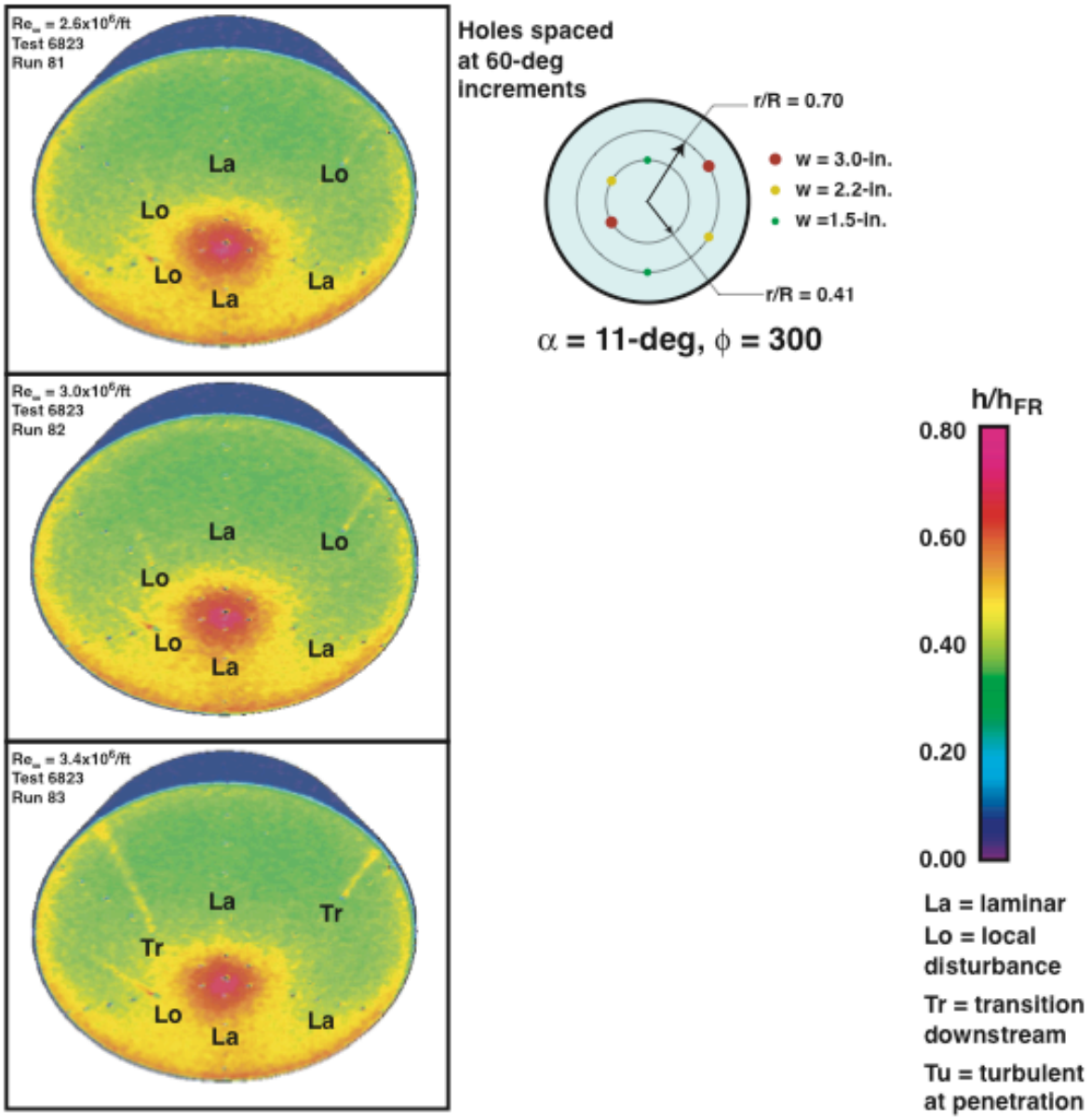

Figure 29. Cavity Effects on Heating, Baseline B-5-PA-2 Model, α = 11-deg, ϕ = 300-deg

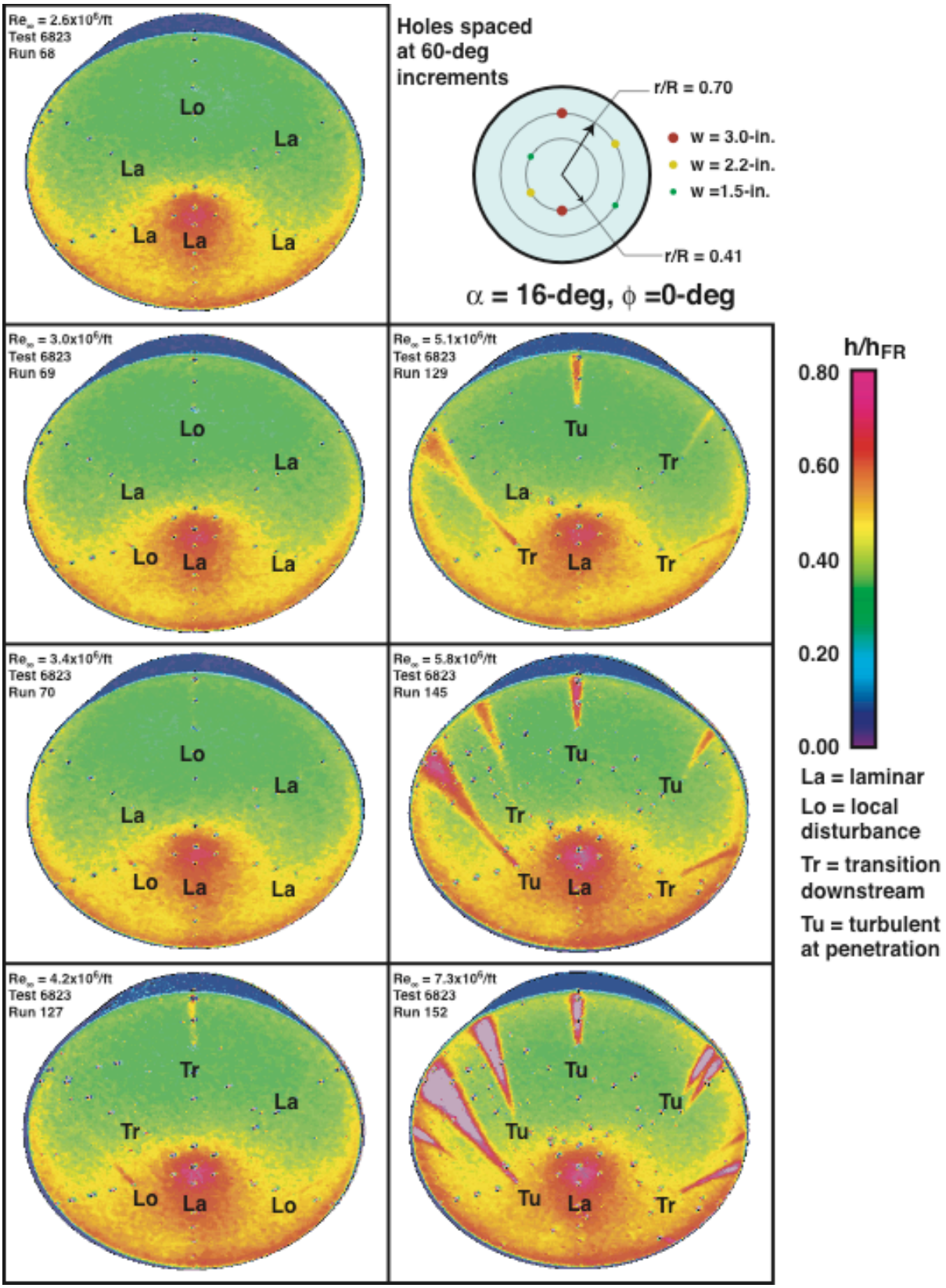

Figure 30. Cavity Effects on Heating, Baseline B-5-PA-2 Model, α = 16-deg, ϕ = 0-deg

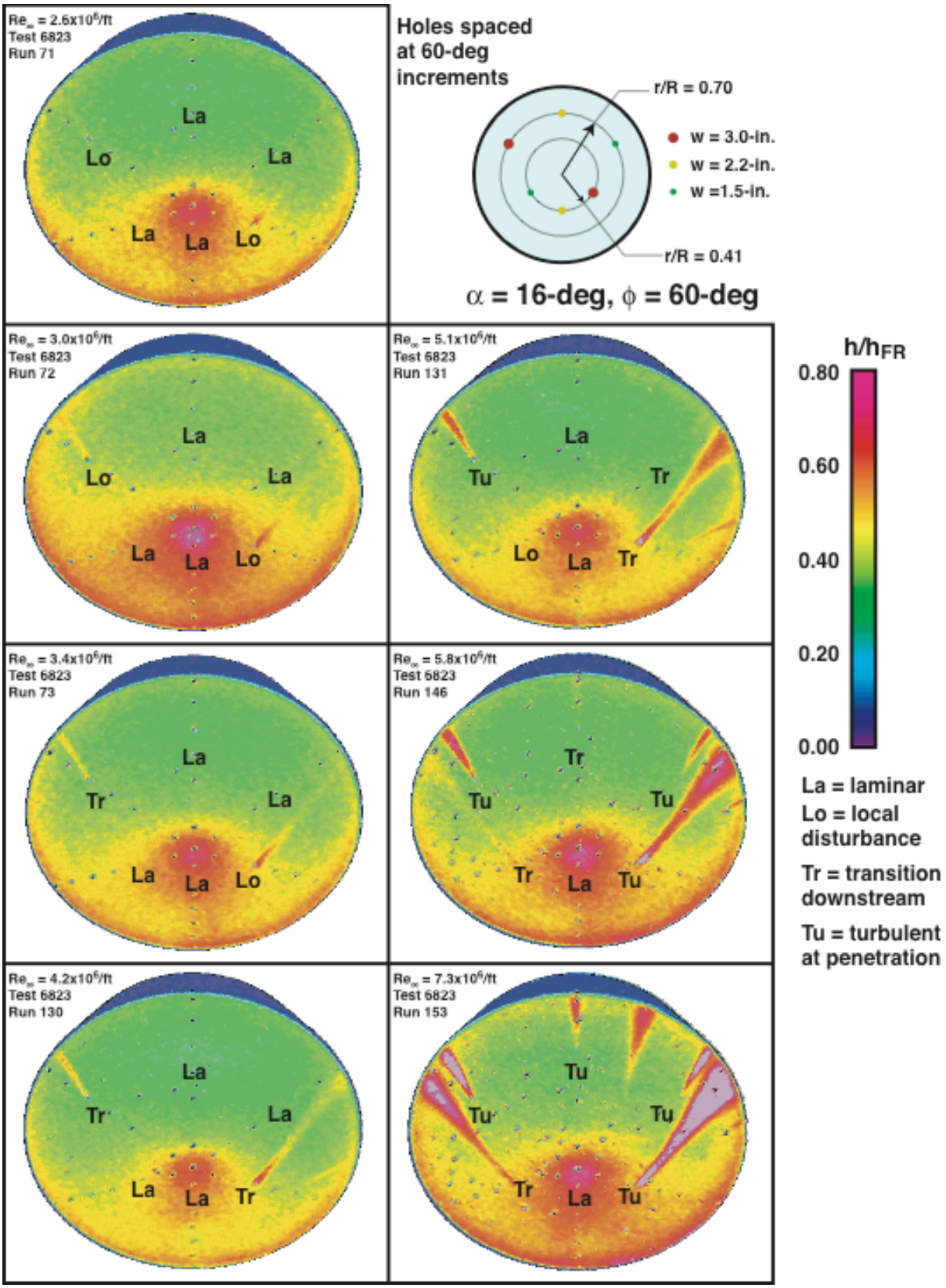

Figure 31. Cavity Effects on Heating, Baseline B-5-PA-2 Model, α = 16-deg, ϕ = 60-deg

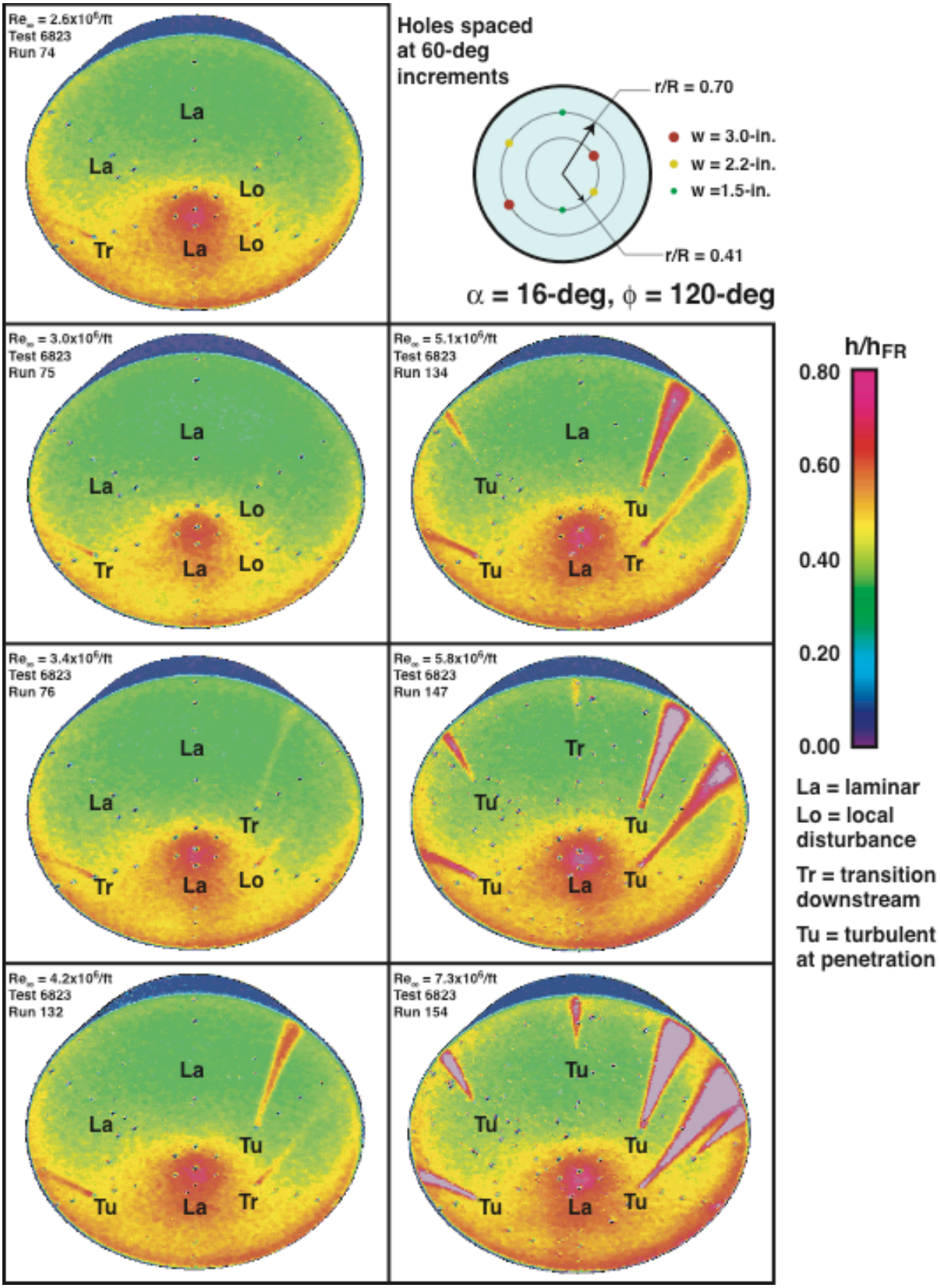

Figure 32. Cavity Effects on Heating, Baseline B-5-PA-2 Model, α = 16-deg, ϕ = 120-deg

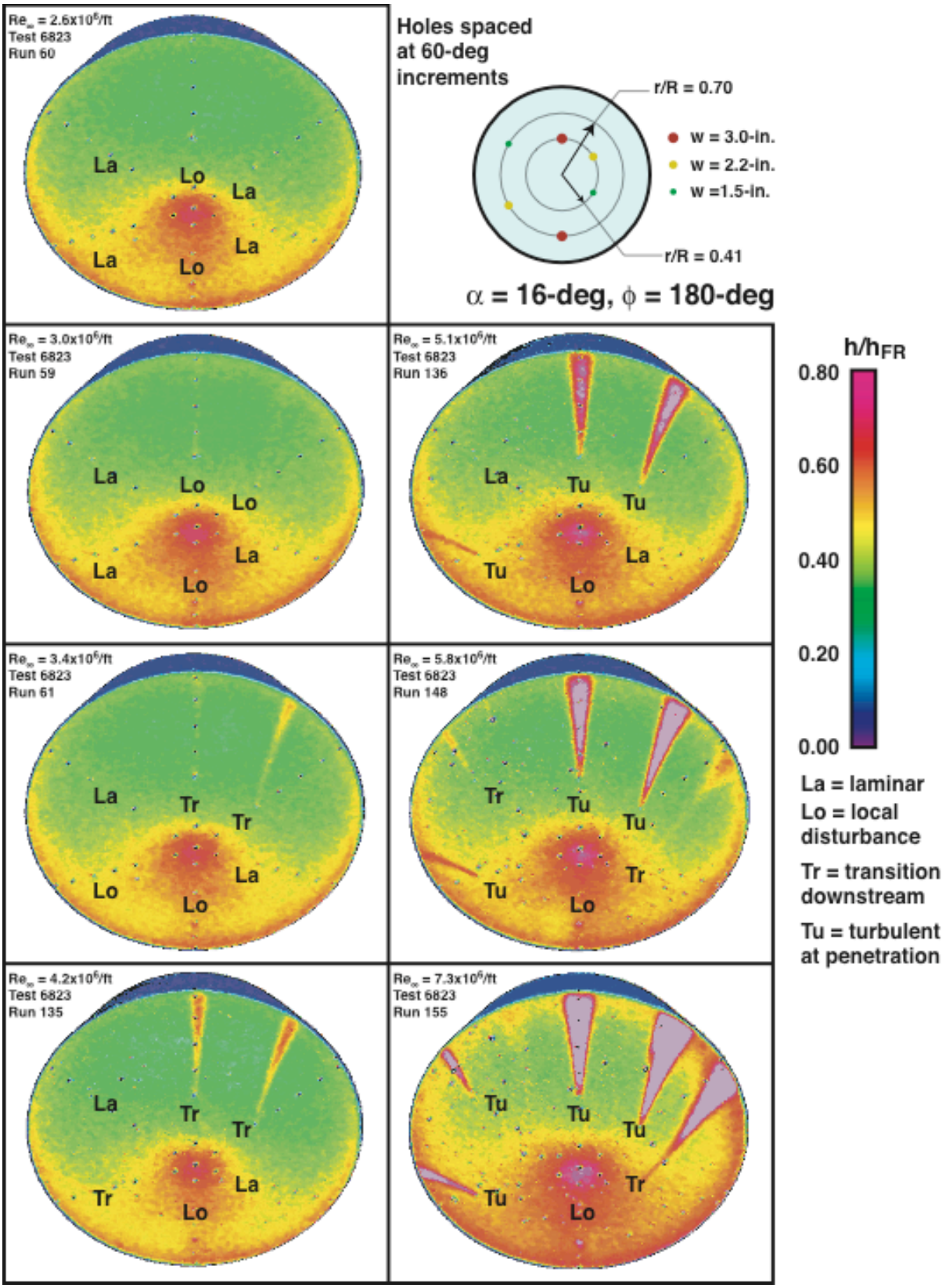

Figure 33. Cavity Effects on Heating, Baseline B-5-PA-2 Model, α = 16-deg, ϕ = 180-deg

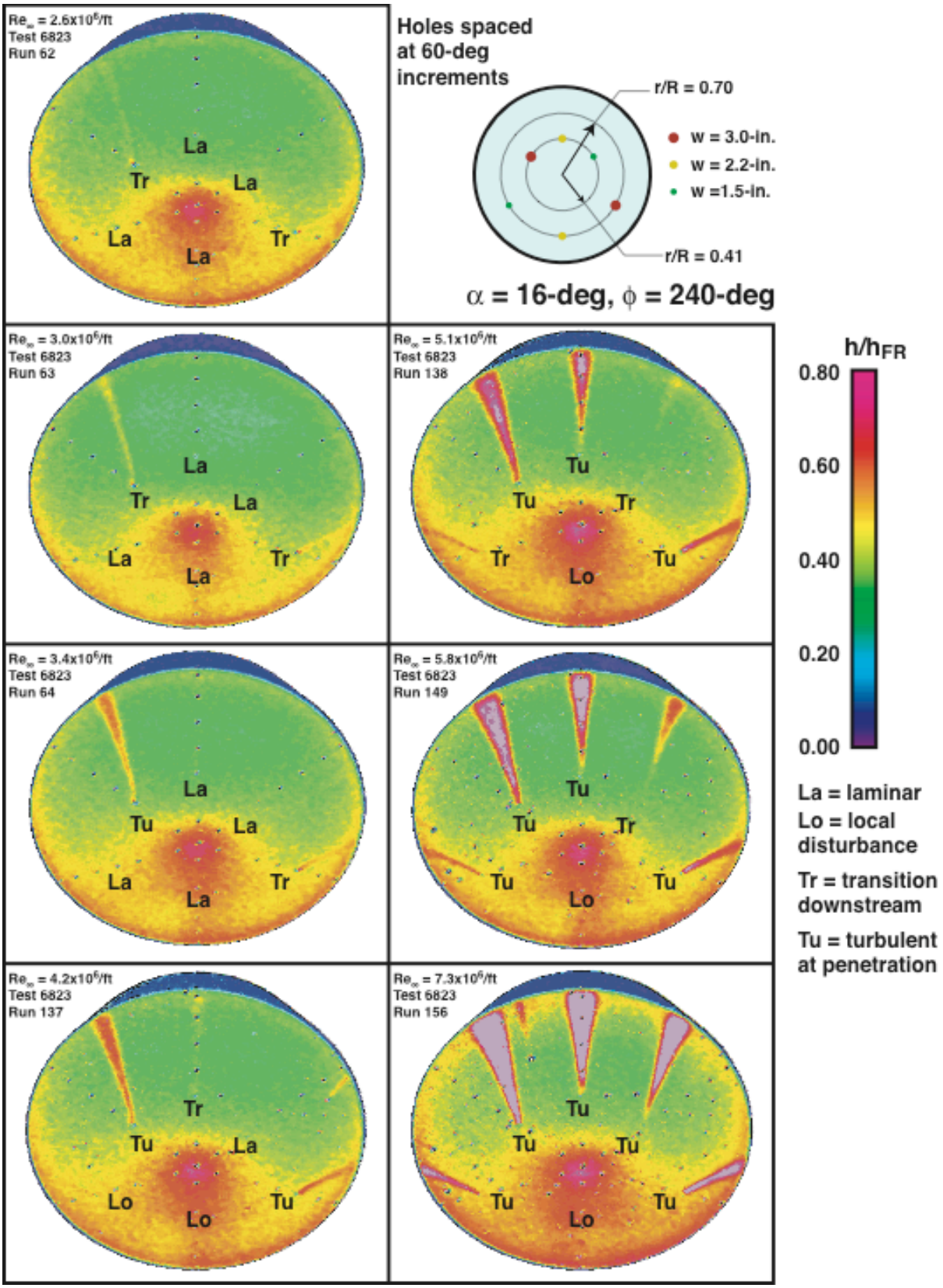

Figure 34. Cavity Effects on Heating, Baseline B-5-PA-2 Model, α = 16-deg, ϕ = 240-deg

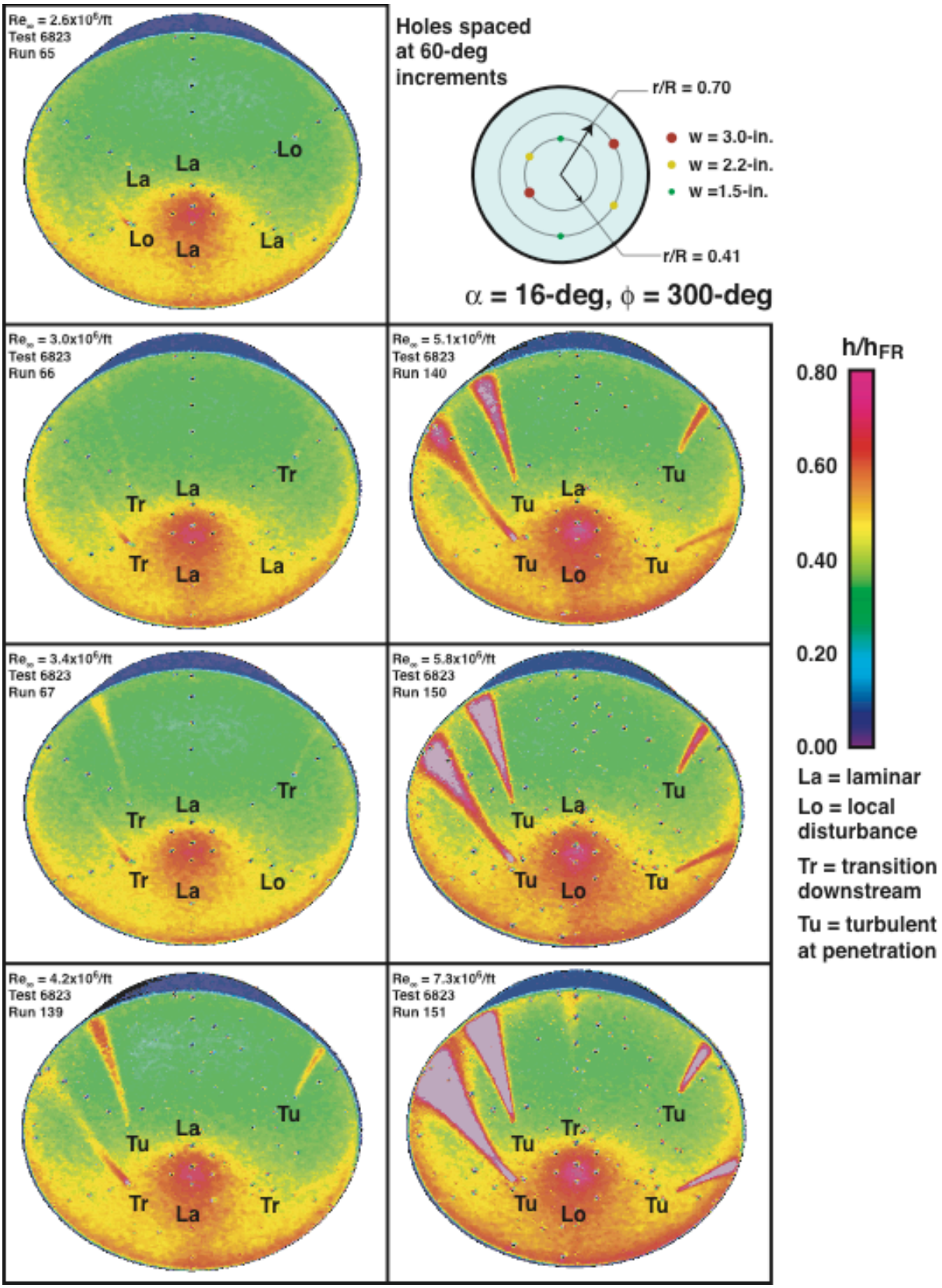

Figure 35. Cavity Effects on Heating, Baseline B-5-PA-2 Model, α = 16-deg, ϕ = 300-deg

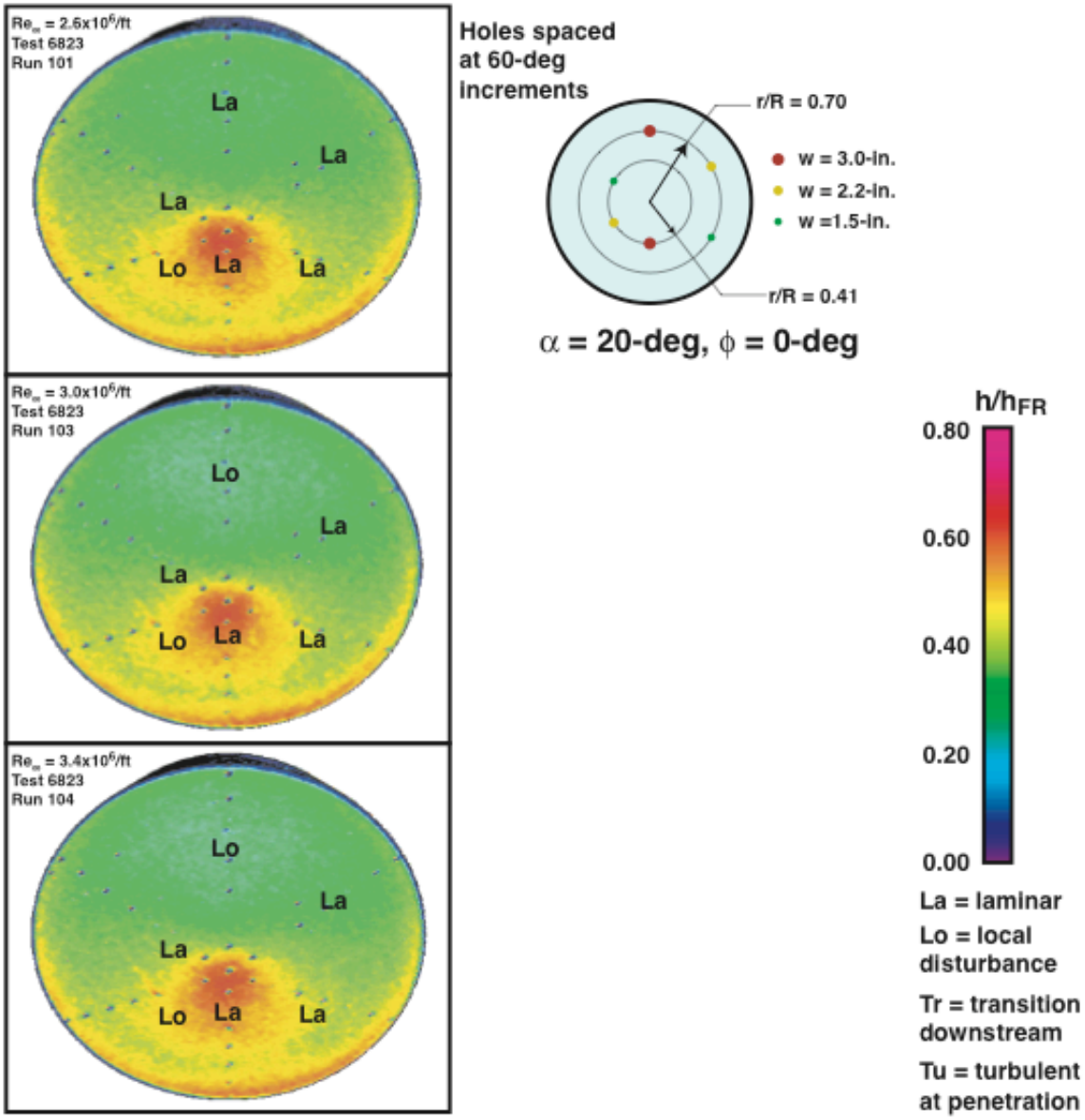

Figure 36. Cavity Effects on Heating, Baseline B-5-PA-2 Model, α = 20-deg, ϕ = 0-deg

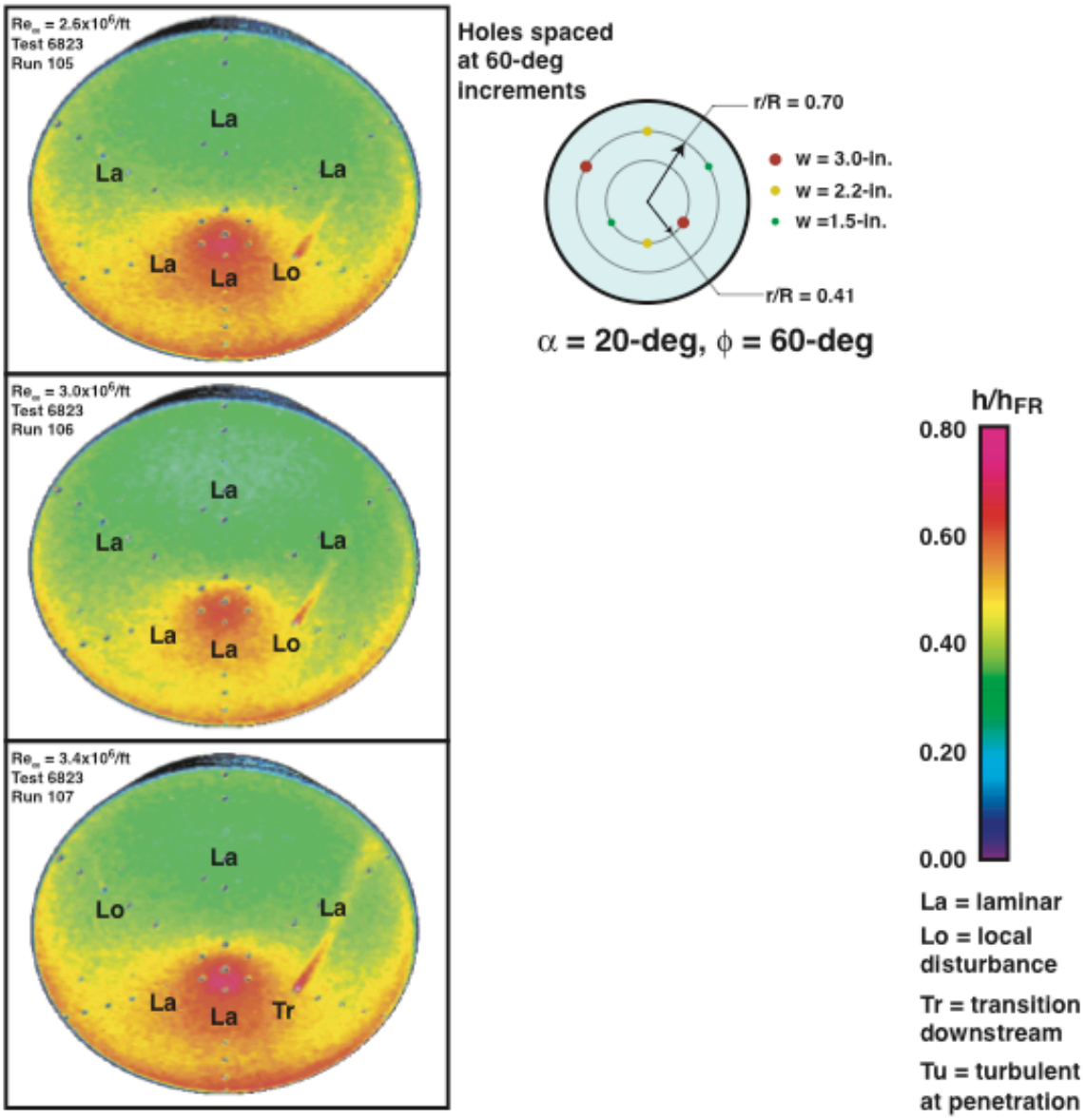

Figure 37. Cavity Effects on Heating, Baseline B-5-PA-2 Model, α = 20-deg, ϕ = 60-deg

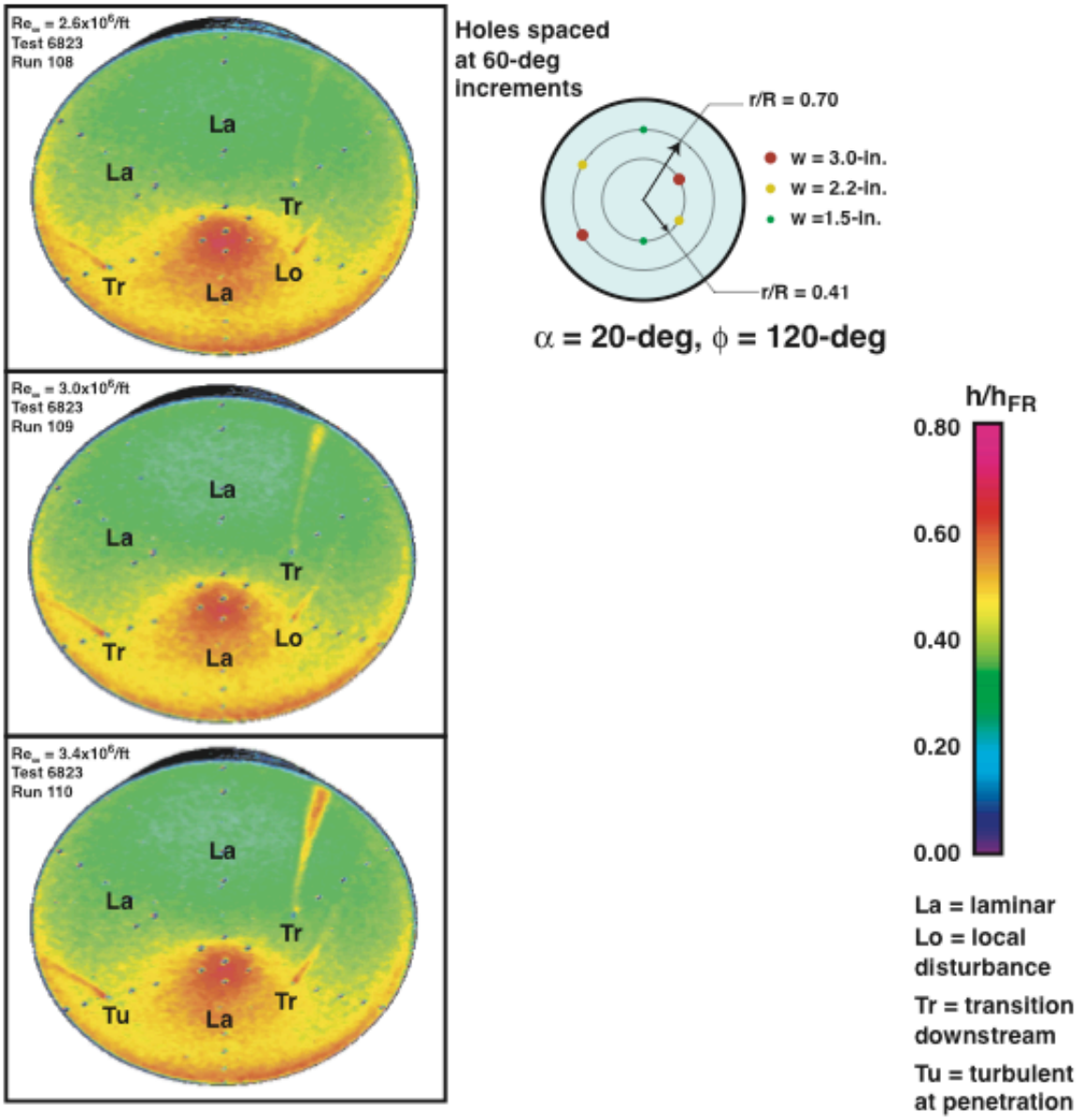

Figure 38. Cavity Effects on Heating, Baseline B-5-PA-2 Model, α = 20-deg, ϕ = 120-deg

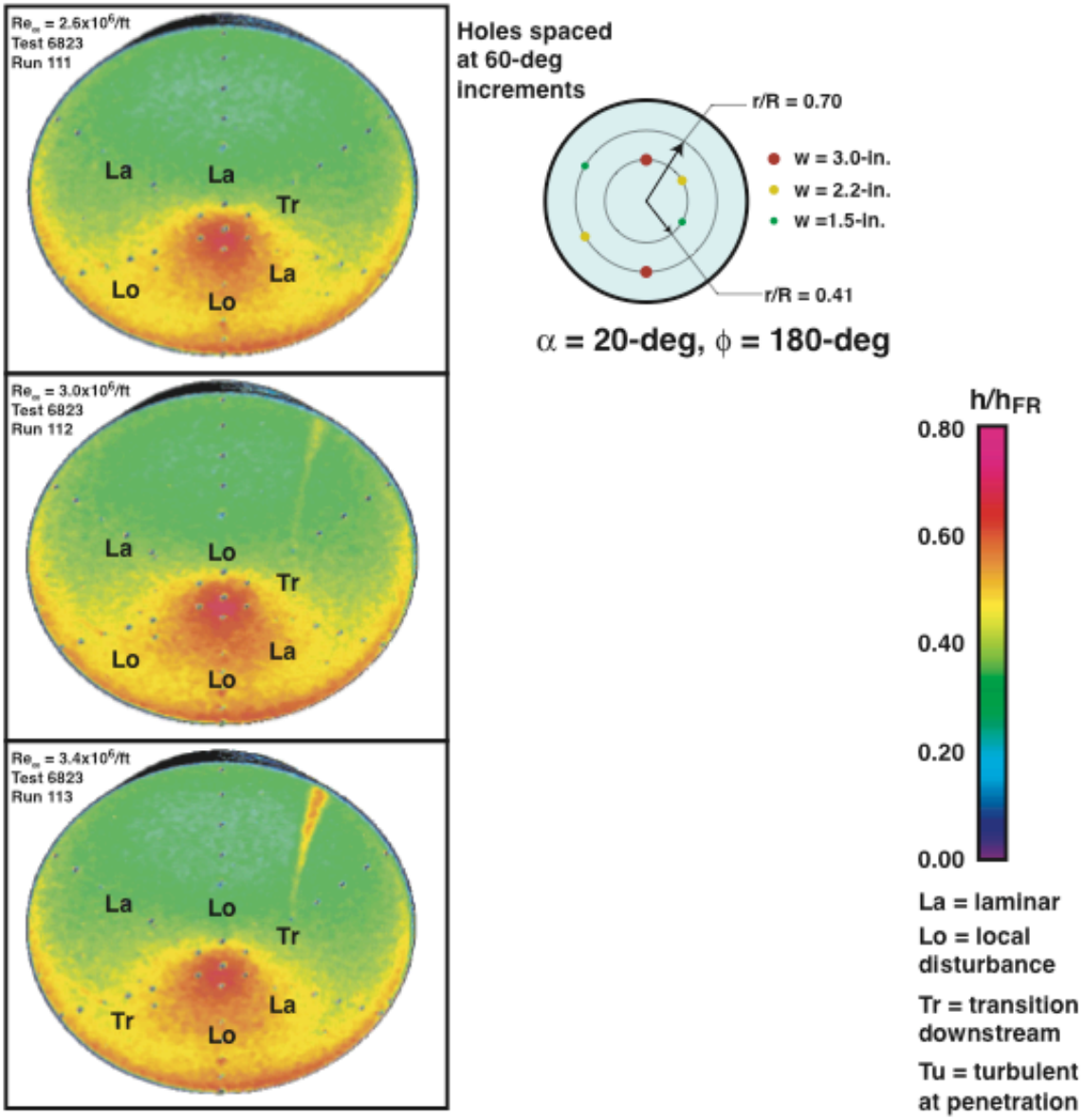

Figure 39. Cavity Effects on Heating, Baseline B-5-PA-2 Model, α = 20-deg, ϕ = 180-deg

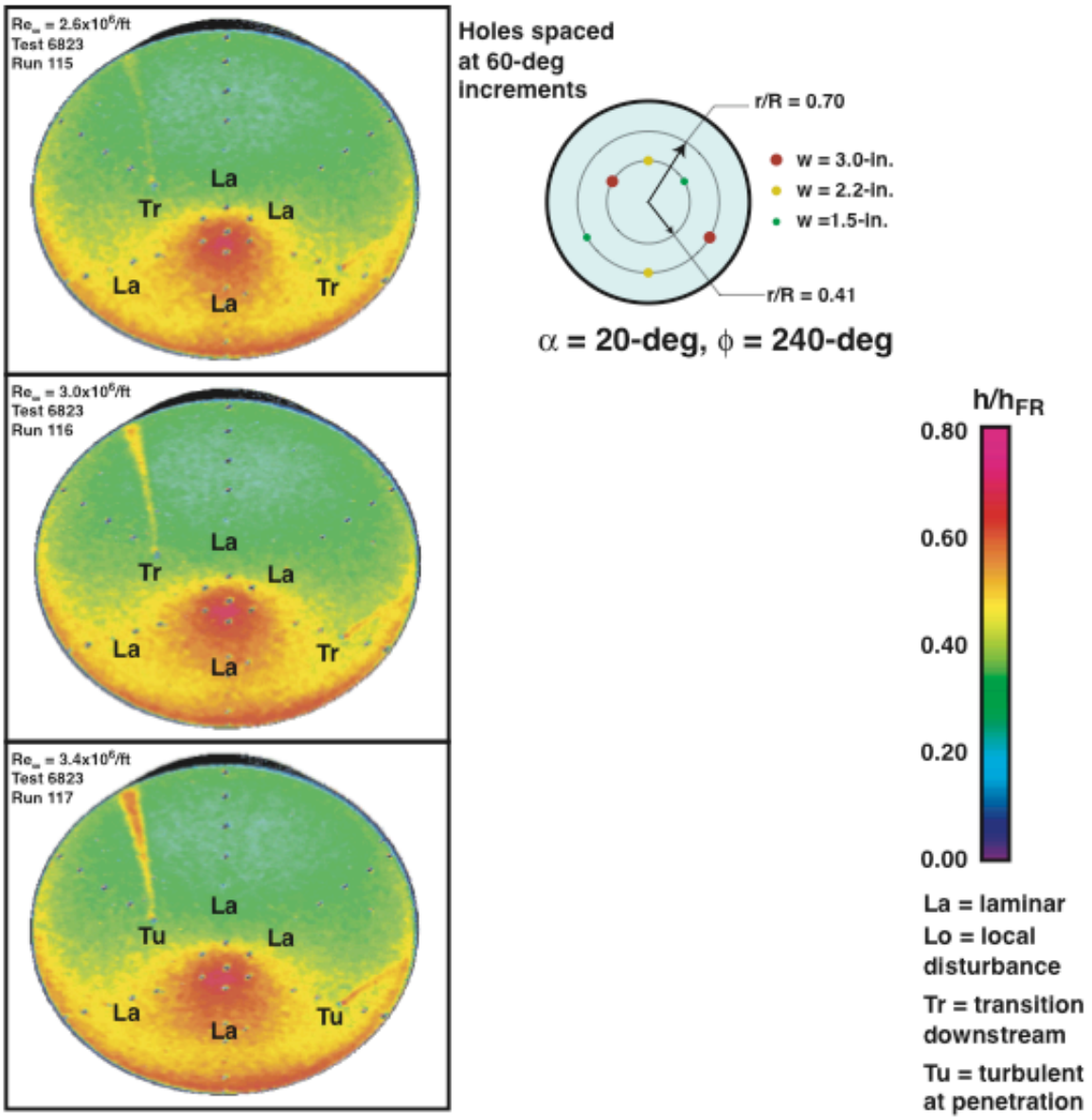

Figure 40. Cavity Effects on Heating, Baseline B-5-PA-2 Model, α = 20-deg, ϕ = 240-deg

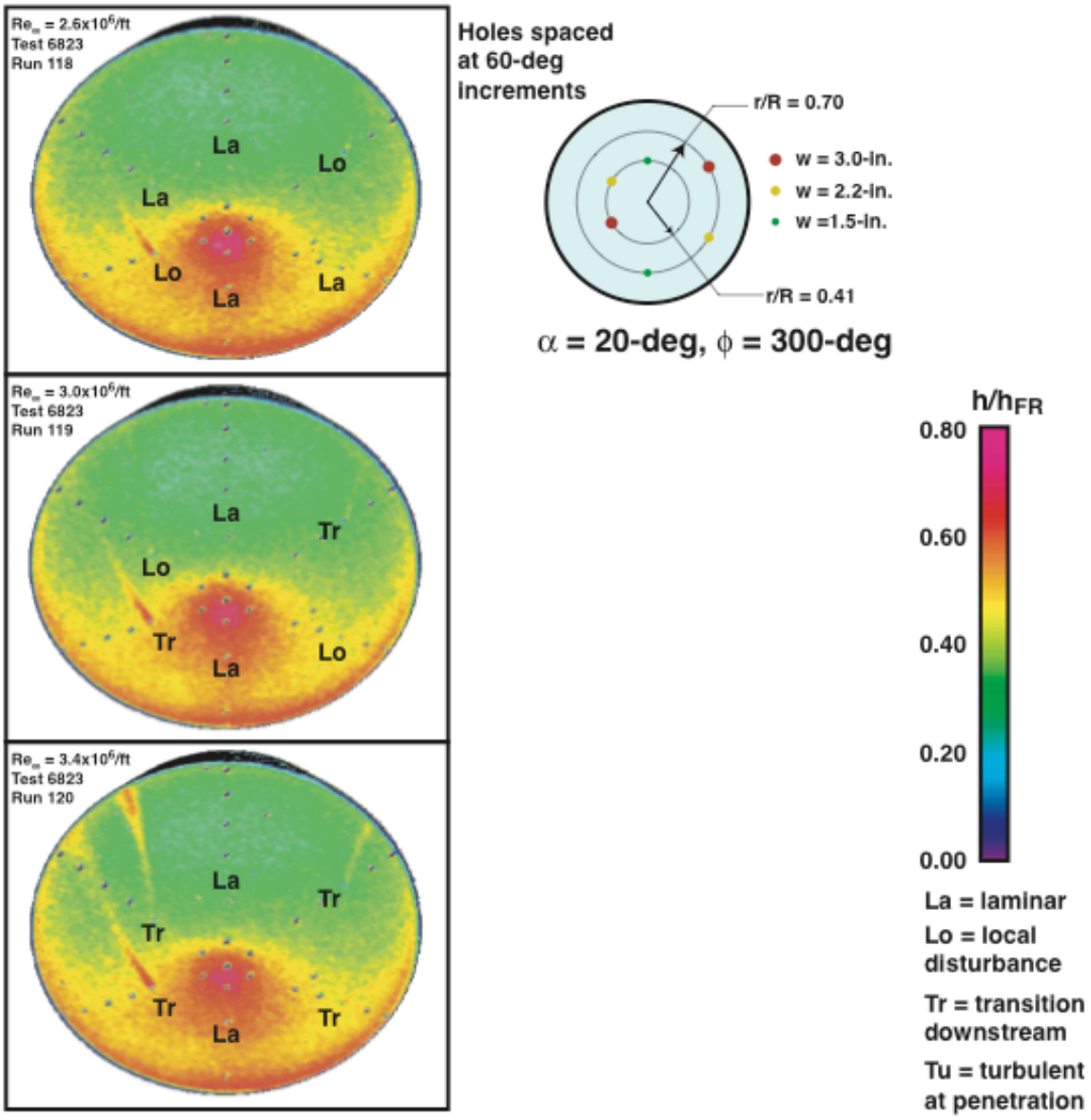

Figure 41. Cavity Effects on Heating, Baseline B-5-PA-2 Model, α = 20-deg, ϕ = 300-deg

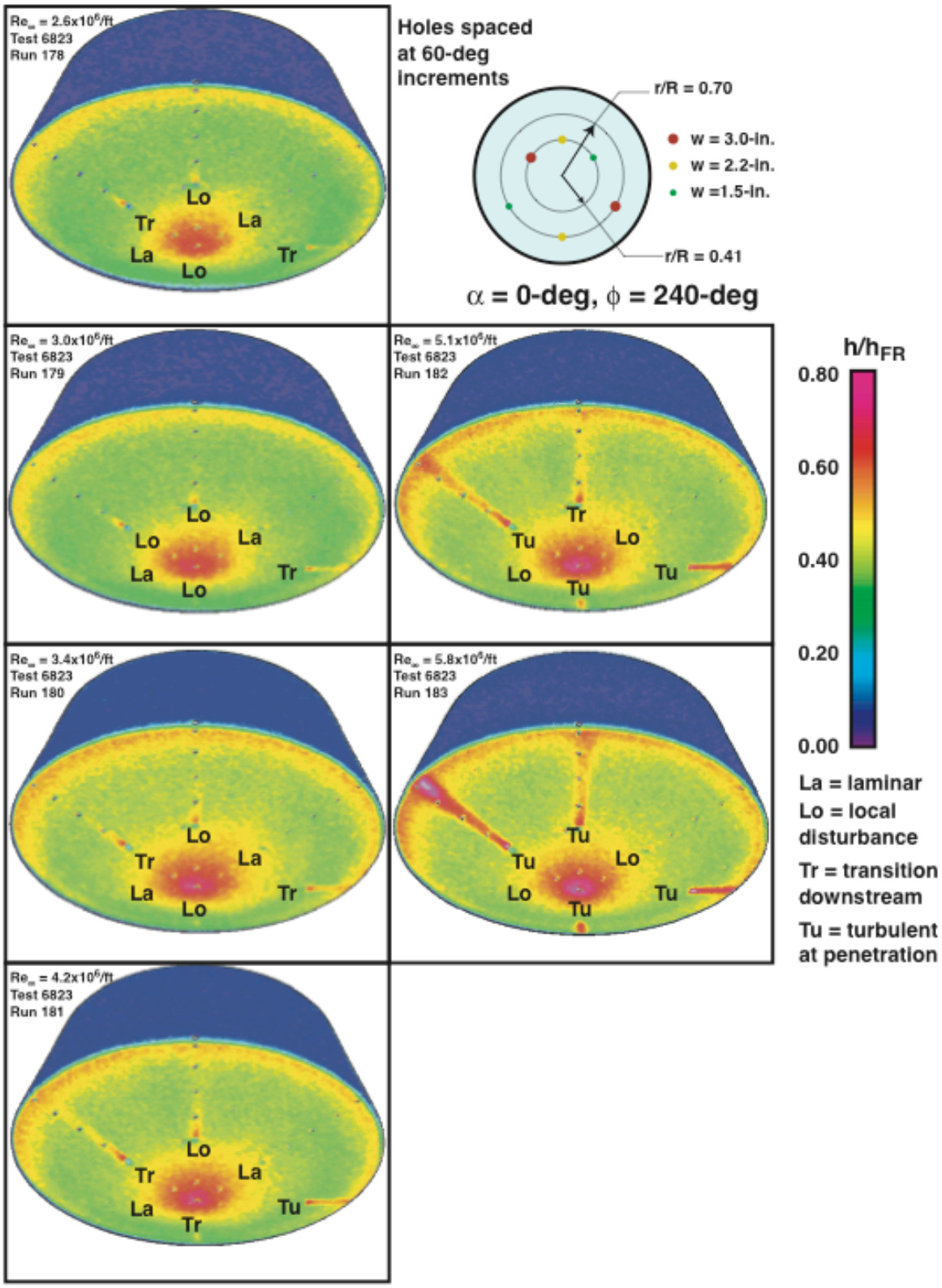

Figure 42. Cavity Effects on Heating, Baseline B-5-PA-3 Model, α = 0-deg, ϕ = 240-deg

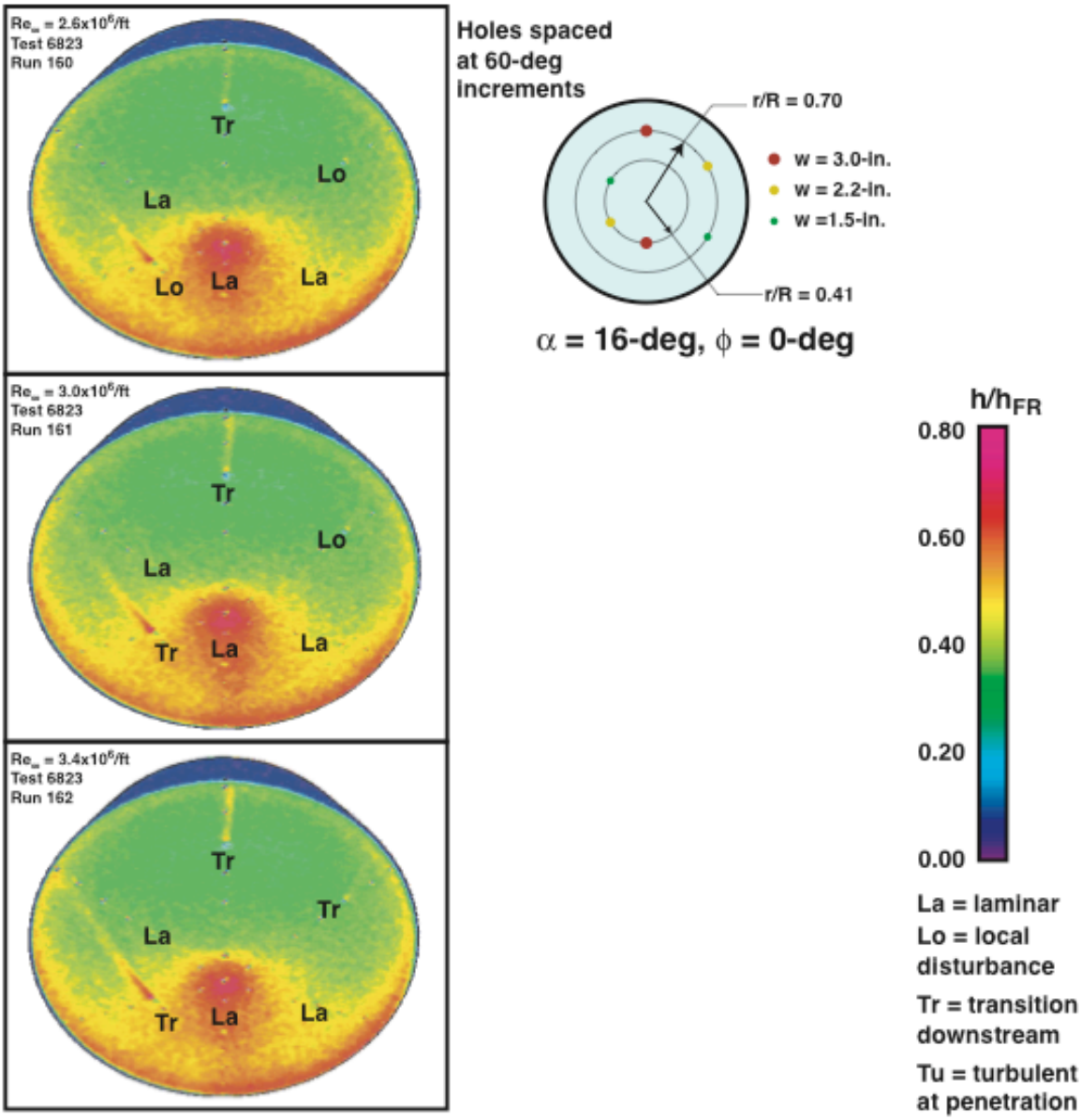

Figure 43. Cavity Effects on Heating, Baseline B-5-PA-3 Model, α = 16-deg, ϕ = 0-deg

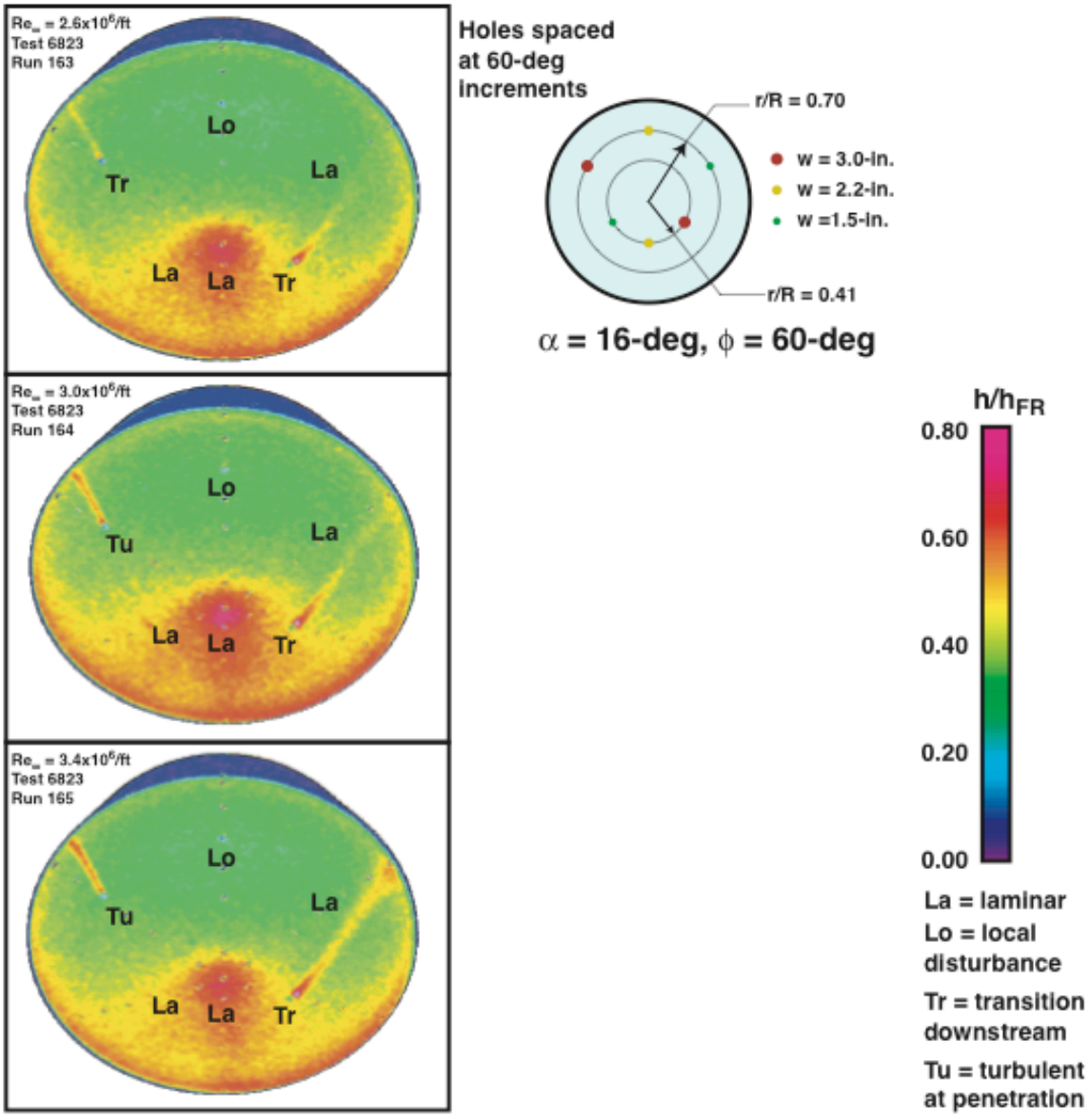

Figure 44. Cavity Effects on Heating, Baseline B-5-PA-3 Model, α = 16-deg, ϕ = 60-deg

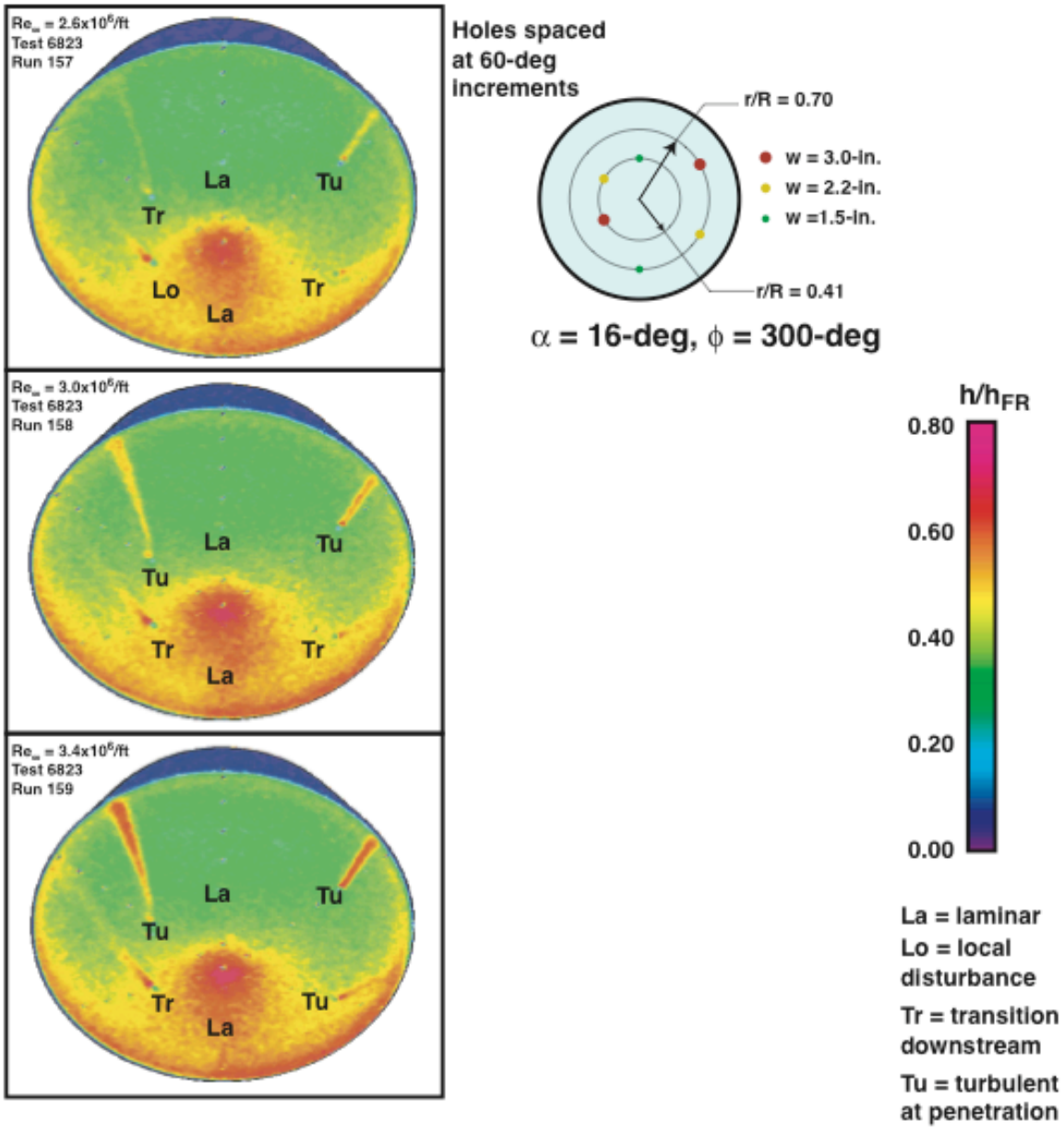

Figure 45. Cavity Effects on Heating, Baseline B-5-PA-3 Model, α = 16-deg, ϕ = 300-deg

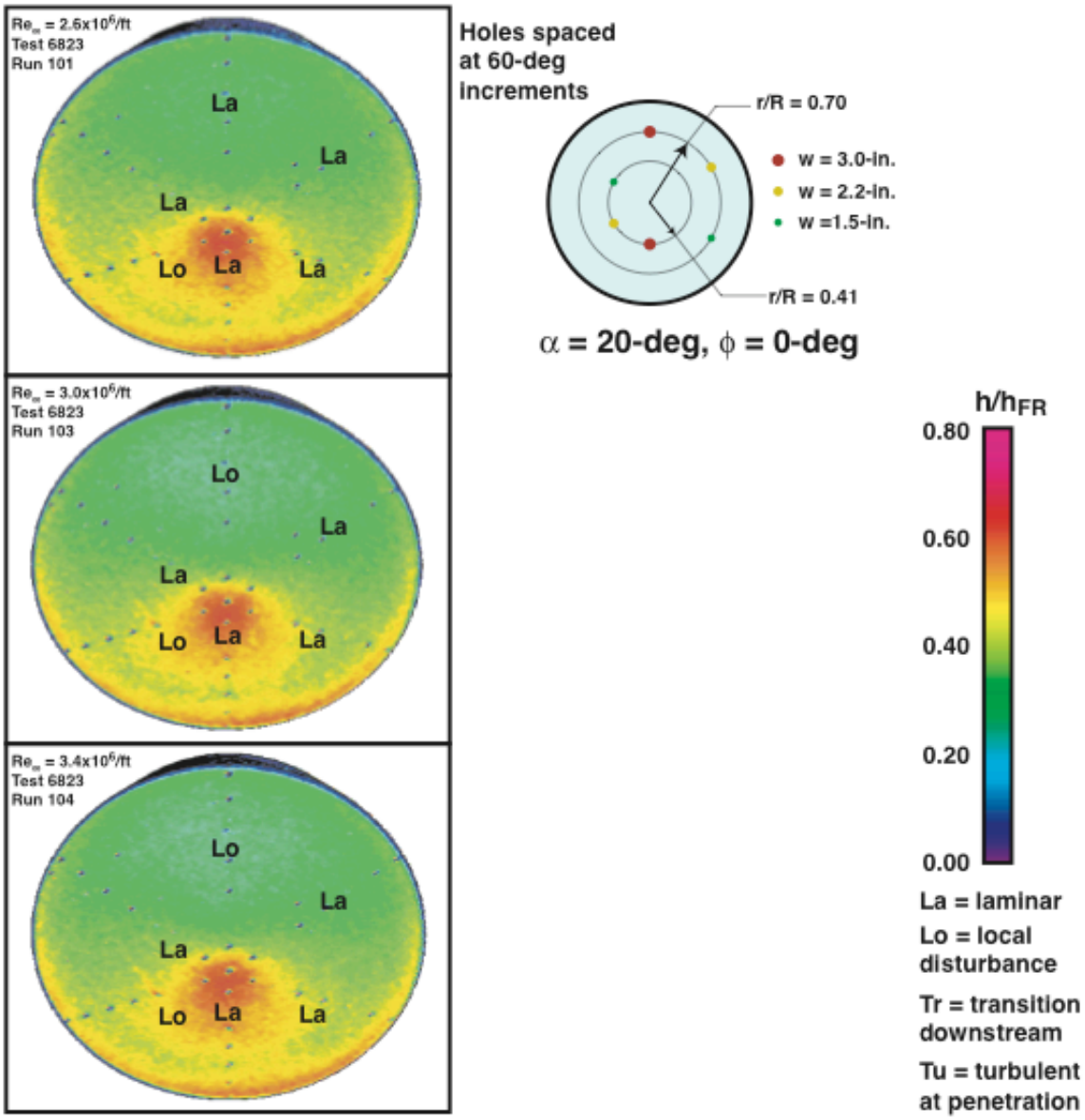

Figure 46. Cavity Effects on Heating, Baseline B-5-PA-3 Model, α = 20-deg, ϕ = 0-deg

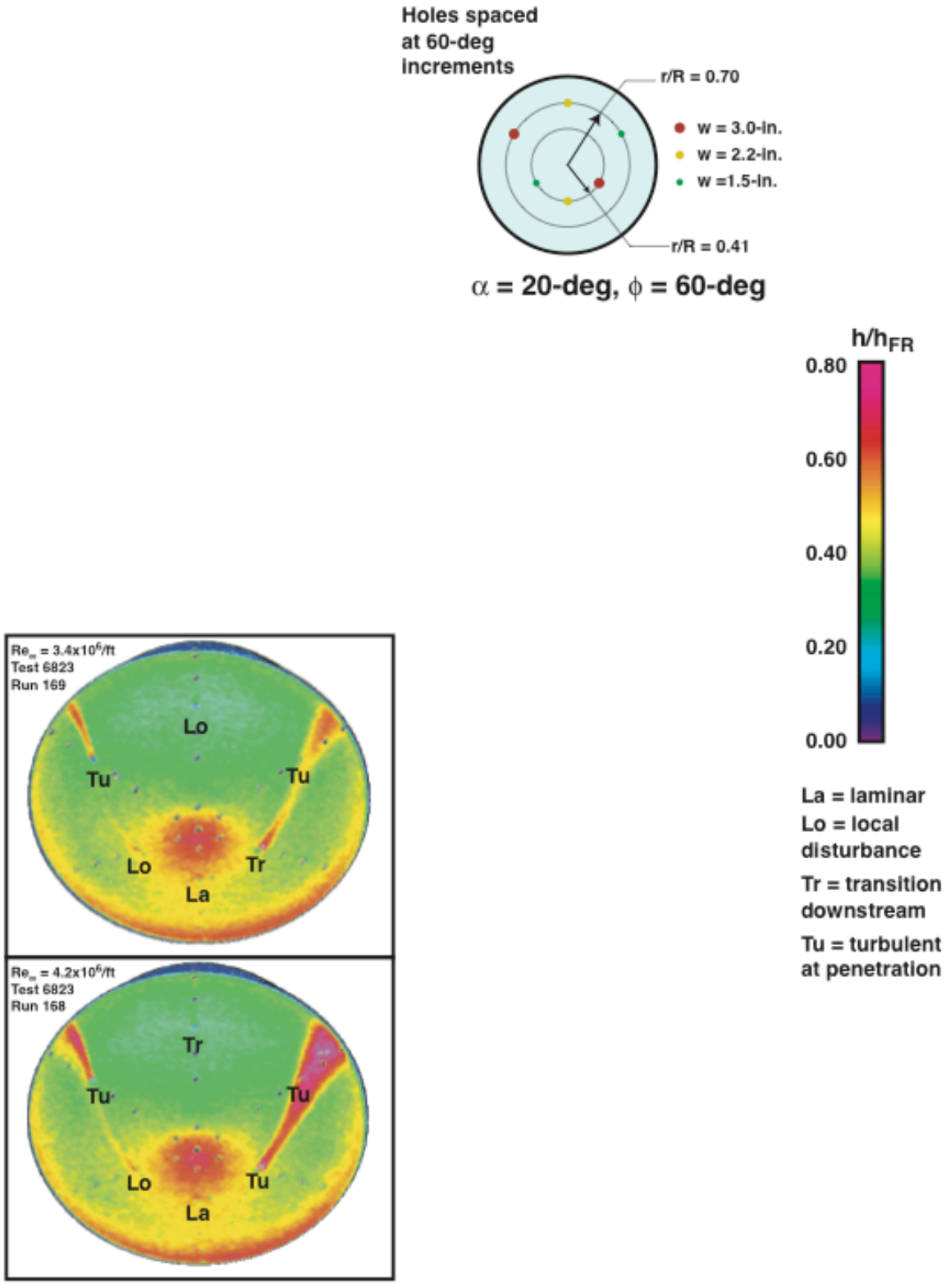

Figure 47. Cavity Effects on Heating, Baseline B-5-PA-3 Model, α = 20-deg, ϕ = 60-deg

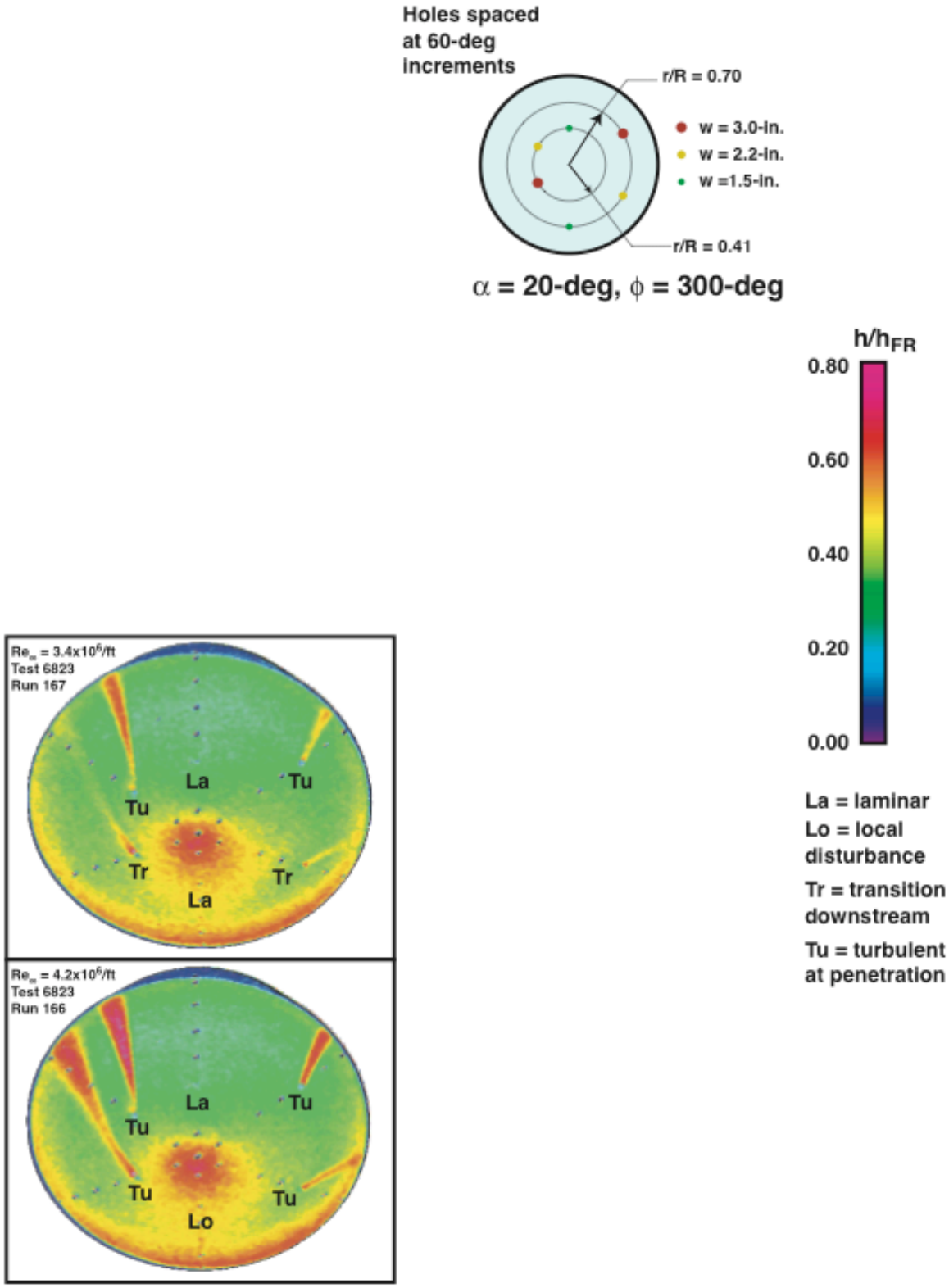

Figure 48. Cavity Effects on Heating, Baseline B-5-PA-3 Model, α = 20-deg, ϕ = 300-deg

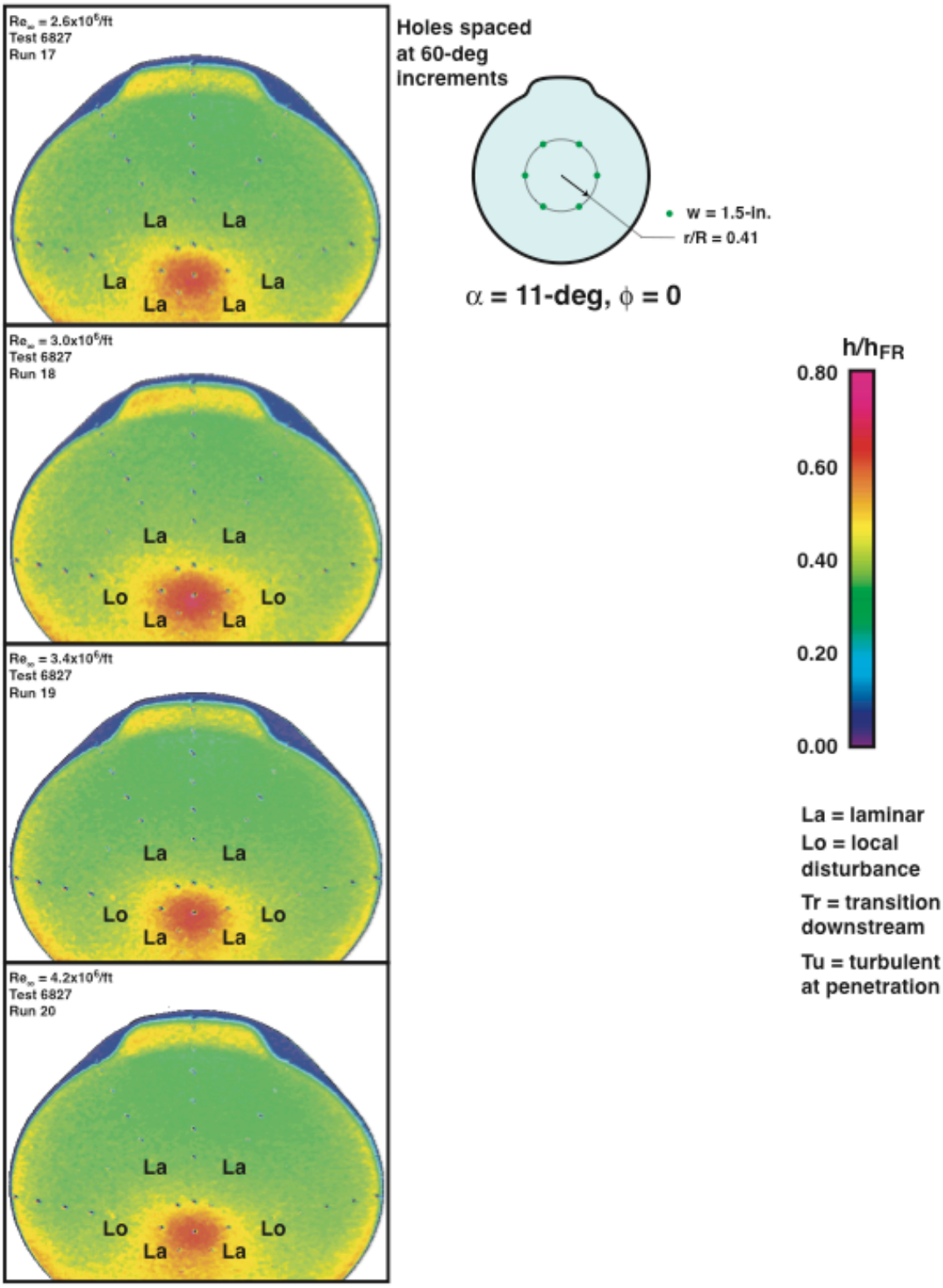

Figure 49. Cavity Effects on Heating, "Tab" T-5-1C-1 Model, α = 11-deg, ϕ = 0-deg

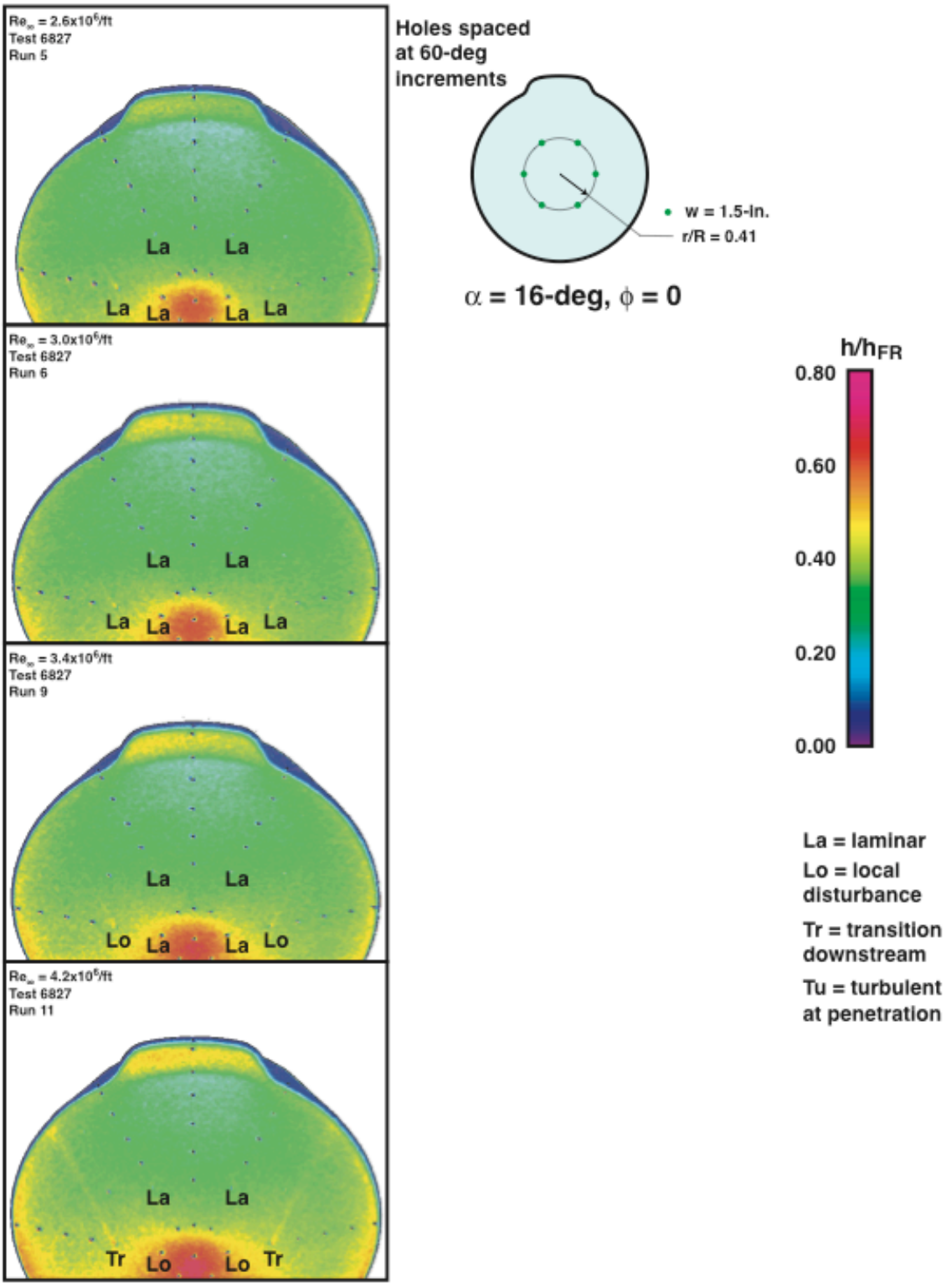

Figure 50. Cavity Effects on Heating, "Tab" T-5-1C-1 Model, α = 16-deg, ϕ = 0-deg

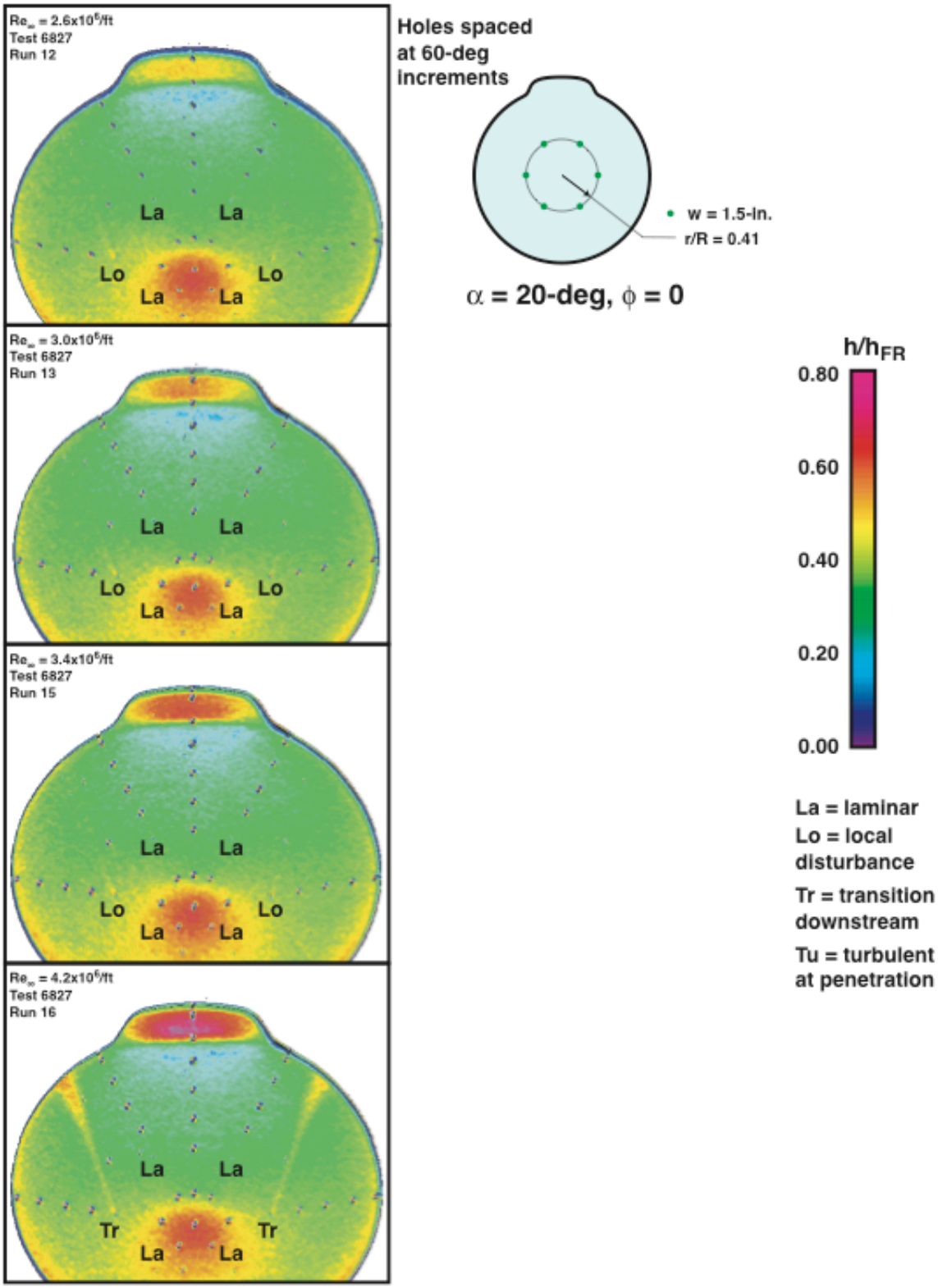

Figure 51. Cavity Effects on Heating, "Tab" T-5-1C-1 Model, α = 20-deg, ϕ = 0-deg

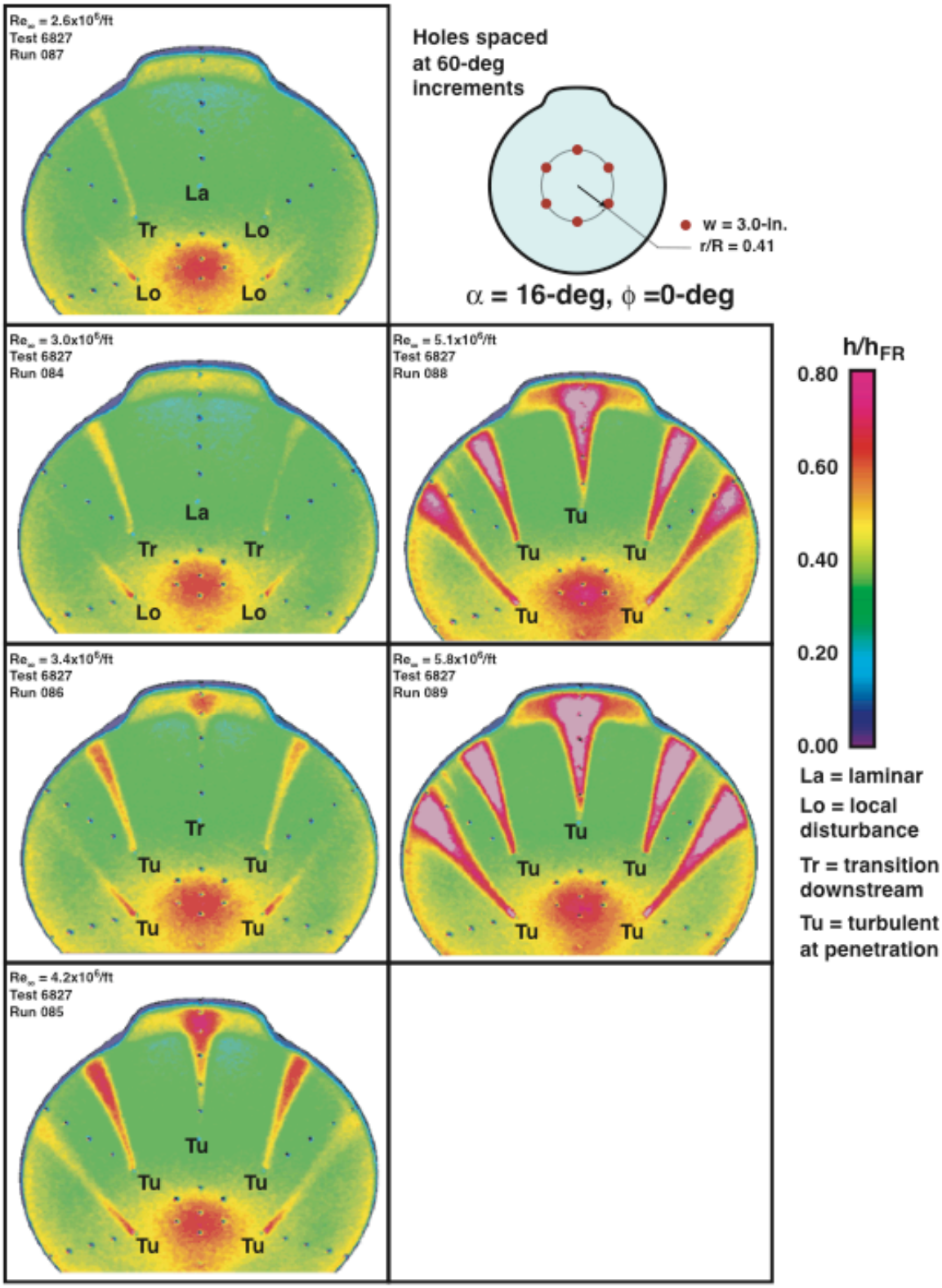

Figure 52. Cavity Effects on Heating, "Tab" T-5-3B-1 Model, α = 16-deg, ϕ = 0-deg

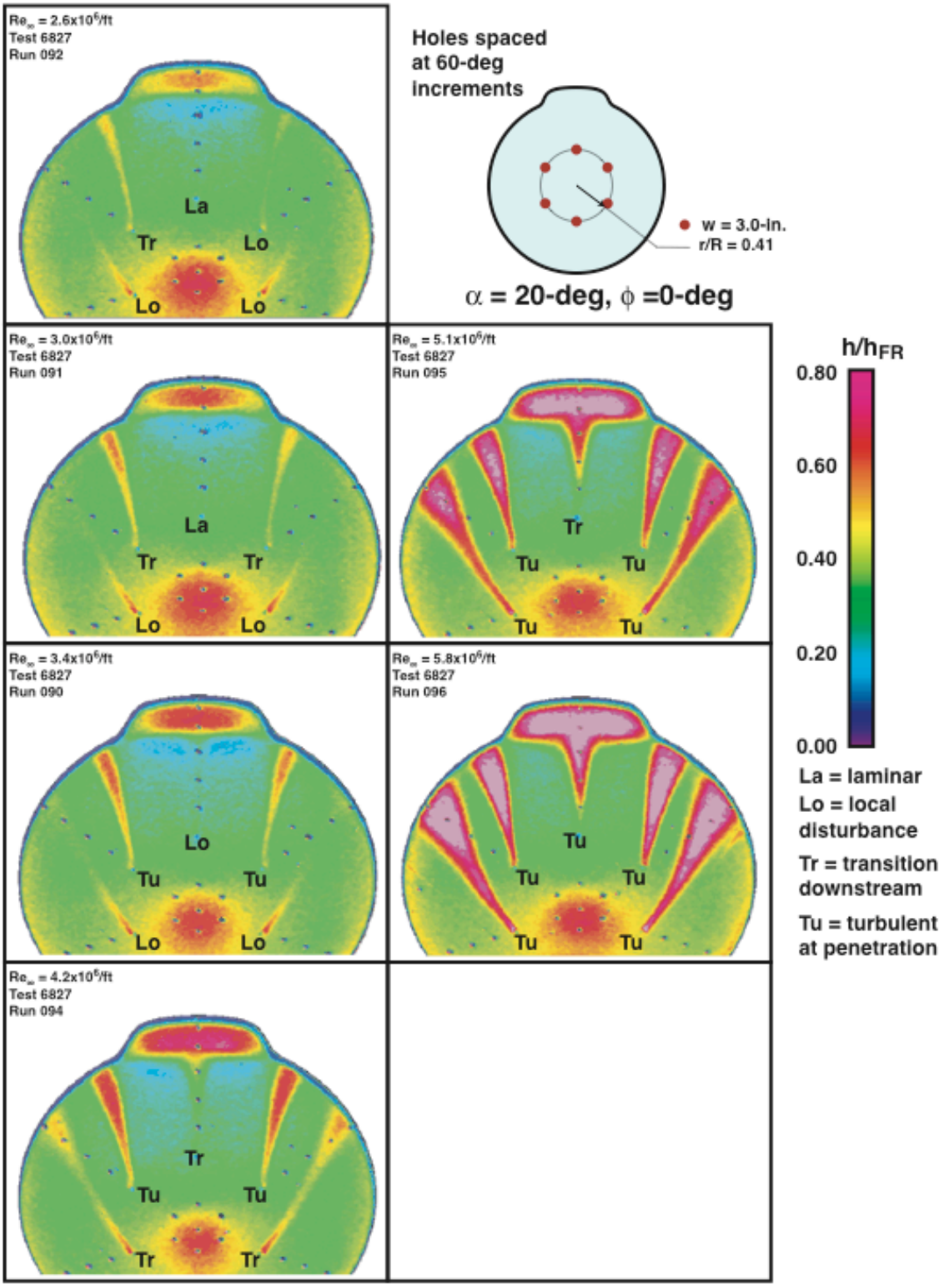

Figure 53. Cavity Effects on Heating, "Tab" T-5-3B-1 Model, α = 20-deg, ϕ = 0-deg

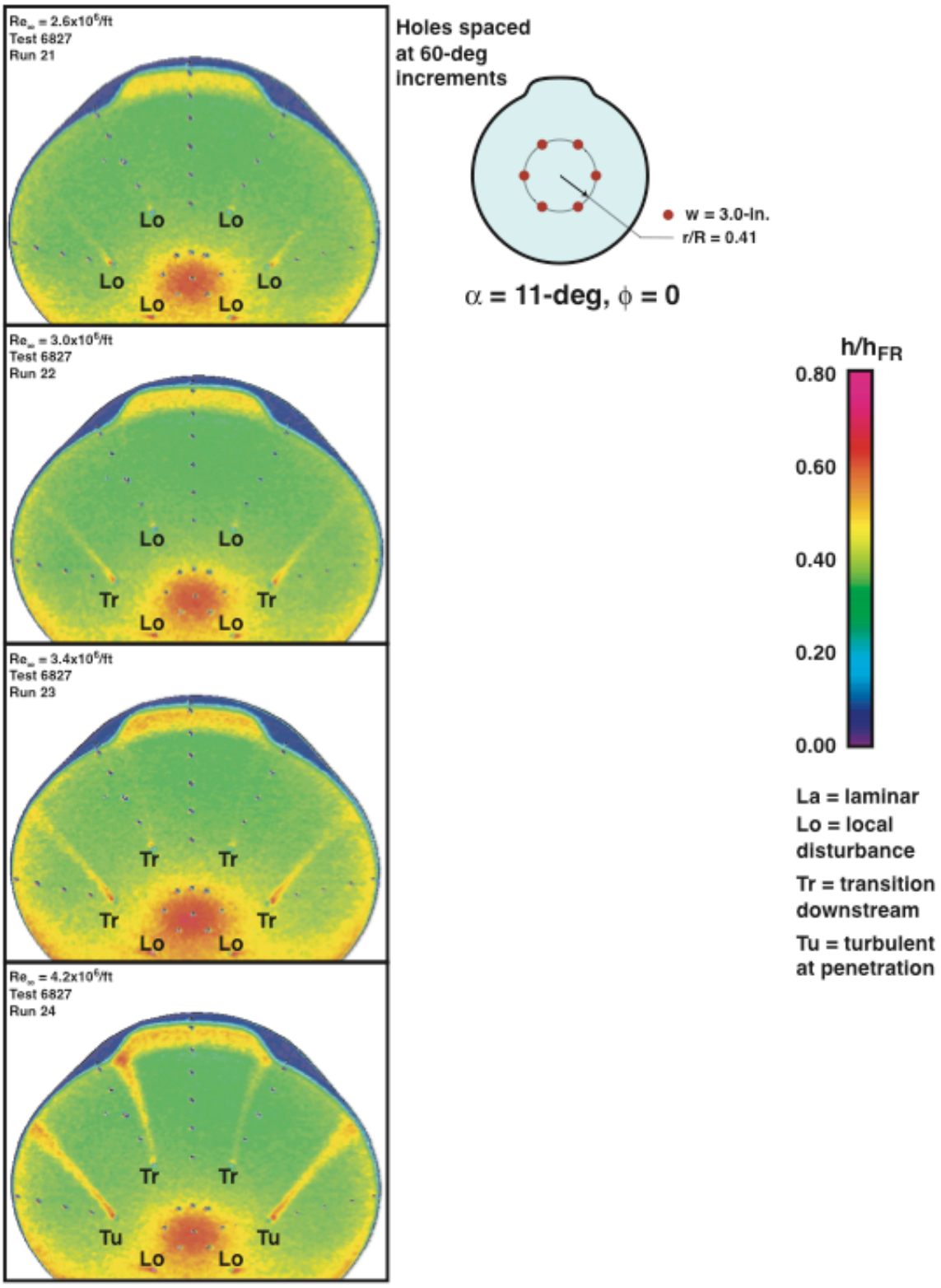

Figure 54. Cavity Effects on Heating, "Tab" T-5-3C-1 Model, α = 11-deg, ϕ = 0-deg

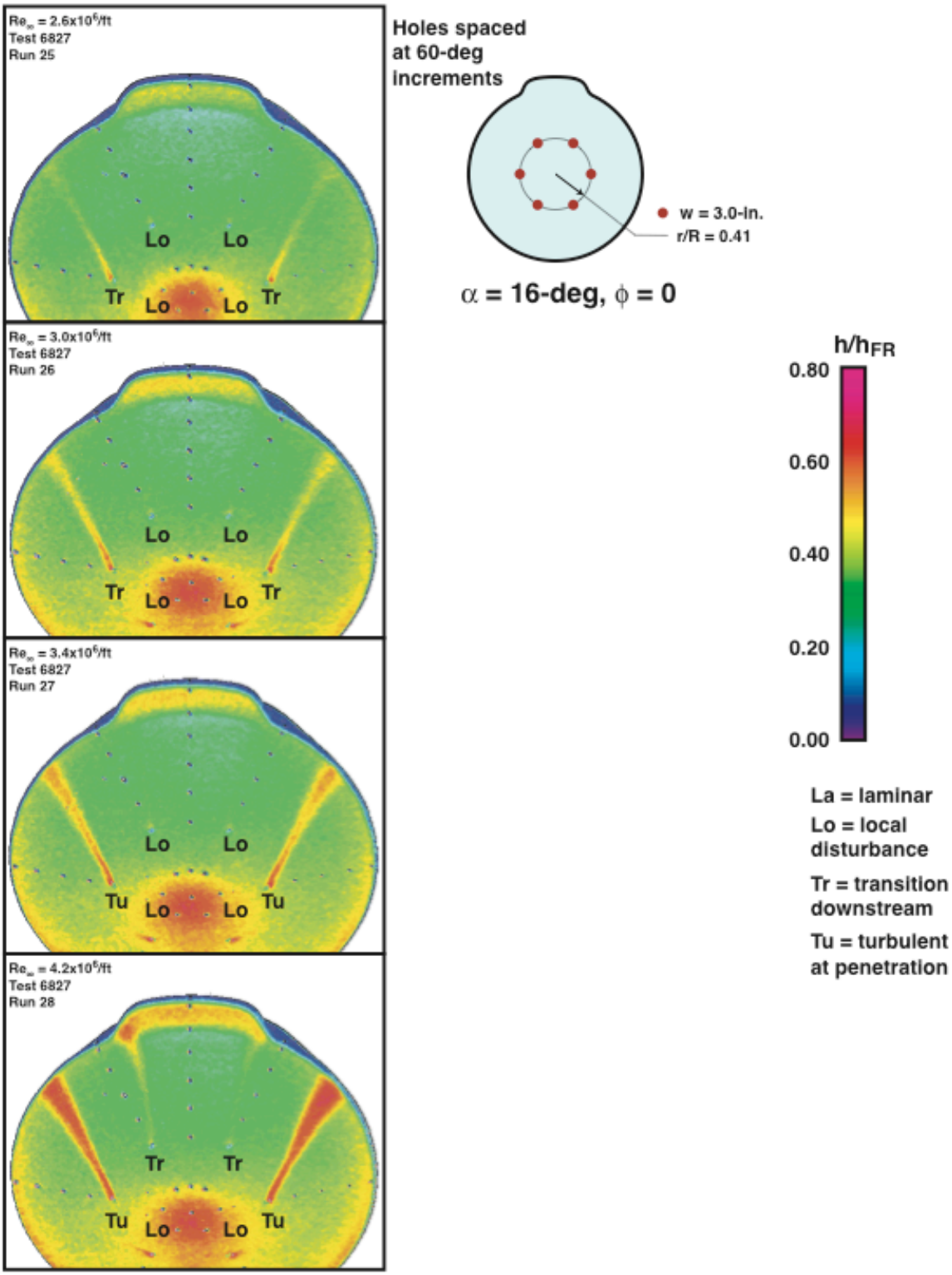

Figure 55. Cavity Effects on Heating, "Tab" T-5-3C-1 Model, α = 16-deg, ϕ = 0-deg

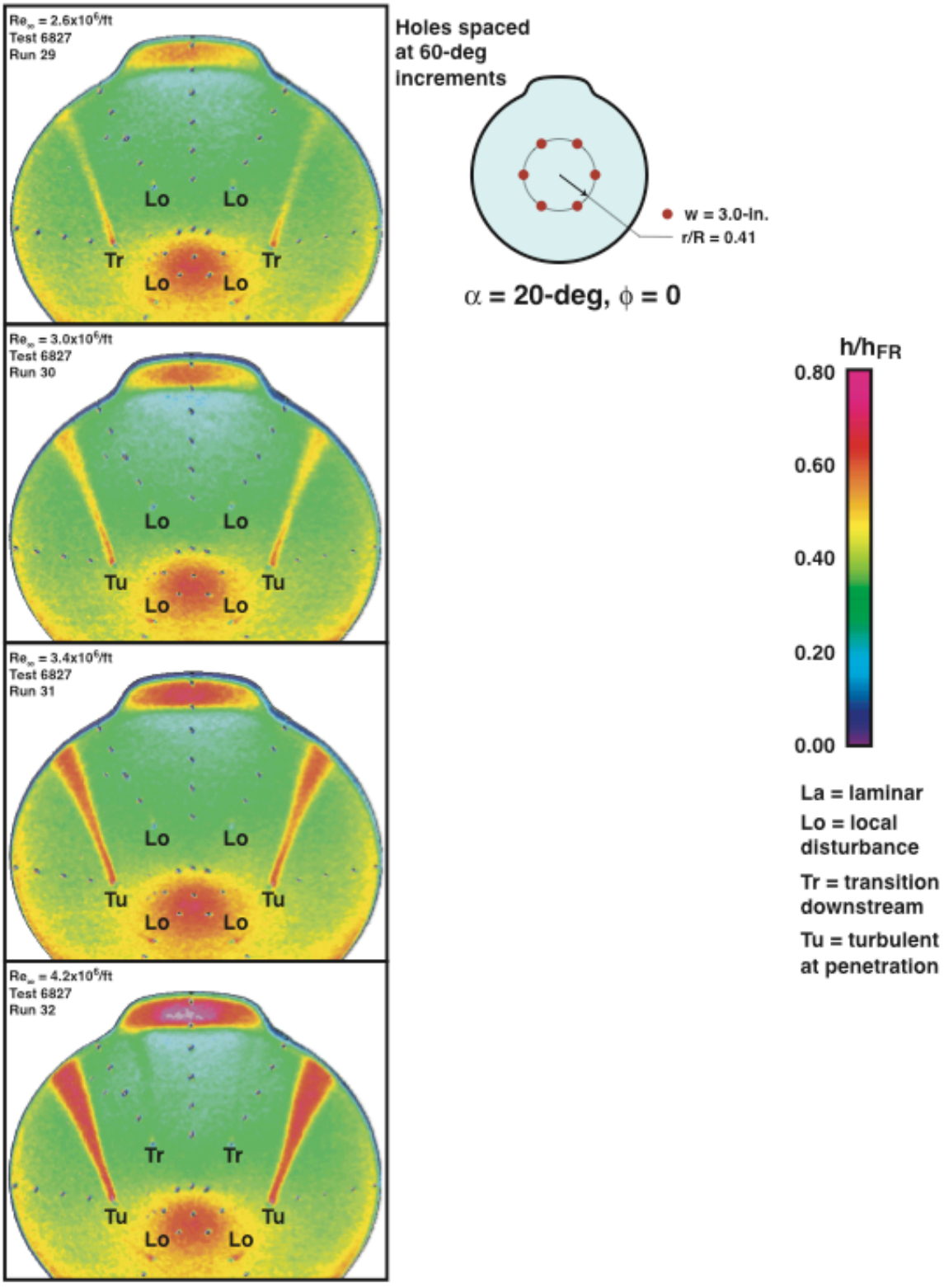

Figure 56. Cavity Effects on Heating, "Tab" T-5-3C-1 Model, α = 20-deg, ϕ = 0-deg

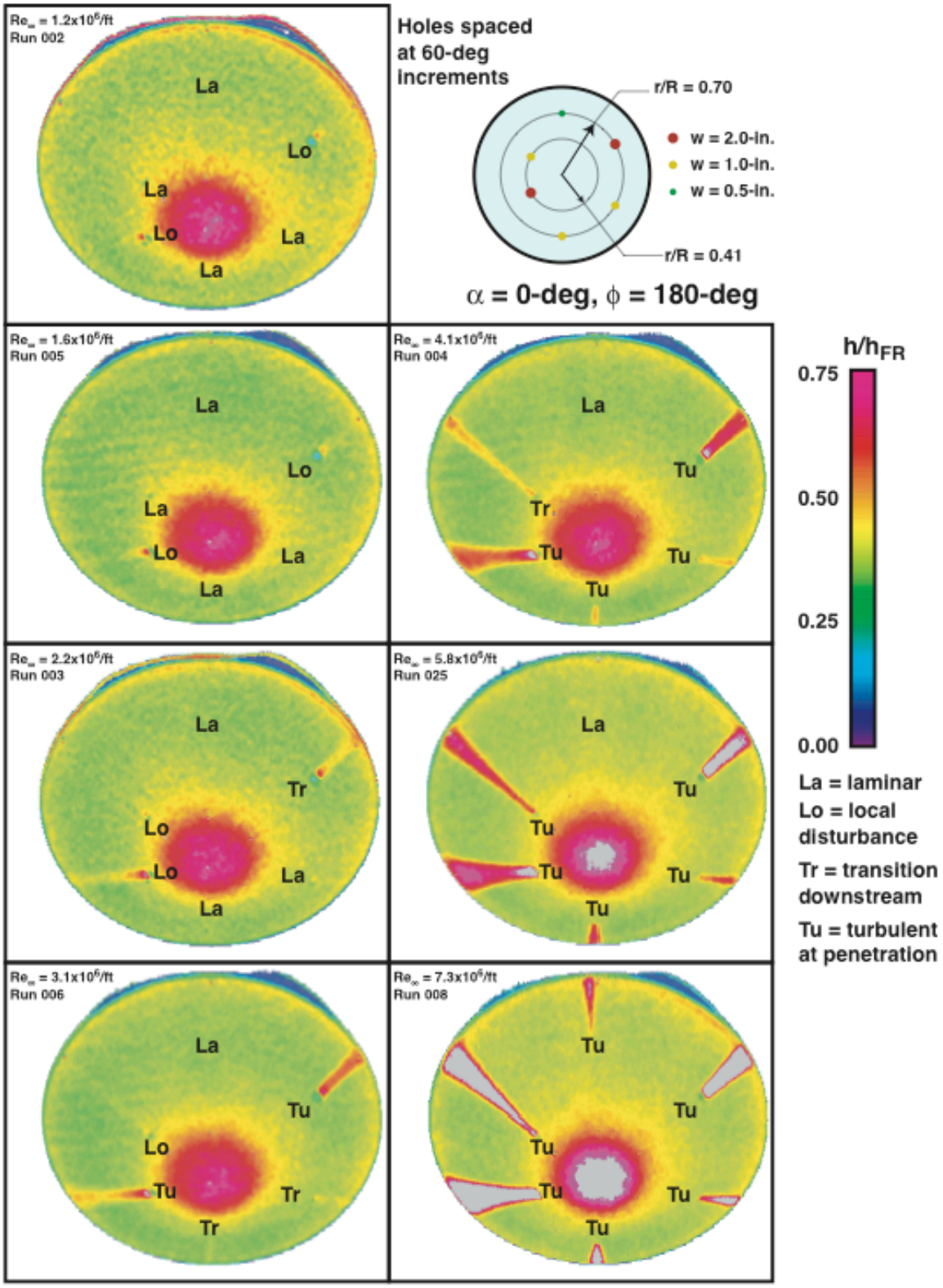

Figure 57. Cavity Effects on Heating, Old Genesis Model, α = 0-deg, ϕ = 180-deg

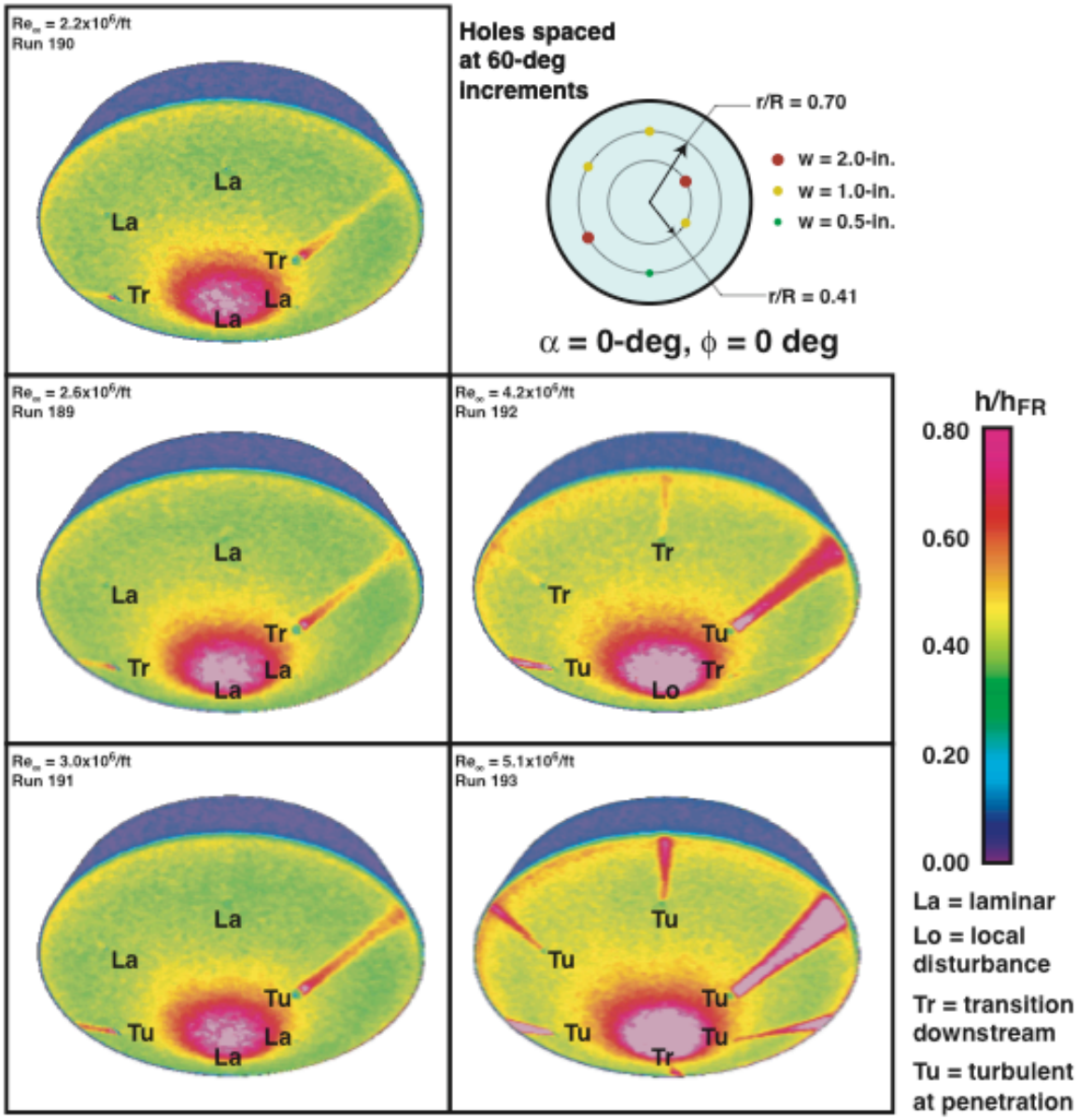

Figure 58. Cavity Effects on Heating, New Genesis Model G-5-PA-1, α = 0-deg, ϕ = 0-deg

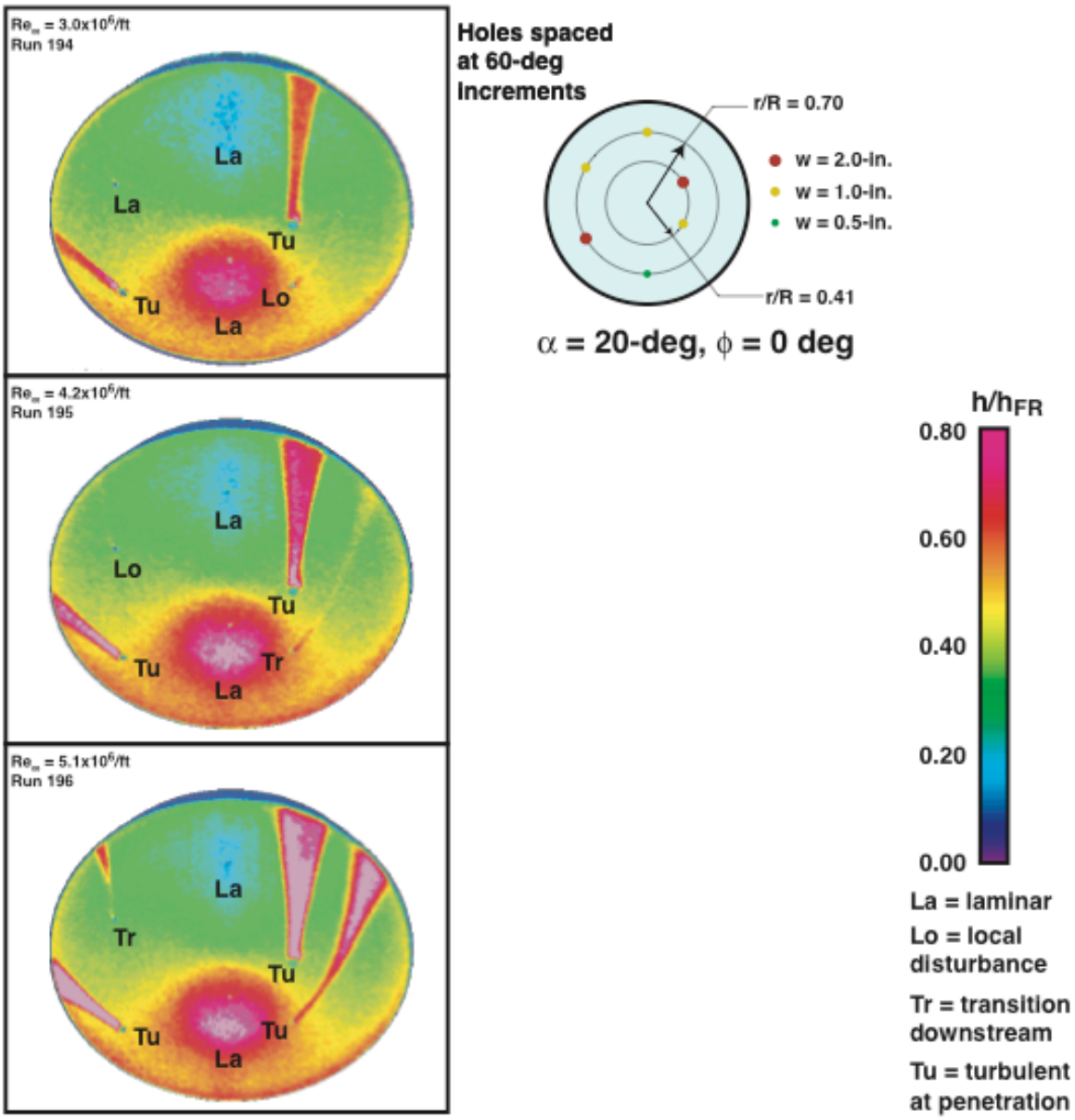

Figure 59. Cavity Effects on Heating, New Genesis Model G-5-PA-1, α = 20-deg, ϕ = 0-deg

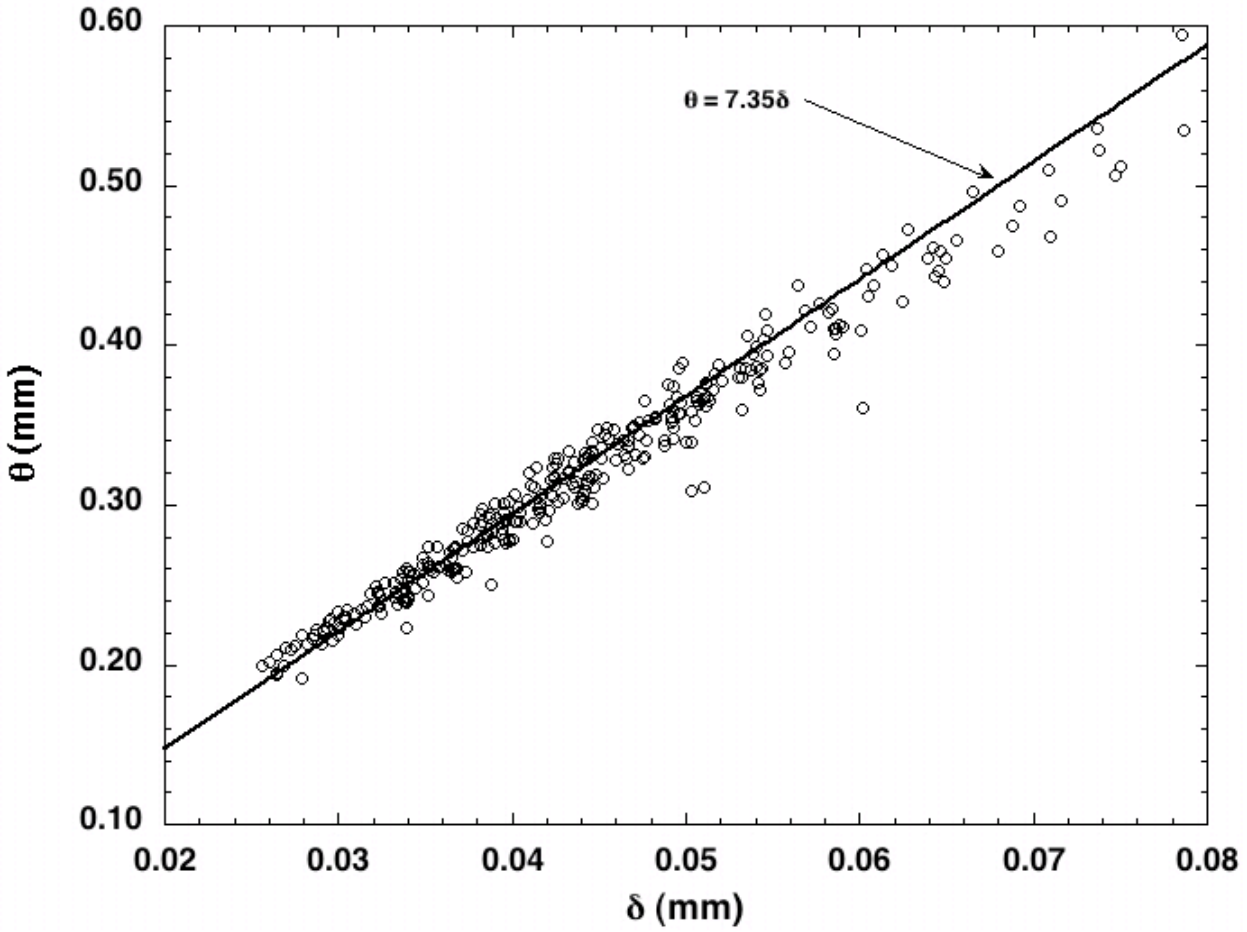

Figure 60. Relation between boundary layer height δ and momentum thickness θ for wind tunnel conditions

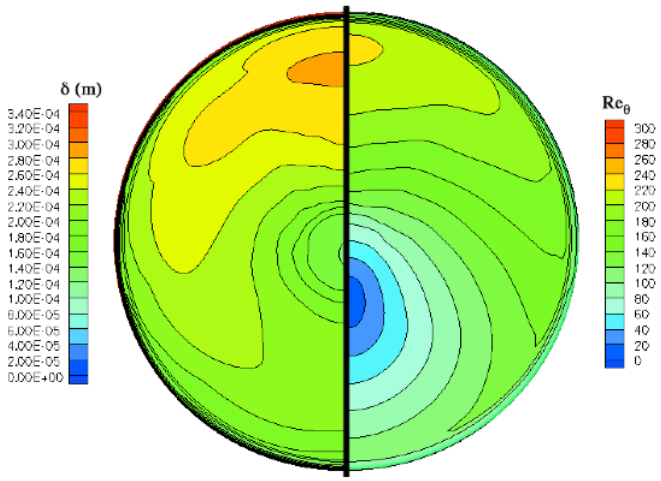

Figure 61. Re_θ and δ distributions for $Re_\infty = 4.2\times10^6$/ft, α = 11-deg

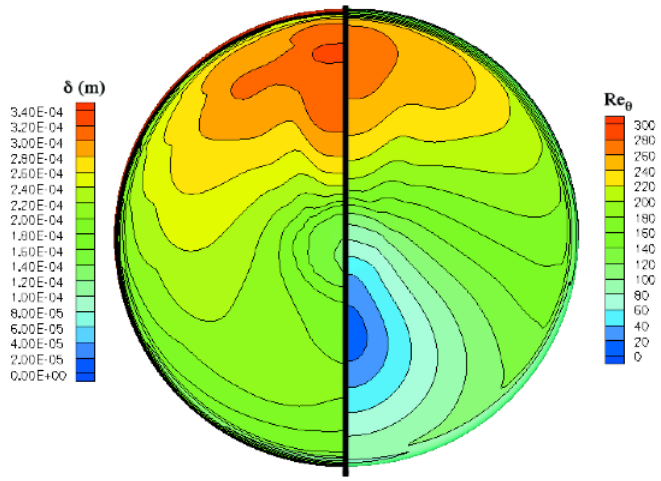

Figure 62. Re_θ and δ distributions for $Re_\infty = 4.2\times10^6$/ft, α = 11-deg

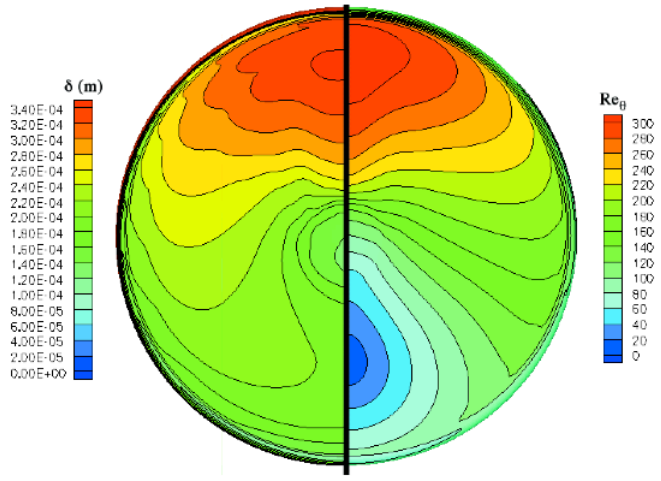

Figure 63. Re_θ and δ distributions for $Re_\infty = 4.2\times10^6$/ft, α = 11-deg

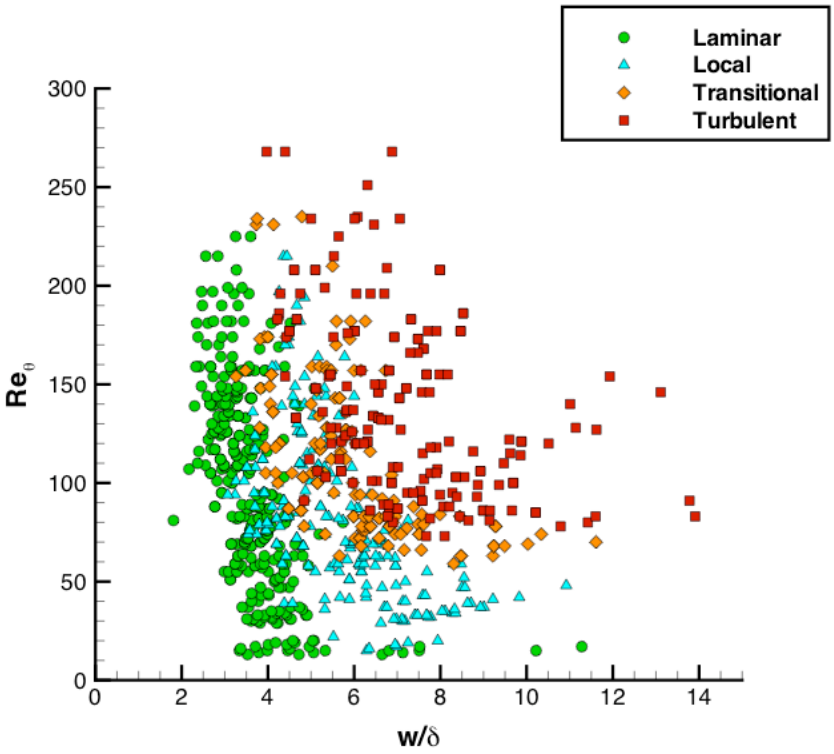

Figure 64. Cavity-Effects Data Plotted as Re_θ vs. w/δ on Linear Scale

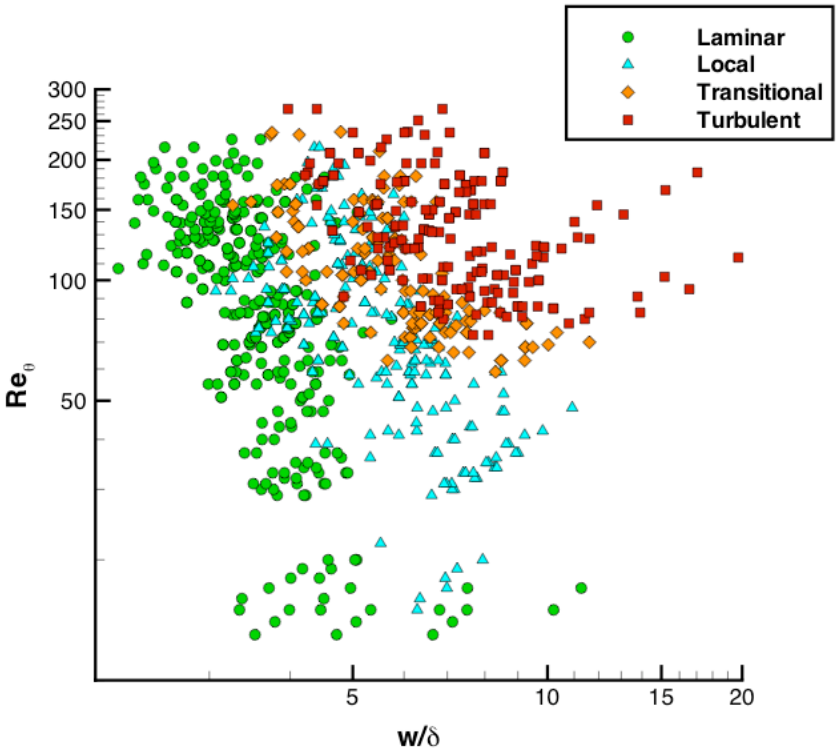

Figure 65. Cavity-Effects Data Plotted as Re_θ vs. w/δ on Logarithmic Scale

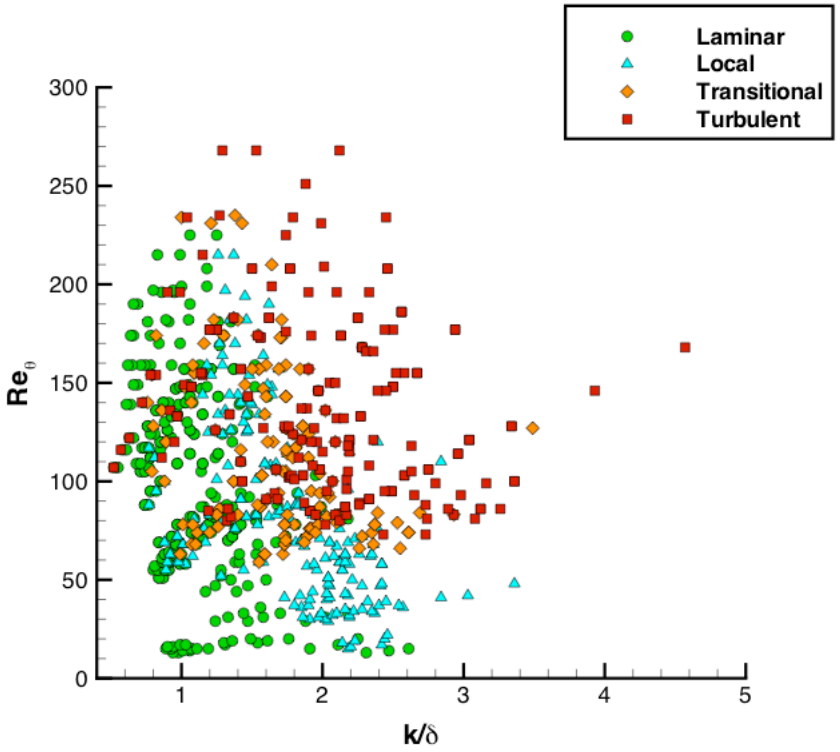

Figure 66. Cavity-Effects Data Plotted as Re_θ vs. k/δ on Linear Scale

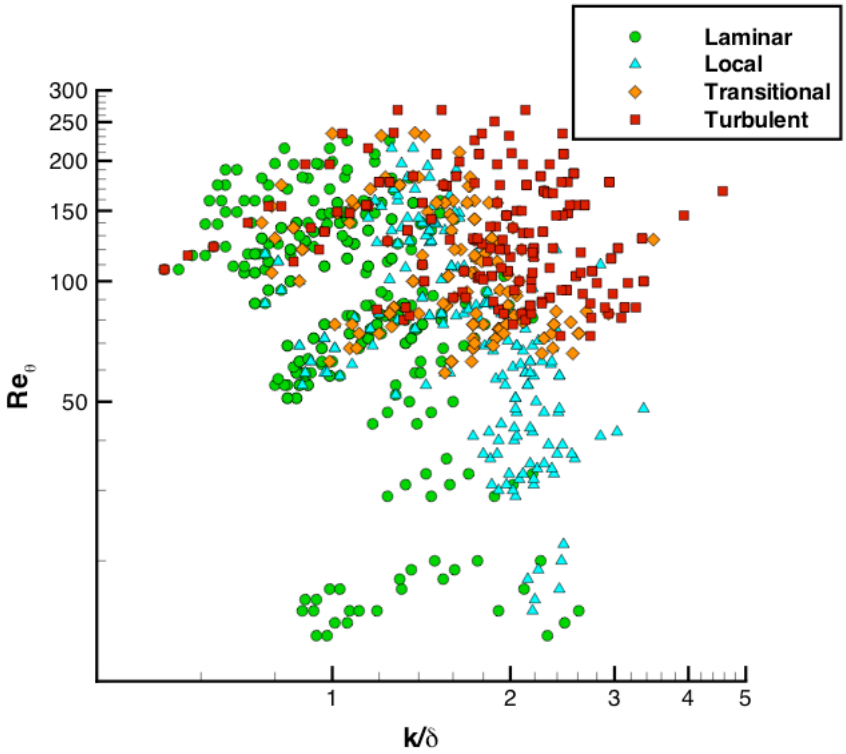

Figure 67. Cavity-Effects Data Plotted as Re_θ vs. k/δ on Logarithmic Scale

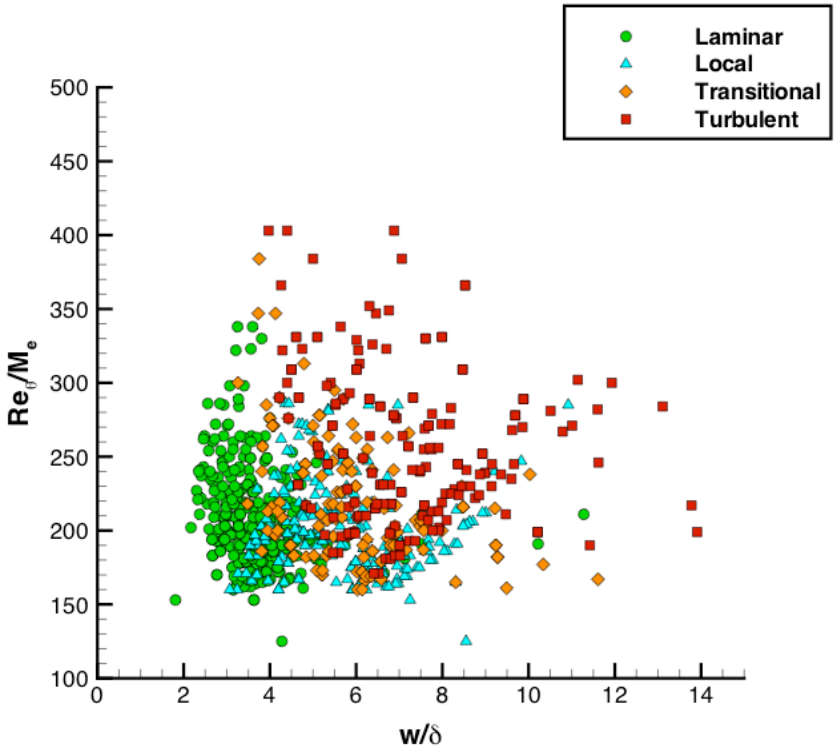

Figure 68. Cavity-Effects Data Plotted as Re_θ/M_e vs. w/δ on Linear Scale

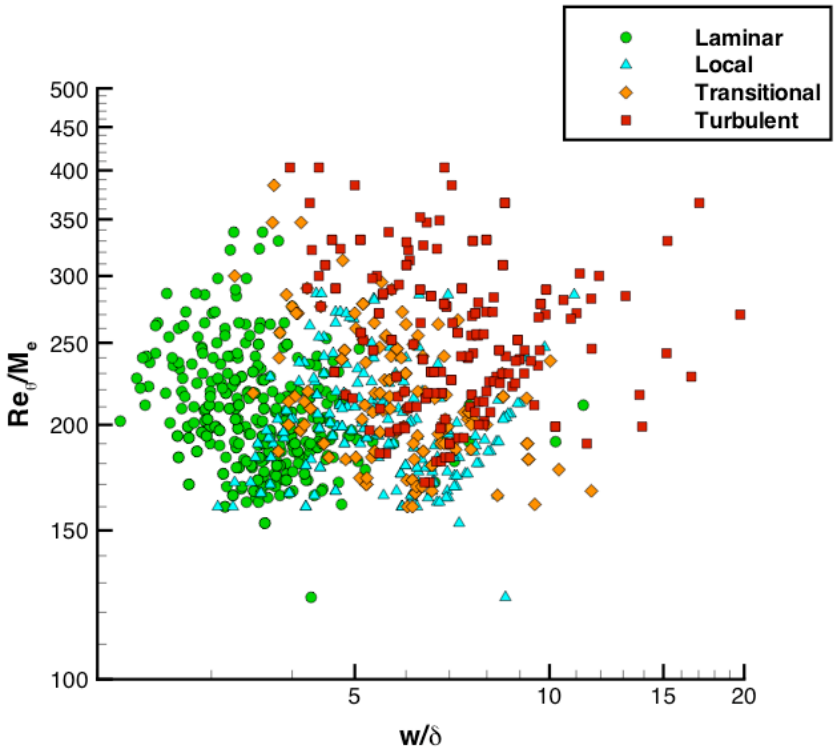

Figure 69. Cavity-Effects Data Plotted as Re_θ/M_e vs. w/δ on Logarithmic Scale

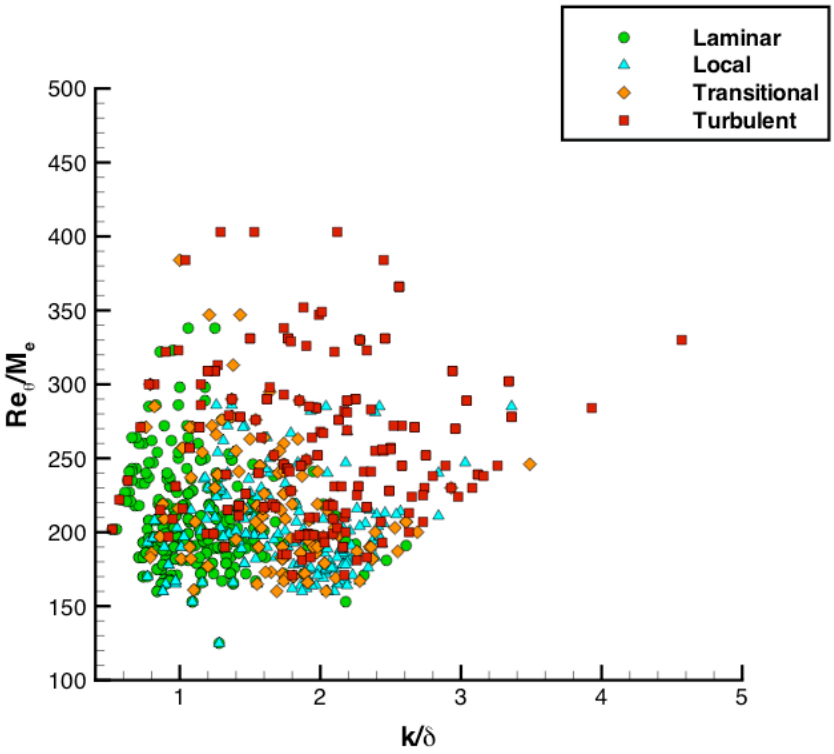

Figure 70. Cavity-Effects Data Plotted as Re_θ/M_e vs. k/δ on Linear Scale

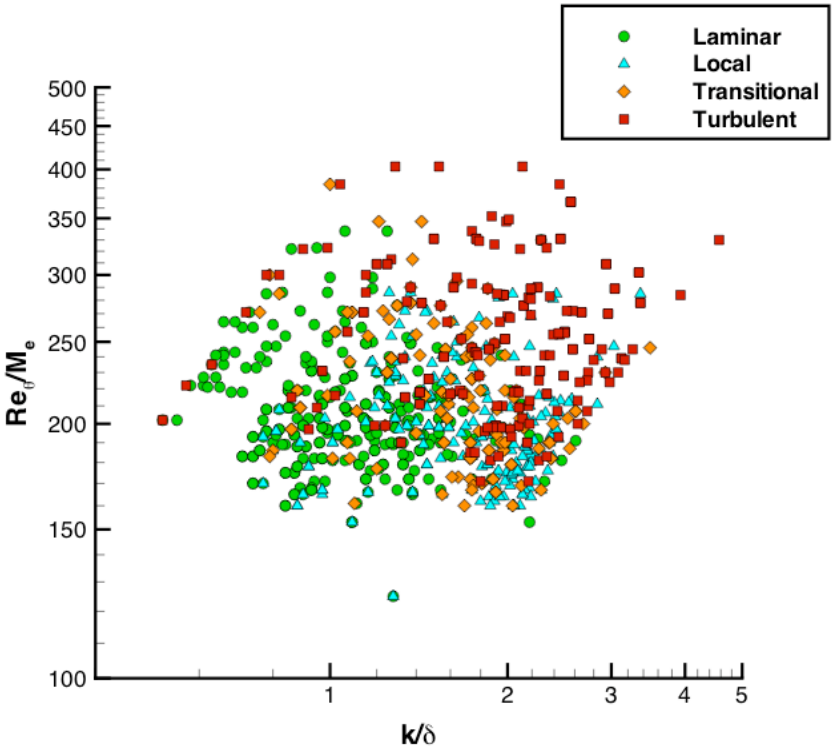

Figure 71. Cavity-Effects Data Plotted as Re_θ/M_e vs. k/δ on Logarithmic Scale

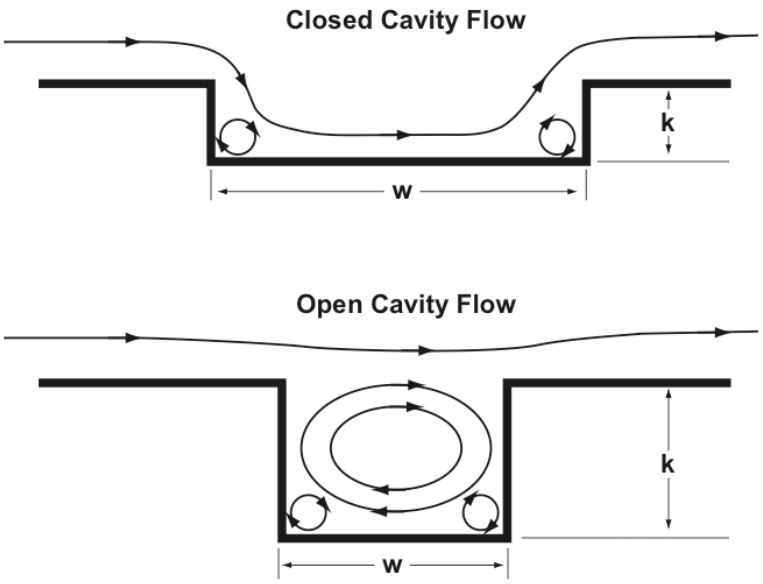

Figure 72. Illustration of Open and Closed Cavity Flows

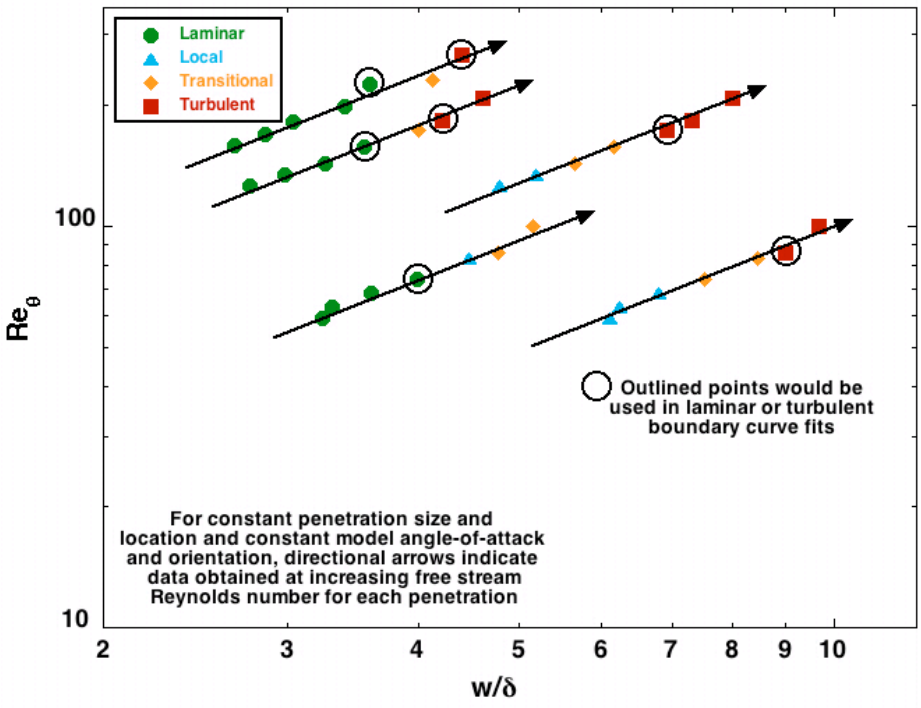

Figure 73. Example of Data Used in Boundary Curve Fits

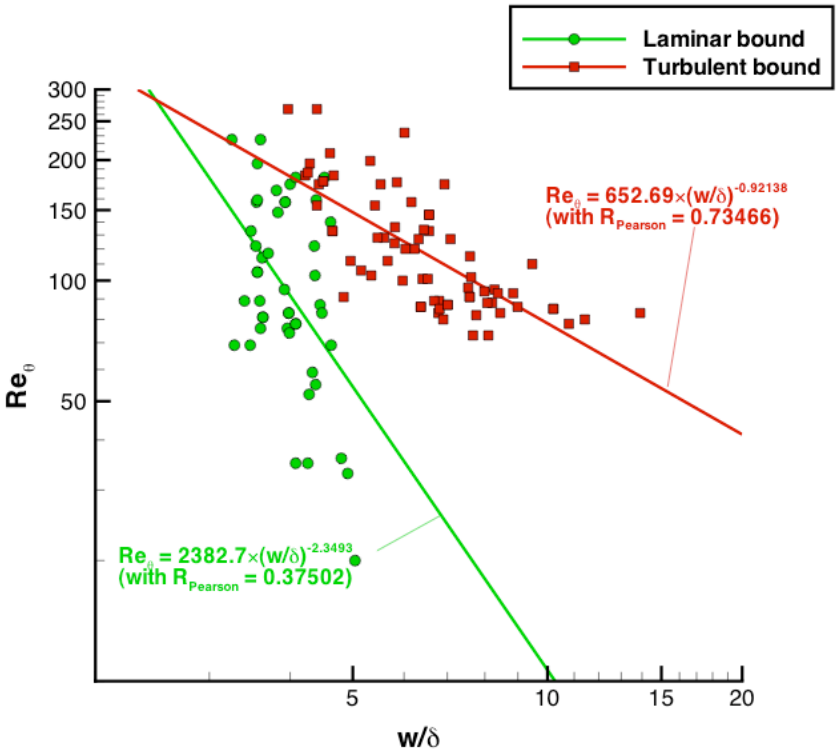

Figure 74. Correlations in Terms of Re_θ vs. w/δ

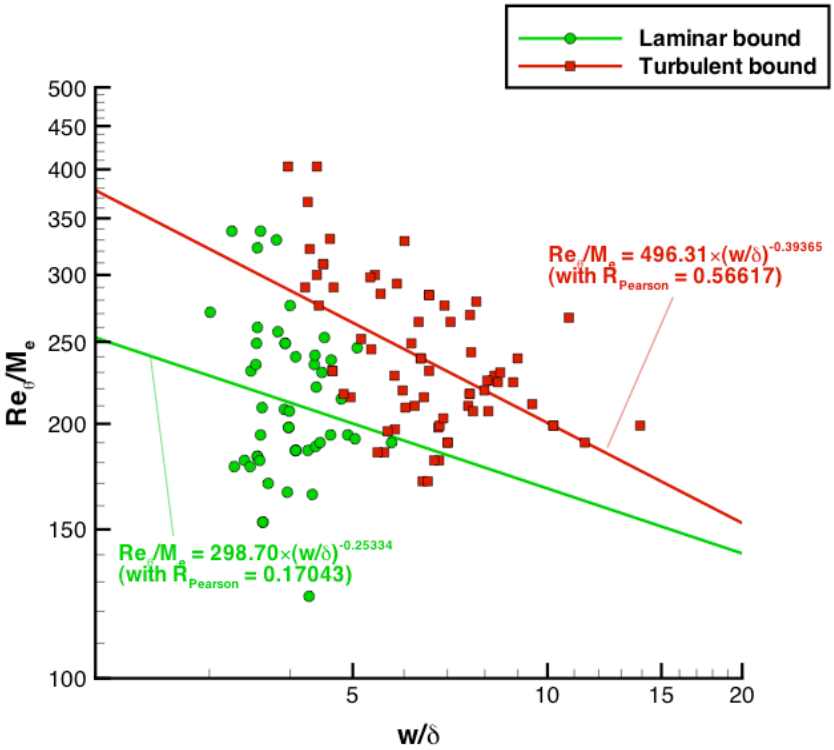

Figure 75. Correlations in Terms of Re_θ/M_e vs. w/δ

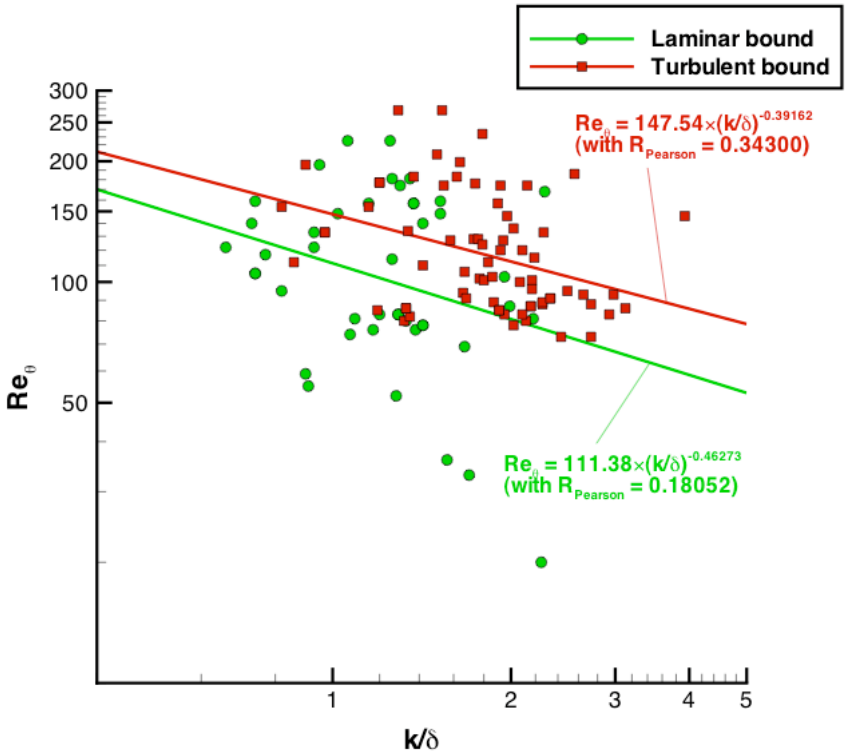

Figure 76. Correlations in Terms of Re_θ vs. k/δ

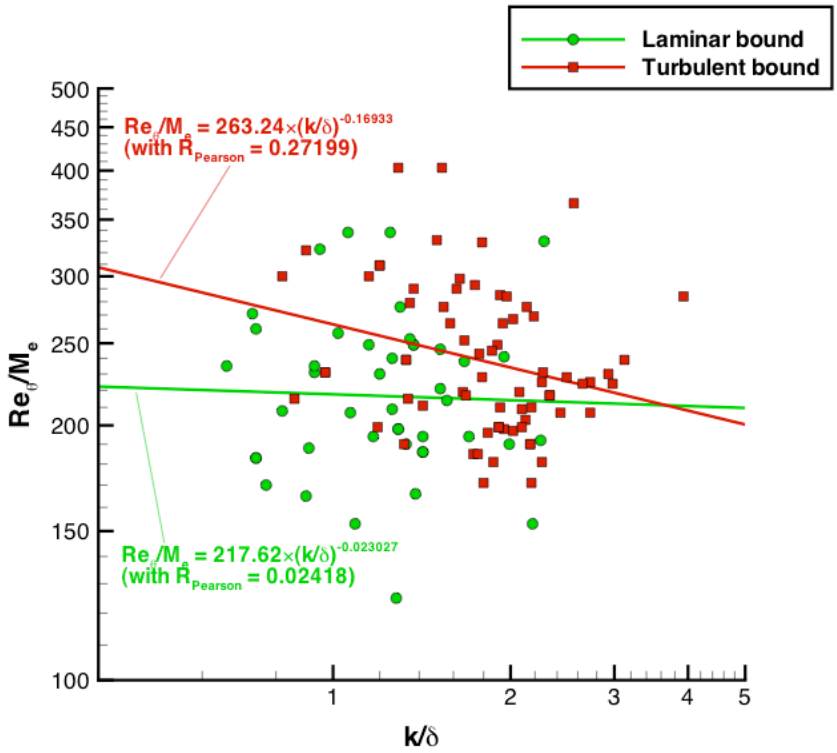

Figure 77. Correlations in Terms of Re_θ/M_e vs. k/δ

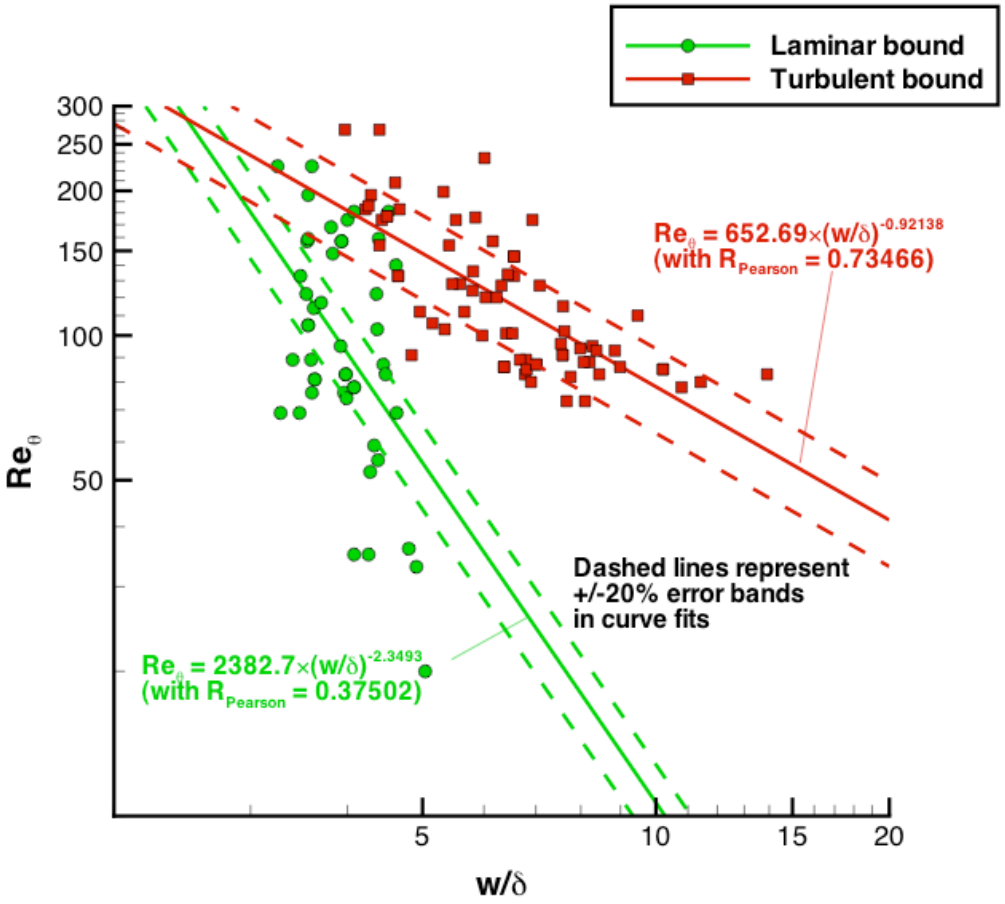

Figure 78. Correlations in Terms of Re_θ vs. w/δ with 20% error bands

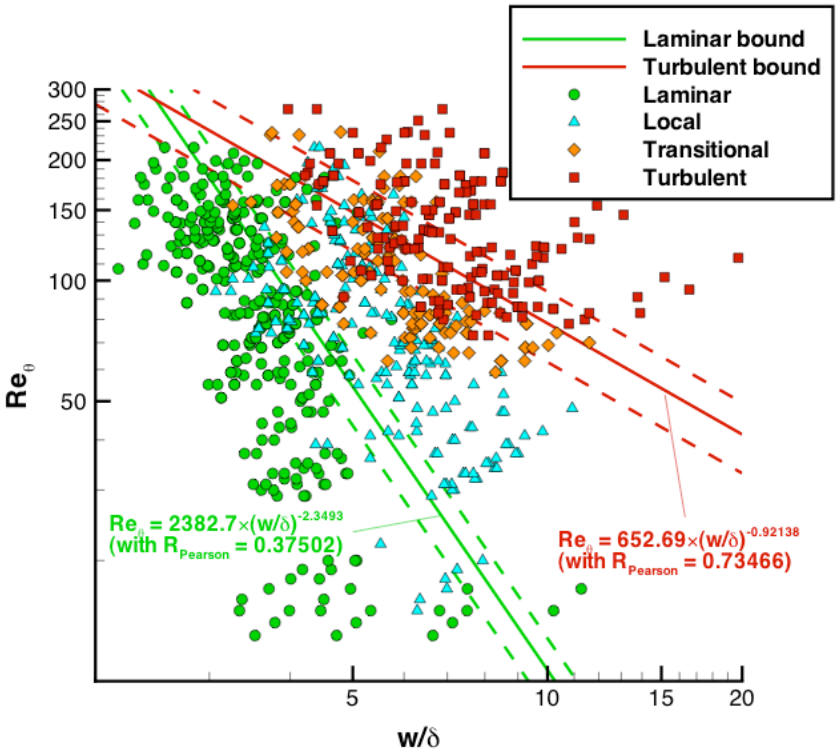

Figure 79. Complete Data Set with Correlations on Logarithmic Scales

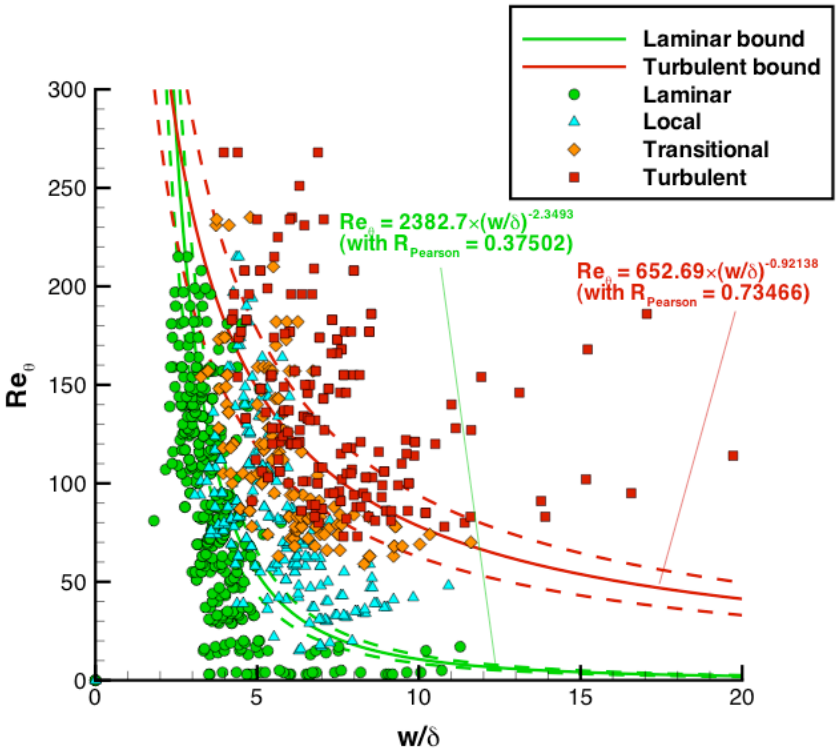

Figure 80. Complete Data Set with Correlations on Linear Scales

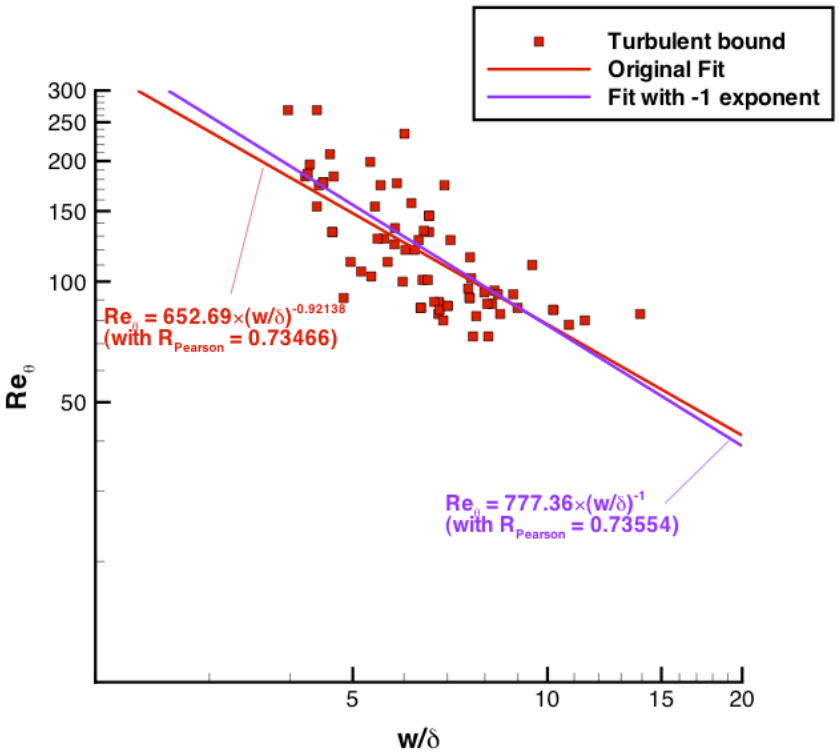

Figure 81. Comparison of Turbulent Correlation Forms

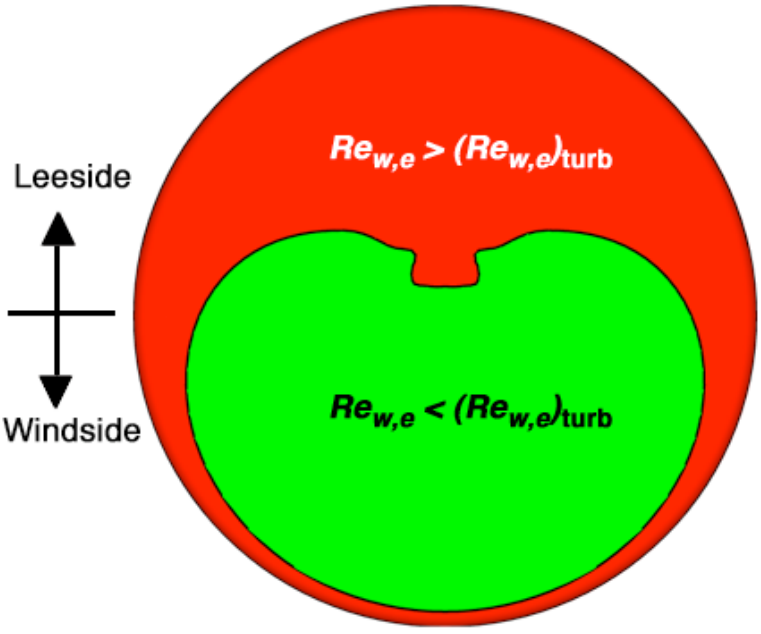

α= 16-deg, Re_∞=9.8×10^6/m, largest penetration (3.0-inch full-scale penetration)

Figure 82. Critical Reynolds Number Mapping Example for Flight Condition

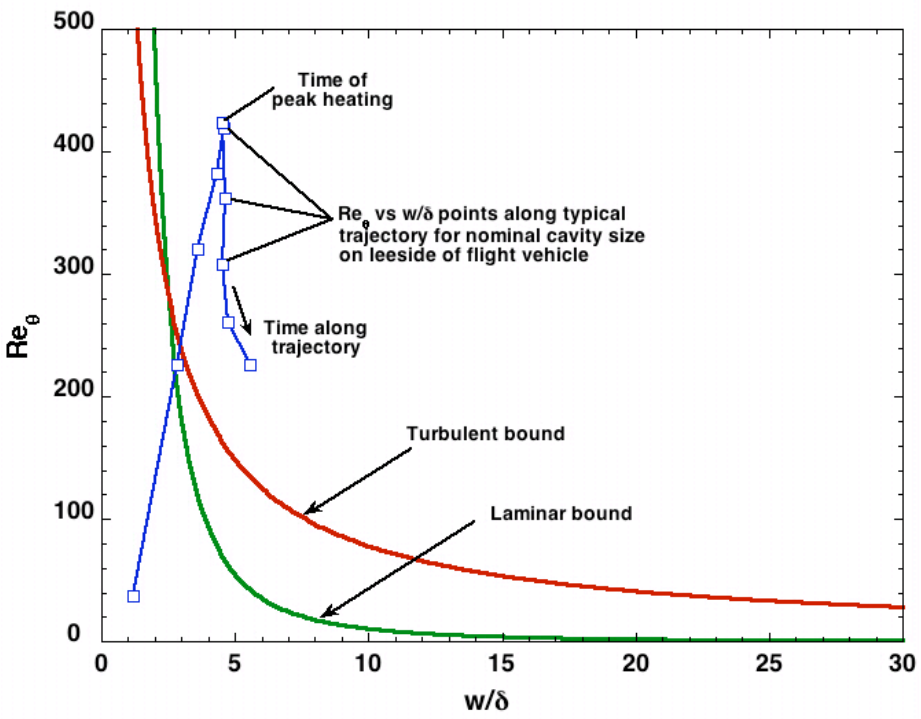

Figure 83. Typical Flight Values Compared to Correlations

REPORT DOCUMENTATION PAGE

Form Approved
OMB No. 0704-0188

1. REPORT DATE *(DD-MM-YYYY)*	2. REPORT TYPE	3. DATES COVERED *(From - To)*
01- 06 - 2008	Technical Publication	

4. TITLE AND SUBTITLE
Correlations for Boundary-Layer Transition on Mars Science Laboratory Entry Vehicle Due to Heat-Shield Cavities

5a. CONTRACT NUMBER

5b. GRANT NUMBER

5c. PROGRAM ELEMENT NUMBER

6. AUTHOR(S)
Hollis, Brian R.; and Liechty, Derek S.

5d. PROJECT NUMBER

5e. TASK NUMBER

5f. WORK UNIT NUMBER
526282.01.07.04.05

7. PERFORMING ORGANIZATION NAME(S) AND ADDRESS(ES)
NASA Langley Research Center
Hampton, VA 23681-2199

8. PERFORMING ORGANIZATION REPORT NUMBER
L-19475

9. SPONSORING/MONITORING AGENCY NAME(S) AND ADDRESS(ES)
National Aeronautics and Space Administration
Washington, DC 20546-0001

10. SPONSOR/MONITOR'S ACRONYM(S)
NASA

11. SPONSOR/MONITOR'S REPORT NUMBER(S)
NASA/TP-2008-215317

12. DISTRIBUTION/AVAILABILITY STATEMENT
Unclassified - Unlimited
Subject Category 34
Availability: NASA CASI (301) 621-0390

13. SUPPLEMENTARY NOTES
An electronic version can be found at http://ntrs.nasa.gov

14. ABSTRACT

The influence of cavities (for attachment bolts) on the heat-shield of the proposed Mars Science Laboratory entry vehicle has been investigated experimentally and computationally in order to develop a criterion for assessing whether the boundary layer becomes turbulent downstream of the cavity. Wind tunnel tests were conducted on the 70-deg sphere-cone vehicle geometry with various cavity sizes and locations in order to assess their influence on convective heating and boundary layer transition. Heat-transfer coefficients and boundary-layer states (laminar, transitional, or turbulent) were determined using global phosphor thermography.

15. SUBJECT TERMS
Boundary layer; LAURA; MSL; Cavities; Laminar; Localized disturbance; Transitional; Turbulent; Ultraviolet

16. SECURITY CLASSIFICATION OF:			17. LIMITATION OF ABSTRACT	18. NUMBER OF PAGES	19a. NAME OF RESPONSIBLE PERSON
a. REPORT	b. ABSTRACT	c. THIS PAGE			STI Help Desk (email: help@sti.nasa.gov)
					19b. TELEPHONE NUMBER *(Include area code)*
U	U	U	UU	92	(301) 621-0390